

University of Alberta

**Electromagnetic Variable Valve Timing on a Single Cylinder Engine in
HCCI and SI**

by

Masoud Mashkournia

A thesis submitted to the Faculty of Graduate Studies and Research in partial
fulfillment of the requirements for the degree of Master of Science.

Department of Mechanical Engineering

© Masoud Mashkournia
Winter 2012
Edmonton, Alberta

Permission is hereby granted to the University of Alberta Libraries to reproduce single copies of this thesis and to lend or sell such copies for private, scholarly or scientific research purposes only. Where the thesis is converted to, or otherwise made available in digital form, the University of Alberta will advise potential users of the thesis of these terms.

The author reserves all other publication and other rights in association with the copyright in the thesis and, except as herein before provided, neither the thesis nor any substantial portion thereof may be printed or otherwise reproduced in any material form whatsoever without the author's prior written permission.

EXAMINING COMMITTEE

Dr. C. R. (Bob) Koch (Supervisor), Mechanical Engineering

Dr. Rudolf Seethaler (Co-Supervisor), Mechanical Engineering, University of British Columbia

Dr. Jason Olfert, Mechanical Engineering

Dr. Robert Hayes, Chemical Engineering

ABSTRACT

An experimental single cylinder engine with variable valve timing is used to study spark ignition and homogeneous charge compression ignition (HCCI). The discrete wavelet transform, on a single cylinder engine with a cam-phasing head, is used in real time for knock detection in HCCI. Classical control schemes are used by modulating fuel octane number to show real time knock control is possible with this detection scheme. The cam-phasing head is replaced with a electromagnetic variable valve timing head and stable spark ignition (SI) and HCCI operating points are found. The robustness of the valve controller is shown by making cycle by cycle switches of valve timing events in SI and HCCI. The effect of heat on the valves from operating in SI is shown to affect valve performance. A valve motion controller, which was designed and developed as a model in simulation, has been installed on a single cylinder engine and tested. The resulting valve motion control works well providing both a robust single cylinder test system with flexible valve timing and also a simulation test bed to develop valve motion control algorithms.

ACKNOWLEDGEMENTS

I would like to thank my supervisor Dr. Bob Koch, for his help, guidance and support as well my co-supervisor Dr. Rudolf Seethaler.

I would also like to thank the technicians in the Mechanical engineering shop, especially Bernie Faulkner and Rick Conrad, who offered countless hours of suggestions, advice and help with this project.

I also want to thank my colleagues, Ahmad Ghazimirsaiied, Sepher Khaligh, Alejandro Martinez, Khashayar Ebrahimi, Ed Sperling, Hamed Babazadeh, Mahdi Shahbakhti, Jason Boddez, Dan Hanford, Michael Schleppe, Dallin Bullock, Mathew Bussiere, and Richard Groulx whose friendship and help made this experience so rich.

Finally, a sincere thanks to my parents and sisters whose love and support is without bounds.

TABLE OF CONTENTS

1	Introduction	1
1.1	Motivation	1
1.2	Problem Statement	2
1.3	Thesis Organization	2
1.4	Thesis Contributions	3
2	Background & Theory	5
2.1	HCCI Fundamentals	5
2.1.1	Knock in HCCI	9
2.2	Variable Valve Actuation Technologies	11
2.2.1	Cam Phasing Technologies	12
2.2.2	Piezoelectric Technologies	13
2.2.3	Hydraulic Technologies	14
2.2.4	Permanent Magnet and Motor Technologies	14
2.2.5	Electromagnetic	15
2.2.6	Hybrid Systems	16
2.3	Experimental electromagnetic Actuators	17
2.3.1	Control Design	19
2.3.2	Simulation Model	23
2.3.3	EVVA Test Bench	24
3	Experimental Setup	27
3.1	Basic Engine Assembly	27
3.1.1	Sensors	28
3.2	Single Cylinder Engine - Cam Phaser Head	29
3.3	Single Cylinder Engine - EVVA Head	31
3.3.1	EVVA Control and Power Electronics Bench	33
3.4	Data Acquisition and Control System	35
3.4.1	ADAPT System	35
3.4.2	CAS System	36
3.4.3	dSPACE MicroAutoBox System	37
3.4.4	National Instruments	37
3.4.5	dSPACE 1103 Controllers	37
3.5	Testing Conditions	38

3.6	Measurement Calibrations	38
4	Knock Detection and Control	40
4.1	Knock Frequency	40
4.1.1	Knock Benchmark	42
4.1.2	Continuous Wavelet Transform	44
4.1.3	Discrete Wavelet Transform	45
4.2	Knock Control - Cam Phaser Head	48
5	EVVA – SI Operation	54
5.1	Steady SI Operation for Several Valve Timing	54
5.2	Cycle by Cycle Switch of EVO in SI	57
5.3	Controller and Model Validation with SI Data	60
5.4	Cycle by Cycle Switch of IVC in SI	64
5.5	Heating Effects on EVVA System	67
6	EVVA – HCCI Operation	72
6.1	Steady HCCI Operation for Several Valve Timing	72
6.2	Cycle by Cycle Switch of IVC in HCCI	74
6.3	Controller and Model Validation with HCCI Data	79
6.4	Knock Mitigation Using EVVA	80
7	Conclusions	86
7.1	Conclusions	86
7.2	Future Work	87
	References	88
A	Uncertainty Analysis	100
A.1	Measured Parameters	100
A.2	Calculated Parameters	101
A.3	Cyclical Parameters	101
B	Experimental Data Summary	102
B.1	HCCI Data for Cam Phasers	102
B.2	SI Data for EVVA	104
B.3	HCCI Data for EVVA	106
C	Experimental Setup	108
C.1	Program and Analysis files Used	108
C.2	Pressure Sensor Calibration	108
C.3	Dynamometer Load Cell Calibration	110
C.4	Emissions Testbench	110
C.5	Cylinder Pressure Signal Pegging	116

LIST OF TABLES

2.1	Variable Valve Technology Summary	12
3.1	Ricardo Single-Cylinder Engine With Cam Phasing	31
3.2	Ricardo Single-Cylinder Engine With EVVA at Engine Start	33
3.3	Control and power electronics for EVVA system	34
3.4	Engine Operating Conditions	39
4.1	Comparison of Control Schemes to No Control Case	52
4.2	Average and standard deviation of Control Schemes Across Three Tests	53
5.1	Valve Timing for steady state cases in SI	55
5.2	Emissions and engine conditions for steady state SI cases	55
5.3	Engine Operating Conditions	57
5.4	Engine parameters for IVC changes in SI	65
5.5	Performance indicators for IVC switching	66
5.6	Engine Operating Conditions for Warm and Cold Motoring Conditions	70
6.1	Valve Timing for steady state cases in HCCI	73
6.2	Emissions Summary for the Four Test Cases	73
6.3	Engine parameters for IVC changes in HCCI	75
6.4	Performance indicators for IVC switching	78
6.5	Valve Timing for Knock Mitigation	81
A.1	Uncertainty in Measured Parameters	101
B.1	HCCI Cam Phasing Test Data	103
B.2	EVVA Test Data for SI chapter	105
B.3	EVVA Test Data for HCCI chapter	107
C.1	Programs used	108
C.2	Analysis and plot generation files used	109
C.3	Emissions Bench	111

LIST OF FIGURES

2.1	Combustion mode comparison	6
2.2	Factors effecting combustion timing	6
2.3	Ignition timing definitions	7
2.4	Cross section of the Marelli actuator used in the experimental set up	17
2.5	3D model of Marelli actuators and head on a single cylinder engine .	18
2.6	Valve state flowchart	20
2.7	Controller flow chart	21
2.8	Simulink model of EVVA system and controller - Top level	24
2.9	EVVA test bench setup	25
2.10	Simulated and test bench results using flux based feedback	26
3.1	Hardware schematic for the Ricardo single cylinder engine	29
3.2	Oil supply schematic for the Ricardo single cylinder engine	29
3.3	Coolant supply schematic for the Ricardo single cylinder engine . . .	30
3.4	Sensor schematic for the single cylinder engine	30
3.5	Valve Timing Diagram for Cam Phaser Head	31
3.6	EVVA and cam-phaser pistons	32
3.7	Intake and exhaust manifold adaptor	33
3.8	Oil supply and drain on EVVA setup	35
3.9	Control and power electronics schematic for EVVA system	36
4.1	Pressure signal for: Case A - high knock; Case B - low knock	41
4.2	Frequency modes in a cylinder	42
4.3	Comparison of pressure PSD to P_{RMS} benchmark	43
4.4	CWT Morlet coefficients for high and low knock cases	46
4.5	DWT colored coefficients for high and low knock cases	47
4.6	Comparison of DWT coefficients to P_{RMS} benchmark	48
4.7	Knock level response to step in fuel energy - no control	49
4.8	Block diagram of the FF and PI controllers	50
4.9	Knock level response to step in fuel energy - FF control	50
4.10	Knock level response to a step in fuel energy - PI control	51
4.11	Knock level response to a step in fuel energy - PI+FF control	52
5.1	Cylinder pressure curve comparison for cyclic changes in EVO timing	58
5.2	Cylinder pressure versus volume for cyclic changes in EVO timing . .	59
5.3	Valve performance for cycling changes in EVO timing	60

5.4	Simulation to engine experimental results for EVO at 180 degrees . . .	62
5.5	Simulation to engine experimental results for EVO at 100 degrees . . .	63
5.6	Pressure and Pressure-Volume diagram for cyclic changes in IVC . . .	65
5.7	Intake valve performance measures for cyclic changes in IVC	66
5.8	Return map for $\theta_{P_{max}}$ for 300 cycles of cyclic IVC	67
5.9	Return map for $\theta_{P_{max}}$ for 300 cycles of steady state valve timing in SI	68
5.10	Motoring trace showing recovery of compression as engine cools . . .	69
5.11	Intake valve opening (IVO) for cold and warm operating conditions .	70
5.12	Exhaust valve opening (EVO) for cold and warm operating conditions	71
6.1	Pressure diagram for cyclic changes in IVC for HCCI operation . . .	75
6.2	Intake valve performance measures for cyclic changes in IVC	76
6.3	Return map for cyclic changes in IVC in HCCI	77
6.4	Return map for $\theta_{P_{max}}$ for 300 cycles of steady state valve timing in HCCI	78
6.5	Simulation to engine experimental results for EVO at 180 degrees . . .	80
6.6	HCCI engine cycles showing effect of valve timing on knock	82
6.7	P-V diagram of HCCI engine cycles showing effect of valve timing on knock	82
6.8	DWT colored coefficients for (a) high knock (b) low knock	84
6.9	HCCI engine cycles showing effect of valve timing on knock	84
6.10	Oscillation in pressure trace and resulting spike in knock index	85
6.11	No oscillation in pressure trace and resulting knock index	85
C.1	Sensitivity of the pressure transducer	110
C.2	Step tests using the dead weight calibrator	111
C.3	Atmospheric pressure calibration	112
C.4	Laminar air flow meter pressure calibration	112
C.5	Intake runner pressure calibration	113
C.6	Manifold Absolute pressure calibration	113
C.7	Exhaust pressure calibration	114
C.8	N-heptane fuel pressure calibration	114
C.9	Iso-octane fuel pressure calibration	115
C.10	Oil pressure calibration	115
C.11	Dynamometer load cell calibration	116

NOMENCLATURE

Acronyms

aTDC	after Top Dead Center
BD	Burn Duration
BDC	Bottom Dead Center
bTDC	before Top Dead Center
CAS	Combustion Analysis System
CAD	Crank Angle Degree
CA10	Crank Angle of 10% mass burned
CA50	Crank Angle of 50% mass burned
CA90	Crank Angle of 90% mass burned
CO	Carbon Monoxide
CO_2	Carbon Dioxide
CWT	Continuous Wavelet Transform
DWT	Discrete Wavelet Transform
DC	Direct Current
EGR	Exhaust Gas Recirculation
eEGR	external Exhaust Gas Recirculation
EVC	Exhaust Valve Closing
EVO	Exhaust Valve Opening
EVVA	Electromagnetic Variable Valve Actuation

FF	Feed-Forward
FF+PI	Feed-Forward with Proportional Integral
HCCI	Homogeneous Charge Compression Ignition
HTR	High Temperature Reaction
iEGR	internal Exhaust Gas Recirculation
IMEP	Indicated Mean Effective Pressure
IVC	Intake Valve Closing
IVO	Intake Valve Opening
K_{PSD}	Knock index based on Power Spectral Density
LTHR	Low Temperature Heat Release
LTR	Low Temperature Reaction
MAP	Manifold Absolute Pressure
NI	National Instruments
NO_x	Oxides of Nitrogen
NVO	Negative Valve Overlap
ON	Octane Number
PRF	Primary Reference Fuel
PI	Proportional Integral
PID	Proportional Integral Derivative
PSD	Power Spectral Density
P_{in}	Intake Pressure
PWM	Pulse Width Modulation
P_{RMS}	Root Mean Squared of the Pressure Trace
RPM	Revolutions Per Minute

$ROPR_{max}$	Maximum Rate of Pressure Rise
SI	Spark Ignition
SNR	Signal to Noise Ratio
SOC	Start of Combustion
SOC-CF	Start of Combustion - Cool Flame
TDC	Top Dead Center
T_{in}	Intake Temperature
$T_{exhaust}$	Exhaust Temperature
uHC	Unburned Hydrocarbons
VVA	Variable Valve Actuation

Symbols

θ	Crankshaft Angle
λ	Air to Fuel Ratio
$\rho_{m,n}$	Oscillation Mode Factor
Δ	Sampling Period
σ	Standard Deviation
κ	Knock Value - Chapter 4
κ	Flux Linkage Parameter - Chapter 2
α	Saturable Flux Linkage Model Parameter
β	Flux Linkage Parameter
ψ	Flux linkage model parameter
φ	Mother Wavelet
η_{th}	Thermal Efficiency
θ_{Pmax}	Crank Angle Location of Maximum Pressure
a	Continuous Wavelet scale
b	Effective Viscous Damping Coefficient
c	Speed of Sound
d	Continuous Wavelet Translation
F_{center}	Center Frequency of Mother Wavelet
$f_{m,n}$	Pressure Oscillation Frequency
Fm	Magnetic Force on the Armature
Fg	Gas Force Acting Upon the Valve
F_{scaled}	Scaled Frequency of Mother Wavelet
Fv	Valve Spring Pre-load
i	Coil current

l_v	Radial Distance From the Armature Pivot Point to Where the Longitudinal Armature and Valve Axes Intersect
l_m	Radial Distance From the Armature Pivot Point to Where the Resultant Opener Magnetic Force Acts on the Armature
m	Order of the Circumferential Mode - Chapter 4
m	Effective Moving Mass - Chapter 2
\dot{m}_{air}	Mass Flow Rate of Air
n	Order of the Radial Mode
n	number of Samples
n_l	Lower Frequency Bin Number
n_h	Higher Frequency Bin Number
N_{fc}	Number of Turns of Flux Measurement Coil
N_{ec}	Number of Turns of Excitation Coil
N	Engine Speed
N	Number of Samples
\hat{p}	Filtered Pressure Trace
P_{RMS}	Root Mean Square value of the Pressure Trace
ϕ_0	Initial Magnetic Flux
R	Coil Resistance
s	Scale
sec	Second
t	Time
T	Temperature
v_{fc}	Induced Voltage
u	Control Input
V	In-cylinder Volume
v	Coil Voltage
x	Valve Position
\dot{x}	Valve Velocity
\ddot{x}	Valve Acceleration
y	Output
y_d	Desired position

CHAPTER 1

INTRODUCTION

1.1 Motivation for the Research

Internal combustion engines play a large role in modern society, from the transportation of goods and resources to the production of food and raw materials. However, the rising price of fuel and increased emissions have created much concern in society and politics. Since 1990, the greenhouse gas emissions from the transportation industry in Canada have increased by 44,000 *kt* CO₂ equivalent [Canada, 2011]. In response, the Ontario government, in 2007, has set emission goals that would see an 80% reduction in greenhouse gas emissions by 2050 from 1990 levels [Burda et al., 2010]. Similarly, the state of California has set the same goals in 2006 [Carlarne, 2010]. These tougher emissions laws and increasing price of fuel have kindled increased interest in research and development of higher efficiency engine technology. Two such technologies that hold promise in the near future are homogenous charge compression ignition (HCCI) and fully variable valve actuation (VVA). HCCI, a combustion strategy that autoignites a homogenous air-fuel mixture based on chemical kinetics, shows great promise of reducing NO_x emissions and increasing efficiency of internal combustion engines. Some challenges of this new technology, such as cold starting, speed/load limitations, and controlling combustion timing, can possibly be dealt with

by the use of variable intake and exhaust valve timing [Pischinger et al., 2000].

1.2 Problem Statement

The primary goal of this research is to implement an electromagnetic valve train on a single cylinder engine; to explore its capability in spark ignition and HCCI and its application to knock mitigation and emissions reduction. In addition, high speed electromagnetic valve control that was developed in simulation and on a test bench [Chladny, 2007][Stolk and Gaisberg, 2001] is validated on a real engine. This validation shows that the simulation is a useful tool for developing valve control strategies in simulation that work without change on the actual engine.

1.3 Thesis Organization

This thesis is organized into 7 chapters. In Chapter 2, fundamentals of HCCI are discussed and compared to SI engines. Current research in the field of variable valve timing is presented, organized by technology. Finally, Chapter 2 provides background information on the electromagnetic actuators used in this thesis. Chapter 3 describes the two single cylinder engine test beds, with cam-phasing and with electromagnetic variable valve timing. Information on the mechanical systems, software systems and operating conditions are described. Chapter 4 describes real time knock detection in HCCI using the discrete wavelet transform. Three different controllers are used in real time to control engine knock using the octane number as a control parameter and the results are presented. In Chapter 5, the Electromagnetic VVA (EVVA) system is run in SI and tests are conducted to show the valve robustness to varying cylinder pressure as well as validating the controller and model presented by [Chladny, 2007]. In Chapter 6 the EVVA system is used to achieve naturally aspirated HCCI and emissions are reported. As well, EVVA is used to show the effect on efficiency, Indicated

mean effective pressure (IMEP) and knock as valve timing parameters are changed. Finally, in Chapter 7 conclusions are presented and future work is discussed.

1.4 Thesis Contributions

Contributions of this research are summarized as follows:

- Real time knock detection using discrete wavelet transform and knock control using fuel octane to maintain combustion near knock limit for HCCI operation while preventing engine damage. Knock monitoring and control is essential in future HCCI combustion research.
- Development of a single cylinder test facility with EVVA actuators which allows for full control of intake and exhaust timing. This system was tested in spark ignition (SI) and HCCI mode and provides a platform to test cycle-by-cycle combustion control needed for HCCI combustion and switching between SI and HCCI combustion modes.
- Physics based model used to design the valve motion control in simulation is now validated on the engine. Flatness based control of valve position is implemented without any changes on the engine and works well. Thus the control design simulation model now provides a validated test bed to develop control algorithms which will work on the engine.
- Temperature effects and operating range limitations of the EVVA system are documented.
- Identified stable SI and HCCI operating points for future combustion modeling and control development.

- Cycle-by-cycle HCCI valve timing is implemented using the valve actuators and the combustion is examined.

CHAPTER 2

BACKGROUND

HCCI and SI engine fundamentals that are pertinent to this thesis are introduced in this chapter. Various variable valve actuation technologies and the electromagnetic actuators used in this study are also described.

2.1 HCCI Fundamentals

Homogeneous Charge Compression Ignition (HCCI), as found by Najt and Foster [1983], is a combustion method where the fuel and air are pre-mixed and compressed in the combustion chamber until ignition occurs relatively uniformly throughout the combustion chamber. This differs from spark ignition (SI) engines since there is no spark plug and differs from compression ignition (CI) or diesel engines since there is no direct injection event to time the combustion. Thus, in HCCI, no direct input is used to trigger combustion as illustrated in Figure 2.1. Rather, ignition occurs as a result of in-cylinder conditions and this is difficult to control. Since HCCI is usually a lean burning combustion, a reduction in throttling losses and thus improved fuel economy is possible compared to SI at part load operating conditions [Kulzer et al., 2007b][Kulzer et al., 2007a]. The ignition process itself differs from SI, since in SI the flame front takes a finite time to travel from the spark location to the ends of the cylinder. However in HCCI, the the flame

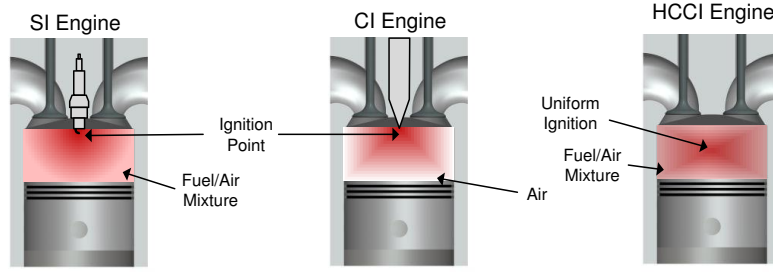


Figure 2.1: Combustion mode comparison

front begins in numerous locations leading to much faster pressure rise rates than SI. Common methods to achieve suitable in cylinder conditions for HCCI include air heating, exhaust gas recirculation, supercharging or turbocharging [Lupul, 2008]. Auto-ignition of the fuel in HCCI typically exhibits one of two modes. The first is a single stage combustion, where the fuel is oxidized in a single event. The second is a two stage combustion event consisting of a low temperature reaction (LTR) and a high temperature reaction region (HTR) [Kalghatgi, 2007].

The engine parameters of manifold absolute pressure (MAP), intake temperature (T_{in}), engine speed (RPM), exhaust gas recirculation (EGR), lambda ratio (λ), and fuel octane number (ON) all effect combustion characteristics, specifically ignition timing as shown in Figure 2.2 [Shahbakhti and Koch, 2010].

Ignition timing, an important parameter in HCCI combustion, is dependant on the

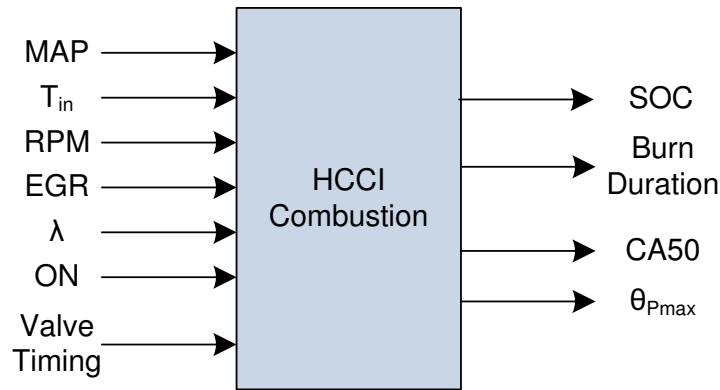


Figure 2.2: Factors effecting combustion timing

engine parameters listed above. The start of combustion (SOC) is defined as the point at which the third derivative of the pressure trace with respect to the crank angle (θ) exceeds a heuristically determined limit [Ghazimirsaid, 2012]. $\theta_{P_{max}}$ is the crank angle of maximum pressure, and is found to be a robust indicator of ignition timing [Ghazimirsaid and Koch, 2012]. One of the most common combustion metrics is CA10, CA50 and CA90, the crank angle at which 10%, 50% and 90% of the fuel mass fraction is burned, respectively. The burn duration (BD) is defined as the crank angle rotation between CA10 and CA90. These combustion parameters are shown in Figure 2.3 including the location of the SOC for the LTR referred to as the cool flame (SOC-CF). Increasing the intake temperature of the mixture for

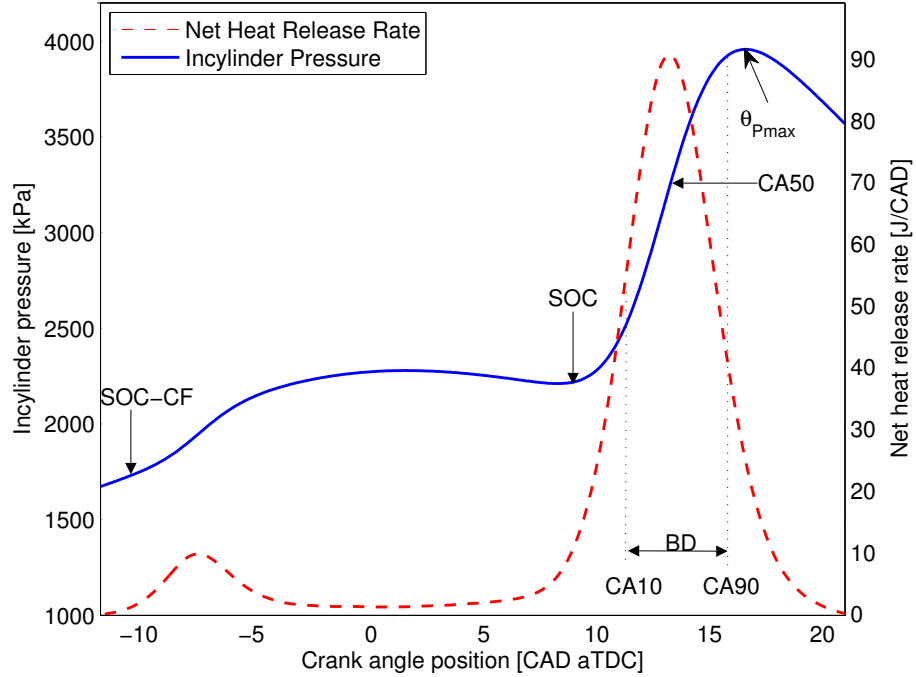


Figure 2.3: Ignition timing definitions. Adapted from [Shahbahkti, 2009]

HCCI causes combustion to occur earlier and lowers the covariance of the Indicated Mean Effective Pressure (IMEP) for an operating point [Persson et al., 2004]. This increase in inlet temperature can be obtained by EGR [Iverson et al., 2005] or by

heating the intake [Atkins, 2004].

Increasing MAP by boosting (turbocharging or supercharging) for HCCI combustion can increase the HCCI load range. An increase in the operating range by 6.5 bar break mean effective pressure (BMEP) with high dilution rates and low temperature combustion has been experimentally shown [Kulzer et al., 2011]. A study of three different boost strategies, turbocharging, supercharging, and series turbocharging indicate that all three methods extend the high load operating range of HCCI with series turbocharging providing the highest range extension [Mamalis et al., 2010]. Single turbocharging proved to be the most efficient method but does not provide the maximum attainable load. Supercharging was found to avert back pressure problems but had lower brake efficiency due to mechanical work required to provide boost [Mamalis et al., 2010].

Engine speed directly affects combustion timing since the auto-ignition process in HCCI is a time-based process. Using a Primary Reference Fuel (PRF) of ON=80, [Sjöberg and Dec, 2007] illustrated how increased engine speed corresponds to decreased low temperature heat release (LTHR). In their work, in order to keep the crank angle in which 50% of the burned fuel mass fraction (CA50) constant, intake temperature, T_{int} was modified. It was found with increasing engine speed, for a given ON, the intake temperature, T_{in} , must be increased to maintain combustion timing. It was shown that increased intake pressure (MAP) can reduce the temperature requirements for constant CA50. It was further shown that intake pressure alone can be used to control CA50 with different engine speeds [Sjöberg and Dec, 2007].

The use of EGR has been shown to delay autoignition for HCCI operation with different fuels [Dec, 2002] [Yao et al., 2005] [Olsson et al., 2003] and thus enable a wider engine-speed range. EGR can be achieved by using external EGR, internal EGR (iEGR) or a combination of the two. Internal EGR has been shown to have stronger effects of charge heating while external EGR has a stronger dilution and

specific heat capacity effects [Audet, 2008]. It has been shown that both start of combustion as well as burn duration are sensitive to mixture dilution from EGR [Atkins and Koch, 2005]

Automotive engines typically operate over a range of engine speeds and loads. However, HCCI does not have as large of a speed load range as that of SI engines [Santoso et al., 2005]. For low load, HCCI is limited in part by increase in CO production due to low combustion temperature [Yang et al., 2002][Kaiser et al., 2002]. As the load decreases, the fuel/air mixture becomes lean causing delayed combustion timing that eventually lead to misfires, or a lack of autoignition of the air fuel mixture. This can potentially lead to damage a catalytic converter and lowers efficiency [Kim et al., 2000]. For high load, HCCI combustion is limited by knocking phenomena which is associated with an audible knocking or pinging sound [Draper, 1933]. One solution to the limitations of HCCI is to mode switch to SI and back as needed [Dickey, 1999]. Fully variable valve timing is useful tool as fast actuation is required to ensure a smooth transition for which no misfire or knocking cycles occur [Santoso et al., 2005].

2.1.1 Knock in HCCI

At high loads, the overly rapid combustion energy release, and associated pressure oscillations, in an engine is often termed as a "knocking" or "pinging" noise [Sheppard et al., 2002]. The pressure oscillations in HCCI could conceivably give rise to engine damage similar to that experienced in SI engines due to engine knock or scrubbing of the thermal boundary layer present in the cylinder. Removing this boundary layer exposes the in-cylinder surfaces to the high temperature combustion gases, resulting in significantly increased heat transfer [Tsurushima et al., 2002].

After the HCCI combustion, the descending piston as well as heat transfer cause the in-cylinder temperature to decrease. As the mixture temperature changes, the dom-

inant resonance frequency of the pressure oscillations varies according to the local speed of sound of the mixture. The nature of knocking is thus a very transient one, as the rapid initiation of the oscillations during combustion is followed by a significant change in the characteristic frequency as the piston descends during the power stroke. One important difference between knock in HCCI and SI combustion is that while knock in SI results from the abnormal case of auto-ignition of the end gas zone, the pressure oscillations of HCCI are formed due to the normal auto-ignition of the in-cylinder mixture.

Numerous methods for detecting knock have been proposed. Typically, the pressure waves of knock resonate at a particular frequency that is characteristic of the combustion chamber geometry. The Fourier transform is often used to determine the presence of knock by looking at the characteristic frequency [Ashrafzadeh et al., 1991] [Vulli et al., 2008]. However, for a non-stationary signal such as knock, traditional signal processing techniques have limitations as they rely on the assumption of a stationary, periodic signal. Furthermore as engine speeds increase, additional mechanical noise from the valve train and piston movements reduce the signal to noise ratio and greatly reduce the effectiveness of the traditional methods [Nilsson et al., 2009]. The use of a wavelet transform to obtain time frequency resolution is advantageous for the transient HCCI knock [Geradin et al., 2009]. Both continuous and discrete wavelet transforms have been used [Chang et al., 2002] [Borg et al., 2005] [Berntsson and Denbratt, 2007]. However, the continuous wavelet transform requires significant computational effort [Zhang and Tomita, 2000] and so the computations are often done off-line. In order to be able to control the amount of knock in real time on an engine, a more computationally efficient method is needed. The discrete wavelet transform is a promising real time method of knock detection.

Many knock control schemes have been proposed using a variety of knock detection methods. For spark ignition or diesel engines, actuators such as spark

timing [Souder et al., 2004], exhaust gas recirculation [Yunlong et al., 2010] or injection timing [Jones et al., 2010] are used to influence the combustion and control of knock. In HCCI, however, the most conventional actuation of spark timing or injection timing is not available. The use of multiple fuels is a growing area of research with promise [Visakhamoorthy et al., 2012] [Lakshmanan and Nagarajan, 2010] [Ebrahimi et al., 2011]. For HCCI combustion the high load operation is limited by knock [Atkins and Koch, 2005] and can be increased by increasing fuel octane number [Lu et al., 2011]. With this direct relationship known, the use of PRF, which defines the ON scale can be used as a control input. In this study, the engine is operated near the knock limit and then the load is increased by increasing the amount of fuel injected to cause knock. This causes engine knock which is detected and controlled by modulating fuel octane number. A study by [Audet and Koch, 2009] directly compares the use of octane number modulation for combustion timing control to VVA. This study finds that both actuation methods are suitable for combustion timing control with no significant difference in the performance of each actuator.

2.2 Variable Valve Actuation Technologies

In order to create more efficient and lower emission vehicles, engines equipped with variable valve timing have become a major area of focus for research and development. Changing the valve timing event for different RPM and load, can lead to many advantages. Although not new [Payne, 1899], variable valve timing has been found to benefit emissions [Brustle and Schwarzenthal, 2001], power [Mahrous et al., 2009], efficiency and even backfire [Verhelst et al., 2010]. Variable valve timing has also been used for cylinder deactivation where fuel consumption improvements of 40% were reported [Sabri, 1998]. The following section describes current research in different

types of variable valve actuation technologies with a discussion on the advantages and disadvantages of each type. The common types of VVA technologies include cam phasing, piezoelectric, hydraulic, permanent magnet, electromagnetic, and combinations of these technologies. A summary of the main advantages and disadvantages are given in Table 2.1.

Table 2.1: Variable Valve Technology Summary

Technology	Advantages	Disadvantages
Cam Phasing	Reliability Variable Valve Lift	Cycle by cycle actuation only at low engine RPM
Piezoelectric	Fully variable timing	Small displacements Complicated control
Hydraulic	Fully variable timing soft landing variable valve lift	Space requirements Temperature sensitivity Precise/expensive valves High power consumption
Permanent magnet and motors	Fully variable timing	Low force generation Weight Low valve speeds
Electromagnetic	Fully variable timing Space requirements	Additional electronics Soft landing needed Weight

2.2.1 Cam Phasing Technologies

Cam phasing is a technology that incorporates a traditional cam shaft but allows for variable valve actuation. It has already been incorporated in several production vehicles [Brustle and Schwarzenenthal, 2001][Hosaka, 1991] and remains an active area of research to further improve engine capabilities. Cam phasing combined with a variable cam lift [Nagaya et al., 2006] uses a timing belt connected to a camshaft similar to a conventional engine. However, the camshaft in this system has a planetary gear set where the sun gear is connected to a separate worm gear and motor that can phase the camshaft. This system also has a variable valve lift mechanism

which uses a cam that has a slope in the axial direction. As the camshaft is actuated with a motor, the cam lobe relative to the valve stem moves up or down changing the valve lift. A novel approach that mechanically controls both valve lift, duration and phasing, with a fixed relationship between the three is demonstrated and tested on a European 4 cylinder engine [Pierick and Burkhard, 2000]. A two step early intake valve closing mechanism is compared to a three step and fully variable timing strategies by [Sellnau and Rask, 2003] which can be used in production engines. It should be noted as well that cam phasing, both continuous and discrete forms, are already present in production engines [Sun and Cleary, 2003][BMW Canada, 2010]. With cam phasing, the camshaft relative to the crankshaft is phased and thus valve timing is changed to a new profile. In this method individual cylinder or cycle to cycle actuation is complicated and costly [Sellnau and Rask, 2003]. Independent control of valve timing is desirable for many reasons such as controlling HCCI combustion [Agrell et al., 2003] or to achieve better air-fuel mixing using asymmetric valve opening of two intake valves on a single cylinder [Lou, 2007]. A camless variable valve actuation system is reported to increase the operating range of HCCI by 200% but also increase manufacturing cost by 40% [Lang et al., 2005].

2.2.2 Piezoelectric Technologies

Piezoelectric actuators have the ability to apply relatively large forces in a short time period [Peterson, 2005]. However, the displacement is quite small in these systems; Thus there is a trade off between output force and displacement range. A piezoelectric ceramic stack actuator mechanism that reciprocates at a high frequency is proposed by [Jalili et al., 2003]. The small displacements are accumulated using a ratchet-type mechanism to achieve a high force and sufficient displacement for valve actuation. A valve actuation device that uses piezo-elements to ultimately push against a spring holding the valve closed is proposed by [Heiko et al., 2000]. This system amplifies

the stroke of the piezo-elements by pushing against a large displacer in a hydraulic system.

2.2.3 Hydraulic Technologies

Electrohydraulic variable valve timing uses a hydraulic pump that actuates each valve in an engine individually giving full valve actuation. It requires a hydraulic pump (usually large) and proportional valves that will direct fluid toward the valve. Electrohydraulic VVA systems typically have high power consumption, are temperature sensitive, and require expensive proportional valves [Lou, 2007].

Current research by [Gillella and Sun, 2009] is focused on developing a system that has effective lift and seating velocity control as well as using less hydraulic pump power. Their work has continued in [Gillella and Sun, 2011] where they have validated a model and a control scheme for the valve system.

A electro-hydraulic actuator for fully variable valve timing has been developed by [Sun and Cleary, 2003]. They are able to achieve tracking errors within 140 microns for a 9.5mm lift at engine speeds up to 3000rpm. Attention is also being put into the area of regenerative hydraulic variable valve actuation which recovers some of the energy used by the system [Sabri, 1998]. This manifests itself as re-pressurizing the hydraulic fluid in the case of [Schechter et al., 1994] and [Erickson and Richeson, 1992].

2.2.4 Permanent Magnet and Motor Technologies

Electric rotary motors can be used for valve actuation by the use of a mechanism to convert angular motion into linear motion. Rotary motors are able to provide variable valve lift and are generally temperature and wear compensating unlike electromagnetic valve trains [Zhao and Seethaler, 2011]. The linear behavior of the actuator system only requires a simple control strategy. However, large motors are often required in order to achieve the necessary torque requirements. A brushless DC motor has

been proposed by [Zhao and Seethaler, 2011] that actuates the intake valve through an off-center arm to increase the torque that can be applied.

A VVA system proposed by [Duerr and Seethaler, 2008] uses an electric motor connected to a camshaft that actuates the valve. This system also incorporates a spring to store energy so the electric motor is only used to overcome friction losses and combustion forces on the valve. This system achieves valve seating velocities that are independent of the engine speed which makes soft valve landing difficult at low RPM. The same team developed another system with two cam configurations operated with an electric motor that solves this problem and provides continuously variable lift at low engine speeds [Seethaler and Duerr, 2009]. An electric motor driven valve train where the electric motor uses a non-linear mechanical transformer to convert the rotational movement of the motor into the desired valve motion has been developed by [Chang et al., 2003].

Many different types of magnetic actuators from the moving coil actuators to the “Sawyer motor” which is a two-phase pulse permanent magnet linear actuator is described by [Boldea and Nasar, 1999]. These technologies, however, are best suited for larger valve travel but may have application to variable valve actuation. A linear actuator that uses permanent magnets is proposed by [Lequesne, 1992]. It is best suited for fast actuation at lower frequencies. Permanent magnet VVA actuation can be limited by the high temperatures that the valve will be subject to in an automotive applications [Johnson et al., 2004].

2.2.5 Electromagnetic

Typical Electromagnetic valve trains consists of two pre-compressed springs and a moving armature between two electromagnets at each end [Pischinger and Kreuter, 1984]. Each electromagnet has an attractive force on a moving center armature. Some of the problems facing electromagnetic variable

valve actuation (EVVA) technologies are high electric power demands, limited variable lift design, temperature sensitivity as well as obtaining soft-landing control [Lou, 2007].

VALEO has created a electromagnetic linear valve actuator that they claim is near ready for production [Picron et al., 2008]. This system has two modes of operation, commutation (slow) and ballistic (fast) valve actuation. They claim that the EVVA system is competitive with the mechanical equivalent. They also point out that engine with a regenerative braking system can almost entirely offset the electrical consumption of the valves [Frederic et al., 2010].

Different technologies have been compared in [Lang et al., 2005] and it has been determined that an electromagnetic valve train would cost 25% less than electrohydraulic systems for a similar gain in the extension of HCCI operating range.

2.2.6 Hybrid Systems

Research into combining cam phasing, electromagnetic valve train and electrohydraulic valve trains are also being investigated. One example is a hydraulic valve train that uses a hydraulic control and latching mechanism in conjunction with the two spring actuation of a electromagnetic valve train [Lou, 2007]. This system addresses the need for closed loop control and incorporates lash adjustment – two common problems in electromagnetic valve trains. A combination of camshaft and hydraulic systems is designed by [Wong and Mok, 2008] where a camshaft is the source of hydraulic power that actuates the valves. This system only requires low cost proportional valves and simplifies control scheme. A combination of a permanent magnet and an electromagnet uses less power at low speeds due to lower spring compression and spring force but uses the electromagnet at high speeds to compress the spring further to increase the spring force [Nagaya et al., 2008].

2.3 Experimental electromagnetic Actuators

The actuators used in the experimental set-up of this work are a hinged actuator design. A schematic of the double actuator used is shown in Figure 2.4 [Chladny, 2007] [Stolk and Gaisberg, 2001] where a left and right armature are each connected to separate valves. One double actuator is required for the intake and one is used for the exhaust resulting in a four valve per cylinder system as shown in Figure 2.5. Shown in Figure 2.4, each valve has closer and opener excitation coils and opener and closer as measurement coils which are used for valve position estimation. The valve spring is mounted in the cylinder head and opposes the torsion spring force. The armature has a rest position in the middle of the 8 millimeter range of motion. A control oriented model of the valve actuator is detailed in [Chladny, 2007] and is duplicated here for completeness as the model will be validated with the single cylinder engine results.

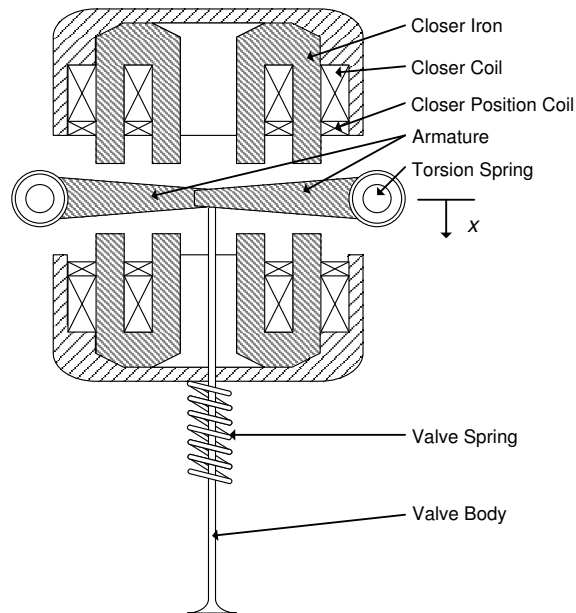


Figure 2.4: Cross section of the Marelli actuator used in the experimental set up [Chladny, 2007]

The valve actuator model consists of a electrical subsystem and a mechanical

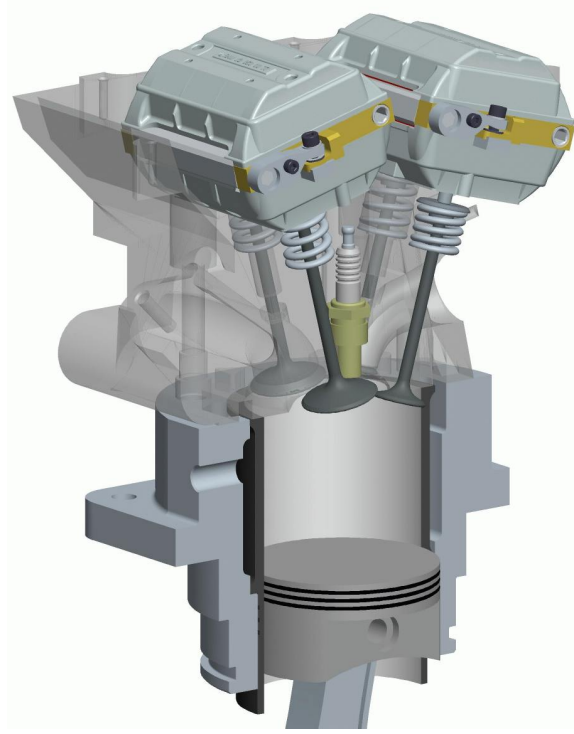


Figure 2.5: 3D model of Marelli actuators and head on a single cylinder engine [Chladny, 2007]

subsystem, where the position of the valve taken as the middle armature position as shown in Figure 2.4. Magnetic saturation occurs in this system and the flux linkage, $\lambda(x, i)$, which is dependant on the valve position, x , and the current, i , is given as

$$\lambda(x, i) = \psi(1 - e^{-ig(x)}) \quad (2.1)$$

where

$$g(x) = \frac{\beta}{\kappa - x} + \alpha \quad (2.2)$$

where the parameters $\psi, \beta, \kappa, \alpha$ are flux linkage model parameters identified by system identification and x is the valve position. The state space model of the valve actuator including magnetic saturation is described by

$$\begin{pmatrix} \dot{x}_1 \\ \dot{x}_2 \\ \dot{x}_3 \end{pmatrix} = \begin{pmatrix} \frac{x_1 g'(x_2) x_3}{g(x_2)} \\ -x_3 \\ -\frac{1}{m}(-x_3 b + (\kappa - x_2)k - F_v + F_g - \frac{l_m}{l_v} F_m(x_1, x_2)) \end{pmatrix} + \begin{pmatrix} \frac{e^{g(x_2) x_1} u}{\psi g(x_2)} \\ 0 \\ 0 \end{pmatrix} \quad (2.3)$$

where x_i ($i=1,2,3$) are the state variables chosen such that the state x_1 is the current i , x_2 is $\kappa - x$ (the position), and x_3 is the velocity. The input to one coil, u , is defined as $v - iR$. For soft landing control purposes, only the coil is important. The values of F_m , F_g , and F_v correspond to the magnetic force, gas force and valve spring pre-load respectively. The constants of b and k are the effective linear damping coefficient and spring constant. The output equation for the state space formulation is given by

$$y = [0 \ 1 \ 0] \begin{pmatrix} x_1 \\ x_2 \\ x_3 \end{pmatrix} \quad (2.4)$$

which results in the position as the output since this is what can be measured using the flux measurement coils.

2.3.1 Control Design

Typical of real time control, the highest level of the software consists of a state machine with stages of operation of the valves as shown in Figure 2.6. The state machine is initialized to the fail state at startup. Then the valves are swung to a closed state. From a closed position, the valves are triggered by the engine controller to move at the appropriate engine crank angle to obtain the desired valve timing as shown in Figure 2.6. Should an error occur the state machine transitions to the fail state to prevent damage to the valves.

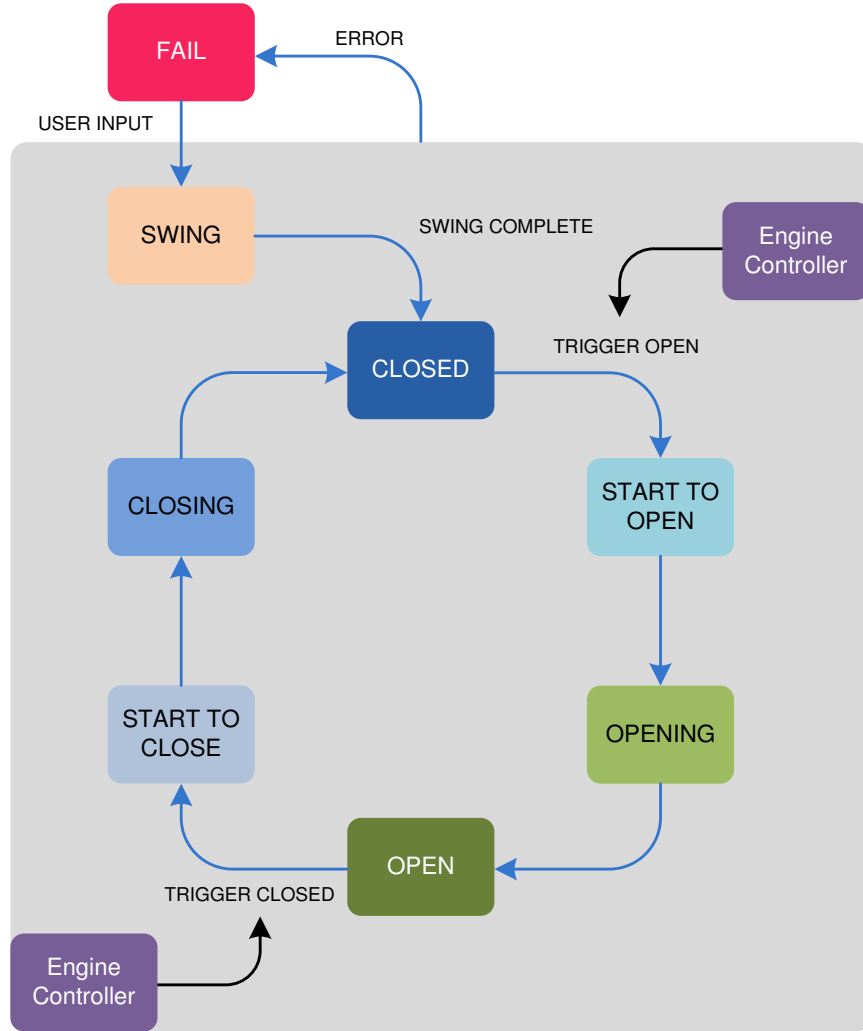


Figure 2.6: Valve state flowchart. Adapted from [Chung, 2005]

Closed loop position control occurs in the closing and opening states. The control methodology followed is shown in Figure 2.7 where the close-to-open and the open-to-close controllers used are illustrated. The difference between the two directions stems from the large variation in combustion gas forces when the valve opens which is compensated by a position-based feed-forward control.

Since valve position is not measured directly it is estimated using a magnetic flux based position sensor [Chladny and Koch, 2006]. To do this, the integrated secondary measurement coils which are concentric with the primary excitation coils are used to

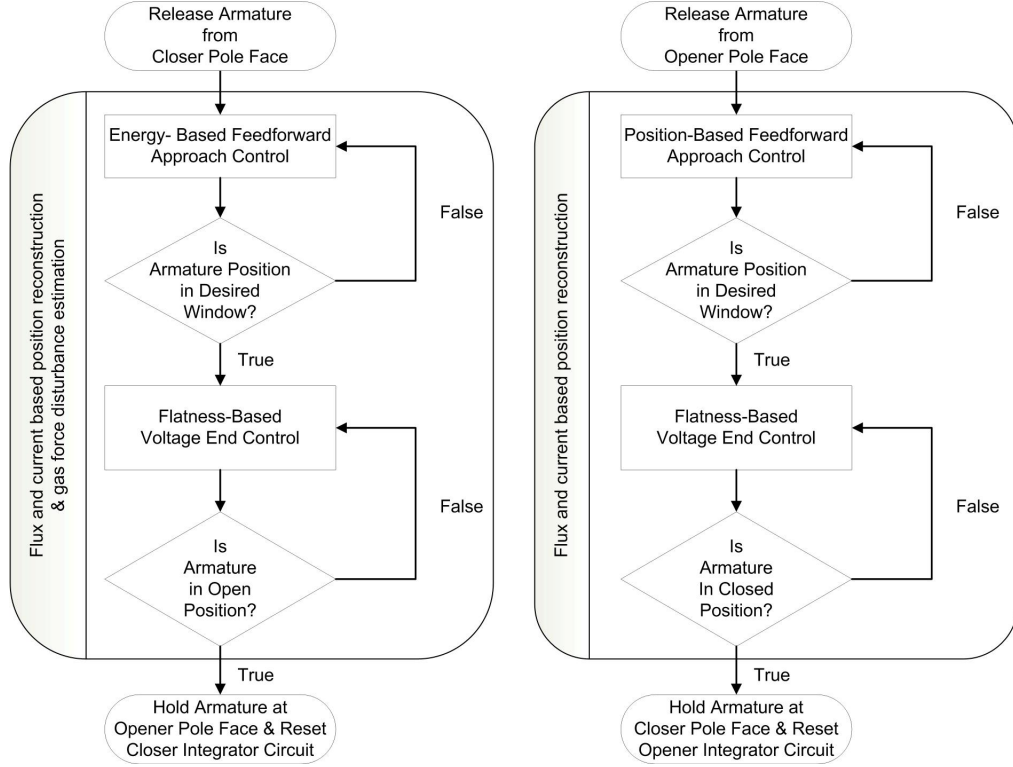


Figure 2.7: Controller flow chart [Chladny, 2007]

measure the induced voltage due to a change in magnetic flux from the primary coil.

Relating current, flux and integrated voltage to position as

$$x = \frac{\beta i}{\alpha i + \ln(1 + N_{ec}/\psi(\phi_0 + \int v_{fc} dt/N_{fc}))} + \kappa \quad (2.5)$$

the armature position x is calculated. The parameters β , κ , ψ and α are identified using nonlinear least squares fit of a 2-D finite element model of the actuator [Chladny et al., 2005]. In equation 2.5, i is the current, N_{ec} is the turns in the excitation coil, ϕ_0 is the initial flux condition, v_{fc} is the induced voltage in the flux coil, and N_{fc} is the turns in the flux coil.

For both opening and closing, flatness-based control [Chladny and Koch, 2008][Chung et al., 2007] is used since equation 2.3 is differentially flat. A differentially flat system is one with a state \mathbf{x} , here x_1, x_2, x_3 , of

dimension n , denoted $\mathbf{x} \in \mathbb{R}^n$, and m inputs, denoted $u \in \mathbb{R}^m$, can be parameterized by “flat” outputs y , denoted $y \in \mathbb{R}^m$, by defining a flat output of the form

$$y = \gamma(\mathbf{x}, u, \dot{u}, \dots, u^{(\alpha)}) \quad (2.6)$$

which allows the state and input to be expressed as a finite number of derivatives of the flat output

$$\mathbf{x} = \phi(y, \dot{y}, \dots, y^{(\beta)}) \quad (2.7)$$

$$u = \psi(y, \dot{y}, \dots, y^{(\beta)}) \quad (2.8)$$

For the solenoid valve the flat output, y , is taken as the armature position x_2 , and the input (voltage) can be shown to be related to the third time derivative of y . The resulting equation for the voltage is given by

$$v = \frac{l_v g(y)}{l_m i g'(y)} (\ddot{y} b + \dot{y} (k + 2F_m(y, i) \frac{g'(y)}{g(y)} - \frac{1}{\kappa - y}) + \dot{F}_g + y^{(3)} m) + iR \quad (2.9)$$

with l_m being radial distance from the armature pivot point to where the resultant opener magnetic force acts on the armature, and l_v being the radial distance from the armature pivot point to where the longitudinal armature and valve axes intersect. This constitutes a feedforward tracking but in order to compensate for disturbances a tracking error is implemented as $\tilde{y} = y - y_d$ with y_d being the desired trajectory. The linear error dynamics is chosen as

$$k_1 \tilde{y} + k_2 \dot{\tilde{y}} + k_3 \ddot{\tilde{y}} + \tilde{y}^{(3)} = 0 \quad (2.10)$$

where the coefficients k_i are chosen such that the characteristic equation is Hurwitz. Solving for $\tilde{y}^{(3)}$ and substituting into equation 2.9 yields exponential tracking of y to y_d .

2.3.2 Simulation Model

A schematic of a physics based control oriented simulation model shown in Figure 2.8 [Chladny, 2007] is used for model based control development. This is the top level of a hierarchical Simulink model. The power electronics, power supply, controller, plant as well as external gas force disturbance provide a realistic dynamical plant model for controller design. The “Testbench” sub-model consists of coil dynamics model, where the opener and closer voltages are used to relate to flux linkage and position to coil current. The magnetic force is a non-linear function of coil current and armature position [Chladny, 2007]. The actuator dynamics are also modeled using Newton’s Law with the coil dynamics and the gas force disturbance. The “Compressed Air Disturbance” model is a gas force disturbance that represents a measured combustion force in an engine. The “dSPACE 1103” sub-model contains the state machine as all the control and estimation algorithms. The “dSPACE 1103” block has the pulse width modulation (PWM) signals as outputs to the power electronics and has as inputs of the valve state. The “Power Electronics” amplifies the PWM signal using an H-bridge that results in a 42V, 0V or -42V signal to the primary coils of the valve actuators. The input to the high power transistors in the H-bridge is the PWM output of the controller which allows 0-100% duty cycle to be changed at each sample instant (50kHz on the actual system). The input to the entire simulation are the engine parameters, the in cylinder pressure trace and the valve state events (Open, Start Open, Opening, Closing, Start Closing Closed). The simulation records important variables including the position, velocity, opener and closer currents, and gas force estimate for comparison to experimental results. This model has been validated on

a test bench with compressed air which attempts to simulate real engine conditions [Chladny, 2007].

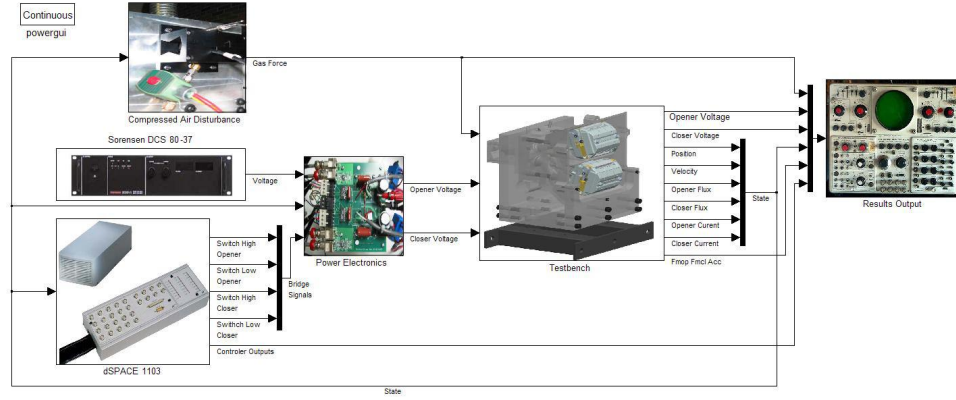


Figure 2.8: Simulink model of EVVA system and controller - Top level [Chladny, 2007]

2.3.3 EVVA Test Bench

Prior to the EVVA system being installed on the Ricardo Hydra Mark III engine, the head and actuators were mounted on an engine test bench [Chladny, 2007]. The test bench setup is shown in Figure 2.9. The setup contained a line from the building air supply to charge the cylinder volume for testing against simulated exhaust back pressure. The setup also measured the valve position using a laser sensor which acted as a reference to compare to the position estimate. This laser signal is not used for control (since it is not available on the real engine) but rather is used to validate the valve position obtained from the measurement coil of the flux as given in equation 2.5. Only the exhaust actuator was tested with this experimental apparatus.

The comparison of the EVVA test bench to the simulation results for the exhaust valve opening against one to five bar are compared in [Chladny, 2007] and duplicated here. This back pressure represents the engine operating from light to high load. Figure 2.10 shows how closely the simulation matches the test bench exhaust back pressures of one to five bar. The test bench results use the flux measurement coils

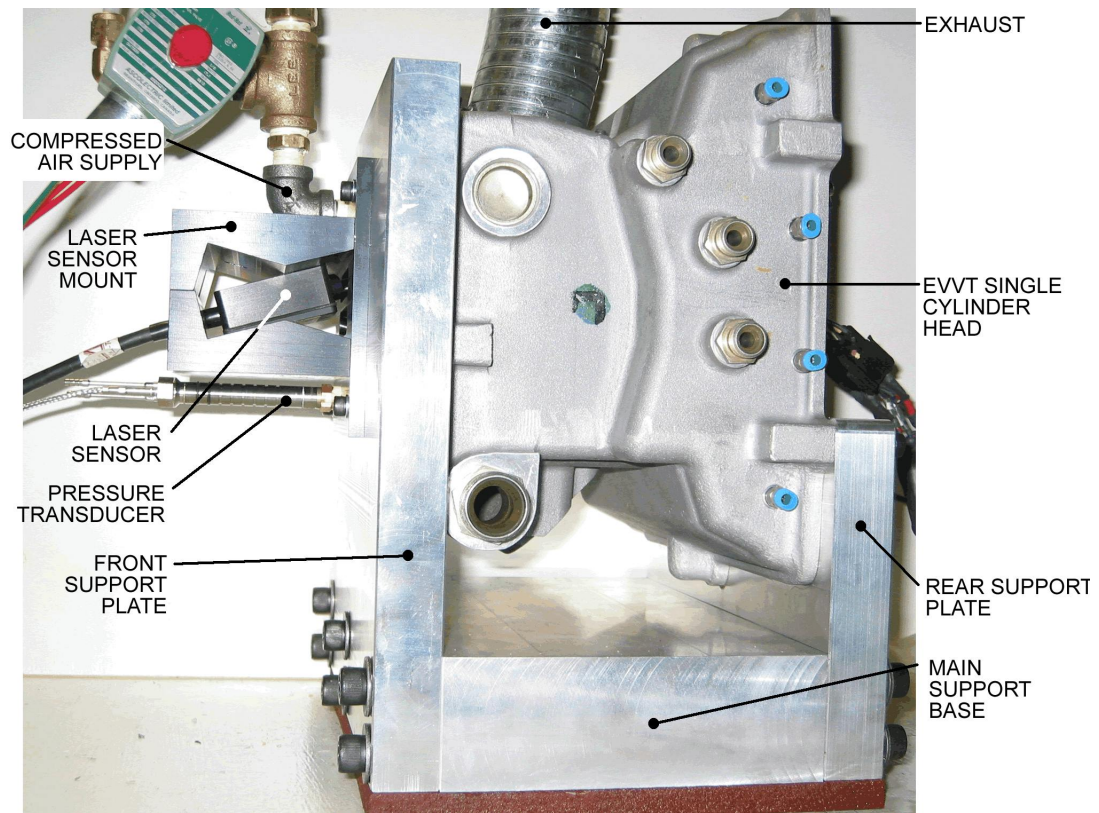


Figure 2.9: EVVA test bench setup [Chladny, 2007]

for feedback control and observer disturbance rejection. The laser position is plotted in Figure 2.10

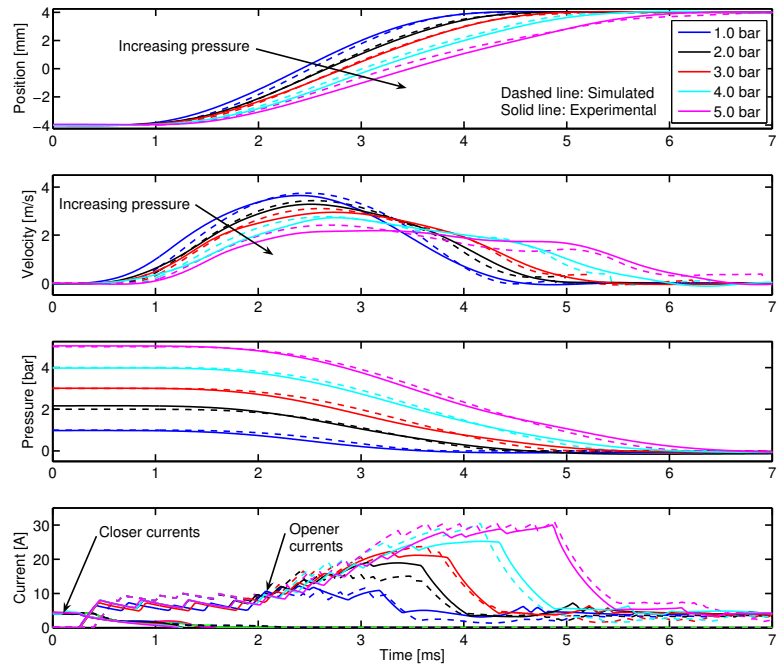


Figure 2.10: Simulated and test bench results using flux based feedback. Figure 7.25 in [Chladny, 2007]

CHAPTER 3

EXPERIMENTAL SETUP, TESTING PROCEDURE & DATA ANALYSIS

This chapter describes the single cylinder engine. The basic configuration is described in 3.1. There are two configurations for variable valve timing used in this thesis. The first configuration is with cam phasing and is described in 3.2, the second is with EVVA and is described in section 3.3. The data acquisition and control systems are then described. Several of the sensors have been calibrated and the details of the calibration are listed in Appendix C. The data acquisition systems, dynamometer controller, valve controller, and engine controller are described in section 3.4.

3.1 Basic Engine Assembly

The engine block and crankshaft is a Ricardo Hydra Mark III. The connecting rod bearing was ground down for the Carrillo Industries connecting rod [Audet, 2008]. A custom made cylinder jug allows for an adjustable compression ratio by turning a ring on the jug that raises or lowers the head which changes the clearance volume. The jug has a custom wet sleeve from Darton International Inc. The crankshaft is coupled to a dynamometer using a shaft and two flexible couplings.

An active dynamometer setup is used in this engine consisting of a 37kW DC

electric motor. The torque (or speed) is controlled with a Eurotherm Drives 590+ drive controller. The torque is measured with a Interface Inc. SSM-A-J-200N load cell [Audet, 2008] and the calibration can be found in Figure C.11.

Figure 3.1 illustrates a schematic of the single cylinder engine without the oil and coolant loops. The intake of air flows through a Cussons Technology P7200/108 laminar air flow meter which is then led into a large barrel to dampen pressure oscillations. A Flo-Tech ITB integrated throttle body and Actuator is then used to control the amount of air before a Eaton Automotive model MP45 supercharger increases the pressure. The supercharger is powered by an electric motor independent of the crankshaft. The intake plenum with a 600W electrical heater follows the supercharger. Two port fuel injectors of iso-octane and n-heptane inject fuel directly on the intake valve. The engine exhaust is directed out of the building. Exhaust temperature, air-fuel ratio, emissions sample and exhaust pressure are taken directly after the exhaust port. The air-fuel ratio is measured with a ECM AFRecorder 1200 wide band oxygen sensor.

The oil and coolant schematic of the engine can be seen in Figures 3.2 and 3.3, respectively. Both coolant and oil temperature are Proportional-Integral-Derivative (PID) controlled in ADAPT software which is further described in section 3.4.

3.1.1 Sensors

A schematic of the sensors is shown in Figure 3.4. Engine vibration is measured with a Bosch Model 261-230-120 vibration sensor which is mounted beside the cylinder jug. Temperature measurements are made with J and K type thermocouples and the pressures are measured with Valedyne P305D pressure transducers. Sample calibrations of the pressure transducers can be found in Figures C.3 to C.10 in Appendix C. The engine speed is measured with a BEI Industries XH25D-SS-3600-T2-ABZC-7272-SM18 shaft encoder which has 0.1 crank angle degree (CAD) resolution and is used

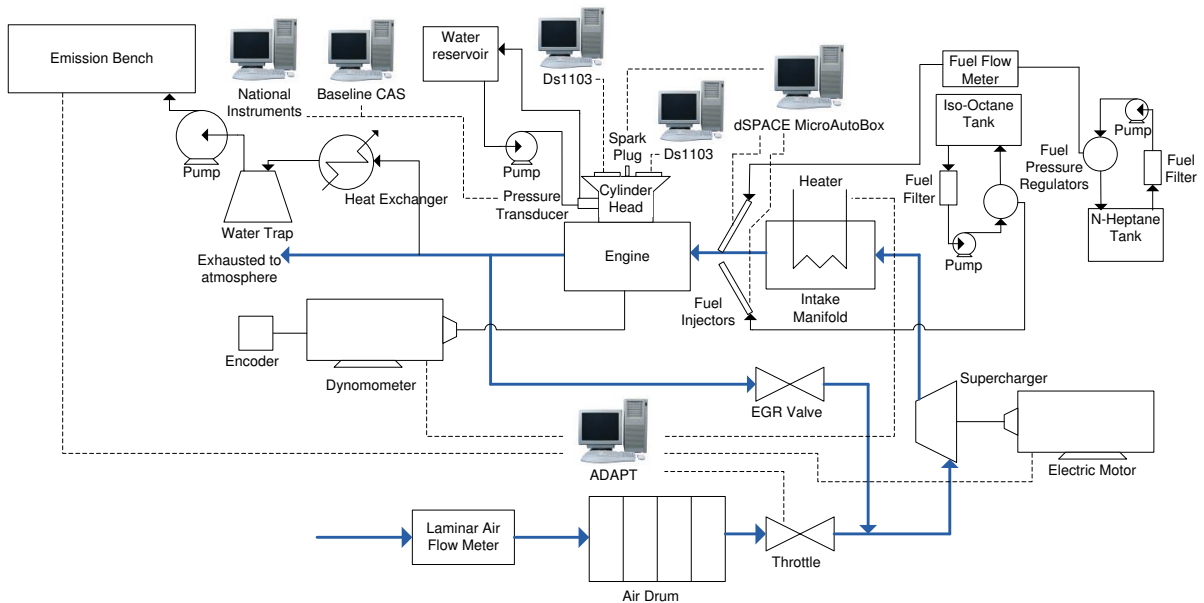


Figure 3.1: Hardware schematic for the Ricardo single cylinder engine and corresponding Computer systems

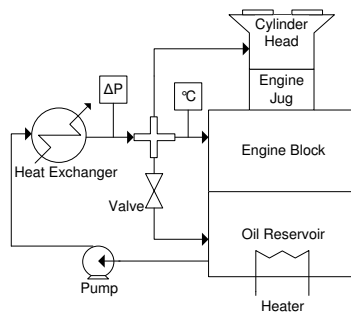


Figure 3.2: Oil supply schematic for the Ricardo single cylinder engine

in timing of crank based parameters for combustion analysis.

3.2 Single Cylinder Engine - Cam Phaser Head

The Cam Phaser setup is detailed in [Audet, 2008] with the specifications in Table 3.1. The head is a production 2007 Mercedes E550 modified for a single cylinder engine. It has four valves per cylinder and cam phasing that is independent for the intake and exhaust valves. However, since the dynamic response of this system is constant

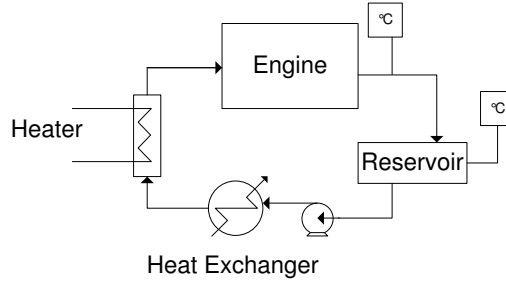


Figure 3.3: Coolant supply schematic for the Ricardo single cylinder engine

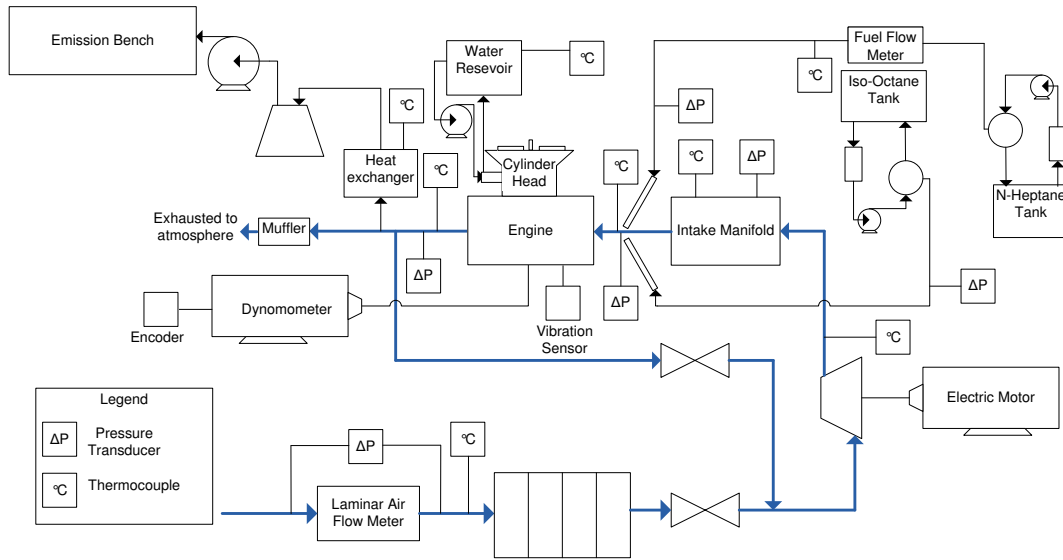


Figure 3.4: Sensor schematic for the single cylinder engine

as a function of time, at higher engine RPM, the cam phasing takes more crank angle degrees (CAD). The CAD cited in this chapter are measured from top dead center (TDC) of combustion, with the prefix *b* or *a* denoting “before” or “after” for bTDC and aTDC, respectively. A diagram of the possible valve timing with the Cam Phaser head is shown in Figure 3.5 with bottom dead center (BDC) denoting location of lowest piston decent. The possible valve timing range for intake valve closing (IVC) and exhaust valve closing (EVC) is shown in Table 3.1. The intake valve opening (IVO) and exhaust valve opening (EVO) values are fixed 40 degrees before the IVC and EVC values respectively.

The cylinder pressure transducer is a water cooled Kistler 6043A60 which uses factory

Table 3.1: Configuration of the Ricardo Single-Cylinder Engine With Cam Phasing

Parameters	Values
Bore \times stroke [mm]	97 \times 88.9
Compression Ratio	12
Displacement [L]	0.653
Valves	4
IVC	118-158 bTDC
EVC	307-345 aTDC

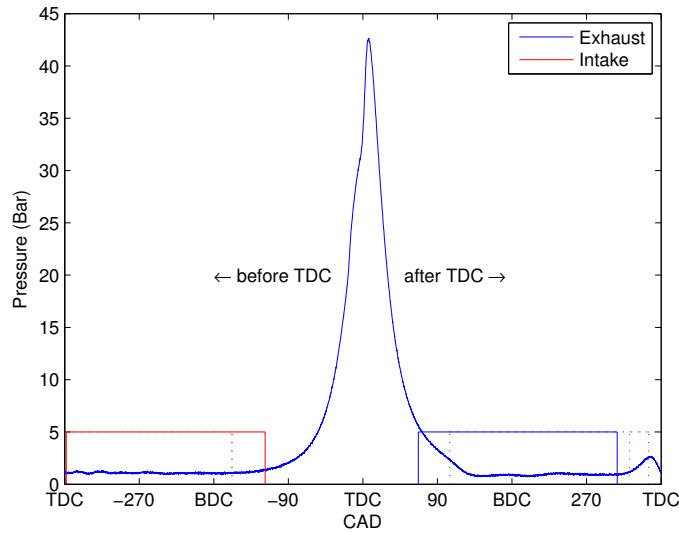


Figure 3.5: Valve Timing Diagram for Cam Phaser Head

calibration settings as described by [Audet, 2008]. The piston for the phaser head is shown on the right side of Figure 3.6.

3.3 Single Cylinder Engine - EVVA Head

The EVVA setup in this experiment is from an experimental (non-production) single cylinder cylinder head and valve actuators produced by Daimler AG. Although the engine has four valves per cylinder, only one intake and exhaust valve are utilized in all reported tests while the other two are held shut. The experimental setup is designed to allow relatively easy swapping of the EVVA and the phaser head. The

main components that must be changed are: the cylinder pressure transducer, intake and exhaust adaptors, the piston, cylinder head and head gasket. The EVVA piston has larger reliefs to allow for a free running engine and a picture of this piston is shown in the left side of Figure 3.6. A Kistler 6061B piezoelectric in-cylinder pressure transducer is used; the calibration for this transducer can be found in Figure C.2. The addition of intake and exhaust adaptors allow for the use of the same intake/exhaust system for both heads. Figure 3.7 shows the intake and exhaust adaptors.



Figure 3.6: EVVA and cam-phaser pistons

Some modifications to the oil and coolant system were necessary for the switch to the EVVA system. Oil which is regulated by a needle valve into the EVVA head for lubrication of the actuator, valve stem and valve spring is drained by holes on one side of the head as seen in Figure 3.8. Plumbing has not been added to the drain back to the reservoir. Instead, oil is added only as necessary and changed when needed. In order to simplify the switching of the engine setup back to the phaser setup, the screw on the cylinder jug, used for compression ratio change, was not altered. The final specifications for the engine are listed in Table 3.2. The valve timing are set to the default values in Table 3.2 at engine start.

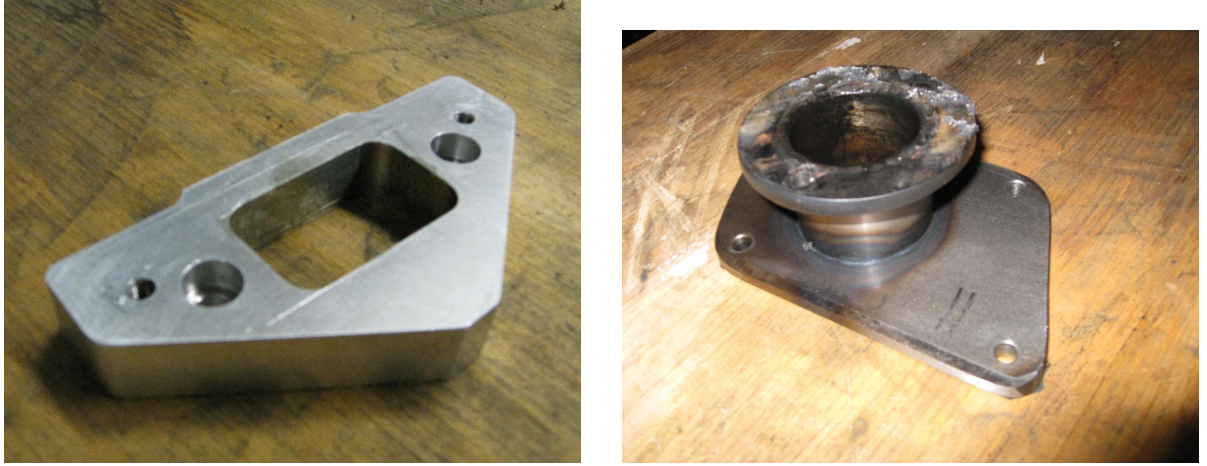


Figure 3.7: Intake and exhaust manifold adaptor

Table 3.2: Configuration of the Ricardo Single-Cylinder Engine With EVVA at Engine Start

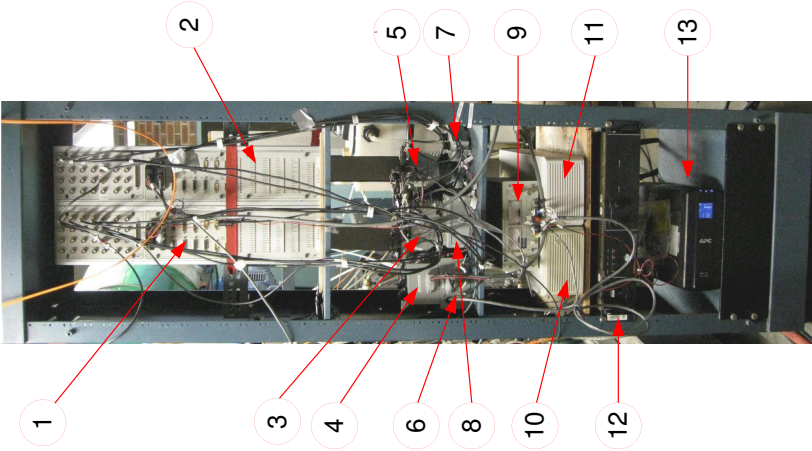
Parameters	Values
Bore \times stroke [mm]	97×88.9
Compression Ratio	13.9
Displacement [L]	0.653
Valves	2
IVO [aTDC]	-300
IVC [aTDC]	-180
EVO [aTDC]	180
EVC [aTDC]	300

3.3.1 EVVA Control and Power Electronics Bench

The control and power electronics for the EVVA system is placed on a rack mount for space savings. It is placed in close proximity to the valve actuators on the cylinder head in order to reduce the length of wire leading to the actuators to keep the inductance of the wires to a minimum. The apparatus is illustrated in the left hand side of Table 3.3 while a description of each numbered component is on the right hand side.

The values of the current limiter for both the intake and exhaust are set to 14A for 0.3 seconds in order to prevent damage to the actuators. If the current exceeds the limit the Sorenson power supply is disabled [Chladny, 2007]. The Sorenson power

Table 3.3: Control and power electronics for EVVA system



Number	Component
1	Intake dSPACE breakout box
2	Exhaust dSPACE breakout box
3	Intake power electronics
4	Opto-isolator
5	Exhaust power electronics
6	Analog integrator
7	Exhaust current limiter
8	Intake current limiter
9	Hewlett-Packard 6236B triple output power supply
10	dSPACE1103 controller for intake
11	dSPACE1103 controller for exhaust
12	Sorenson DCS 80-37 power supply
13	APC back UPS Pro 1000

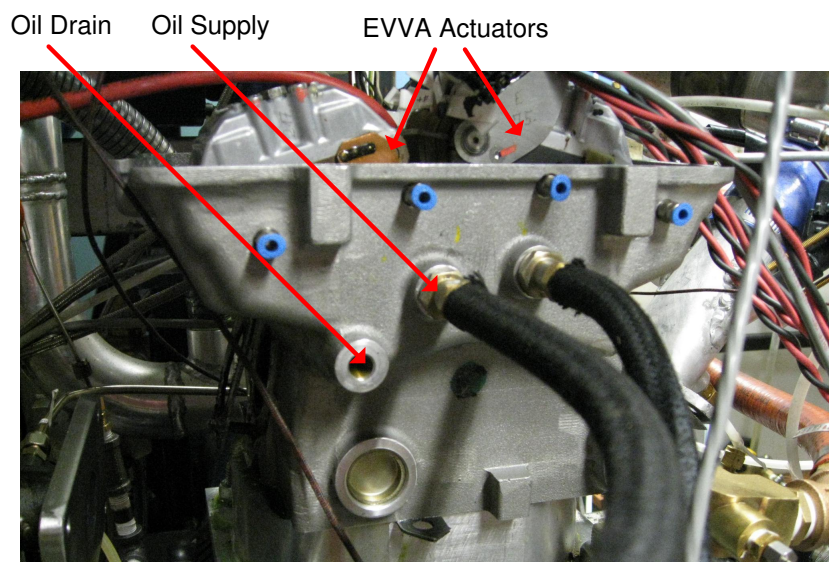


Figure 3.8: Oil supply and drain on EVVA setup

supply is set to 44.7V to account for losses through the bridge and supply the coil with 42V [Chladny, 2007]. A schematic of the control and power electronics for the EVVA intake and exhaust motion control is illustrated in Figure 3.9.

3.4 Data Acquisition and Control System

The data acquisition is performed by ADAPT, CAS, National Instruments, with a dSPACE microAutoBox system as the engine control. Two dSPACE 1103 systems are used for motion control of the EVVA valves - one for each valve. These systems are described below.

3.4.1 ADAPT System

The A&D ADAPT system is a hardware and software package used to control the main parameters of the engine test bed [A&D Technologies, 2003]. Control of the dynamometer speed, the supercharger pressure, the throttle position, and the coolant and oil temperature set points which have PID control loops is performed. All the

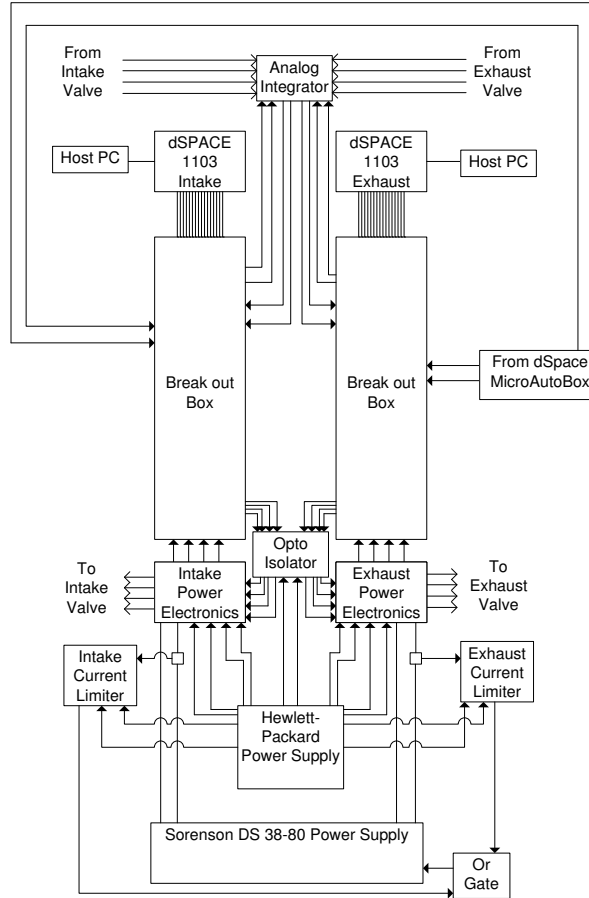


Figure 3.9: Control and power electronics schematic for EVVA system

temperature and pressure measurements (except for the in cylinder pressure transducer), the air flow and the fuel measurements are collected at 10Hz. The ADAPT system also is programmed to perform emission bench calibration and subsequent emissions measurement.

3.4.2 CAS System

The A&D CAS system [A&D Technologies, 2001] is used for crank angle data acquisition and cycle-by-cycle analysis. This system records parameters on a CA basis of 0.1 degree. It records the full cylinder pressure trace as well as calculating values of IMEP, CA50 and displaying peak pressure.

3.4.3 dSPACE MicroAutoBox System

The dSPACE MicroAutoBox system [dSPACE, 2005] is a ds1401 controller which is programmed using MATLAB Simulink and controls the two fuel injectors and timing, fuel octane, spark timing, and cam phasing or EVVA timing at a sampling rate of 1kHz. Timing for these commands are interrupt driven where a 36-1 toothed wheel provides the crank angle as well a one pulse per cycle signal determines the location on the engine cycle. Data is recorded for 200 cycles on a per cycle basis.

3.4.4 National Instruments

The National Instruments (NI) PCIe-6341 data acquisition card is used in conjunction with LabVIEW v9.0 program [National Instruments, 2009]. This program monitors and records the cylinder pressure trace as well as the vibration sensor. The pressure trace and vibration sensor are recorded on a 0.1 CAD basis from -89.90 aTDC of combustion to 90.1 degrees aTDC for at least 200 cycles. This system has enough memory to record up to 3000 cycles if needed.

The NI cylinder pressure trace is used as a safety to prevent damage to the engine in case a valve fails and compression is lost. The NI LabVIEW program takes the maximum recorded cylinder pressure and compares it to a standard value of 8 Bar. If the pressure is higher than 8 Bar, compression exists and thus the valves are working and a high voltage reading of 4V is sent to the dSPACE MicroAutoBox where fuel and spark are enabled. If the pressure drops below 8 Bar, NI voltage output is switched to 0 Volts resulting in the spark and fuel being disabled on the dSPACE MicroAutoBox.

3.4.5 dSPACE 1103 Controllers

Each intake and exhaust valve is controlled through a stand alone dSPACE DS1103 Power PC (PPC) target controller board [dSPACE, 2008] which is each linked to its

own host PC running dSPACE ControlDesk 2.4 on Windows XP operating system. Two way communication between the host and target is achieved through an optical cable. The control program, written in C [Chladny, 2007], measures the coil voltages, currents, flux linkage signals, pressure signal and executes the control algorithm at 50kHz while lower priority tasks such as initialization and processor temperature monitoring are done at 10kHz. Data acquisition is done at 50kHz for 5 seconds, recording 13 parameters including the cylinder pressure trace. The valve controllers maintain the correct bank angle valve timing as they are triggered by the engine controller.

3.5 Testing Conditions

All the engine operating conditions that are tested are listed in Table 3.4. To achieve HCCI, the engine is first warmed up in SI mode, then the transition to HCCI mode is obtained by increasing the intake manifold pressure with the supercharger, disabling spark, reducing octane number, and increasing intake temperature with a heating element. All test conditions are performed with constant commanded engine speed, intake manifold pressure and temperature. For SI testing with the EVVA head, the engine is motored until oil and coolant temperature reaches steady state with the valves unactuated to ensure a smooth start to SI combustion. The spark angle is set to 25 degrees bTDC and 100 ON fuel is used and the valves are then actuated according to the commanded timing.

3.6 Measurement Calibrations

For both cylinder heads, calibration of sensors has been performed. Each pressure transducer is calibrated with a dead weight tester. The Kistler in cylinder pressure transducer signal is reset every cycle with the CAS system when the intake valve is

Table 3.4: Engine Operating Conditions

Operating Condition	Cam Phaser Head	EVVA in SI	EVVA in HCCI
Engine Speed [RPM]	1005 - 1150	680-810	710-790
Intake Temperature [°C]	45-65	23.7-39.1	88-112
Intake Pressure [kPa]	100-120	59.6-98.9	63.7-100.4
Equivalence Ratio	0.32-0.36	0.88-1.09	0.19-0.43
Coolant Temperature [°C]	60-70	22-55	45-60
IVC [bTDC]	118	160-200	160-210
EVC [aTDC]	345	300	300-340
ON [PRF]	0-30	100	0-10
Throttle [%]	100	0	50

open. Details on the emissions bench calibration as well as the pressure transducer calibrations are found in Appendix C

CHAPTER 4

KNOCK DETECTION AND CONTROL¹

This chapter describes a standard knock detection method and then compares it to a wavelet transform method for knock detection. The continuous and discrete wavelet transform are considered. Real time detection and control is implemented with a Proportional Integral (PI), Feed-forward (FF), and PI with FF (PI+FF) controller. The cam phasing head is used on the engine.

4.1 Knock Frequency

A range of data is collected in HCCI with the operating conditions specified in Table 3.4 with varying degrees of knock. Comparing two cases, a high knock (Case A) and low knock case (Case B), is found to provide insight into the knock phenomena. The two cases are run at the same operating conditions except Case A has more fuel injected. Figure 4.1 shows the cylinder pressure for a typical cycle for Case A and Case B as a function of crank angle in degrees after top dead center (TDC). The pressure trace for Case A shows a significant high frequency pressure oscillation starting near the location of peak pressure. These high frequency pressure waves are denoted as knock and are not desirable as they can damage the engine [Heywood, 1988]. It should be noted that the location of the pressure transducer effects the intensity of

¹This chapter is based on Mashkournia et al. [2011] paper.

knock detected and that the location of the sensor is dictated by engine geometry. The high frequency oscillations are found from $0 \leq CAD \leq 50$ for this engine. This range is part of the expansion phase which is taken from TDC to the exhaust valve opening.

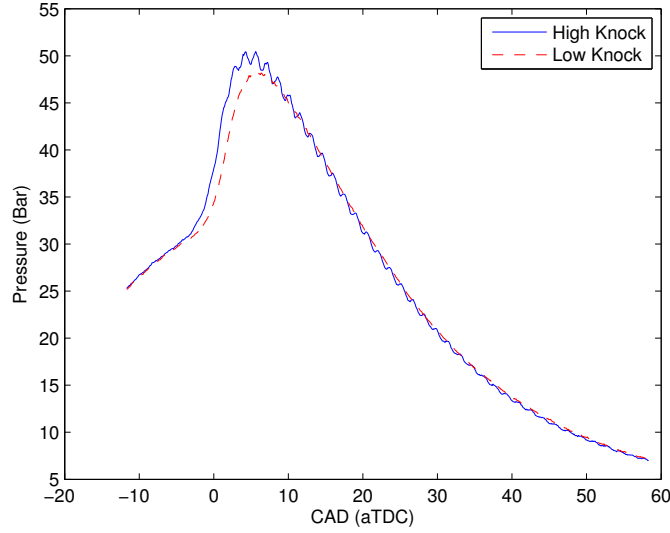


Figure 4.1: Pressure signal for: Case A - high knock; Case B - low knock

The frequency of the pressure oscillations in the combustion chamber induced by the nonuniform combustion can be predicted using acoustic theory, as originally presented in [Draper, 1933]. There is generally one dominant mode of oscillations present in the pressure oscillations which tends to be the first circumferential mode for most engines. The first circumferential mode is the lowest frequency shown in Figure 4.2. The expected frequency of this mode is calculated by:

$$f_{m,n} = \frac{c\rho_{m,n}}{\pi bore} \quad (4.1)$$

where $f_{m,n}$ is the Pressure oscillation frequency in Hz, m is the order of the circumferential mode, n is the order of the radial mode, c is the speed of sound in m/s, $\rho_{m,n}$ is a factor describing the mode, and $bore$ is the cylinder bore diameter

in meters. The speed of sound is approximated as 950 m/s [Borg et al., 2006]. The modes predicted for this engine from the acoustic theory are calculated and used for comparison with Fourier techniques and the wavelet methods. For the given engine bore size of 97 mm, the oscillation frequencies, in kHz, for the various modes are shown in Figure 4.2. A more detailed analysis of the modes of oscillation can be found with a geometry describing a more modern pent roof style 4 valve combustion chamber [D.Schroll et al., 1998]. In this work, the dominant mode is found to be the first circumferential mode, $\rho_{1,0}$ with $f_{1,0} = 5.7$ kHz, throughout the majority of the expansion stroke.

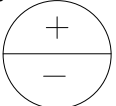
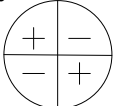
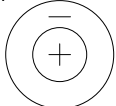
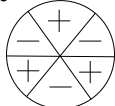
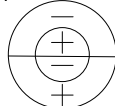
m,n	1,0	2,0	0,1	3,0	1,1
					
$\rho_{m,n}$	1.84	3.05	3.83	4.20	5.33
$f_{m,n}$ (Khz)	5.7	9.5	12	13	17

Figure 4.2: Frequency modes in a cylinder

4.1.1 Knock Benchmark

As the pressure transducer is the most direct measurement of the pressure oscillations induced by knock, this transducer is used for knock measurement. A commonly used benchmark method for knock identification is the value of the root mean square power (RMS) of the pressure signal, in the frequency range of the knocking, typically 4-7 kHz [Borg et al., 2006]. The value of P_{RMS} is defined by

$$P_{\text{RMS}} = \left(\frac{1}{M} [\hat{p} \cdot \hat{p}] \right)^{\frac{1}{2}} \quad (4.2)$$

Here the value of \hat{p} has been determined by bandpass filtering of the pressure trace using a 10th order Butterworth filter, with a pass band of 3-10 kHz and M is the

number of pressure points collected ($M=1800$ here). The knock index, K_{PSD} , is determined from the power spectral density (PSD) using an averaging method around the first and second mode of the knock frequencies (3 kHz to 10 kHz) as

$$K_{\text{PSD}} = \left(\frac{\sum_{i=n_l}^{n_h} \text{PSD}}{n_h - n_l} \right)^{\frac{1}{2}} \quad (4.3)$$

Where n_l and n_h are the frequency bins corresponding to 3 and 10 kHz, respectively. Figure 4.3 shows the relationship between the P_{RMS} and K_{PSD} for each of the 300 engine cycles of high knock (case A) and 300 cycles of the low knock (case B). It can be seen that there is an overlap of the knock index from the high knock case to the low knock case which indicates that there is inherent variability in the amount knock from cycle to cycle [Vressner et al., 2003]. The line of best fit in Figure 4.3 is determined using the method of least squares.

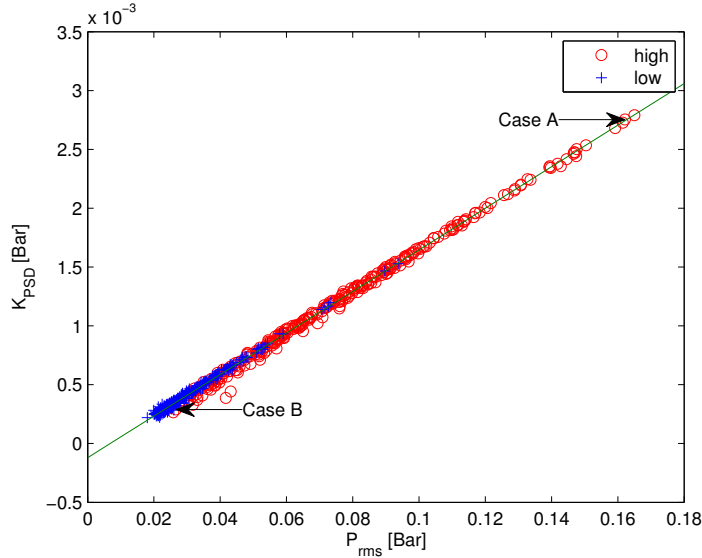


Figure 4.3: Comparison of pressure PSD to benchmark for both high (case A) and low (case B) knock

4.1.2 Continuous Wavelet Transform

The Continuous Wavelet Transform (CWT), unlike the Fourier transform, is a transformation with a basis function that is non-periodic and localized in time. To perform the wavelet transform, the basis function is translated and is scaled(stretched/compressed), and correlated with the signal. The continuous wavelet transform is given by [Chui, 1992]

$$X_w(a, d) = \frac{1}{\sqrt{|a|}} \int_{-\infty}^{\infty} x(t) \varphi^*\left(\frac{t-d}{a}\right) dt \quad (4.4)$$

where a is the scale, d is translation, ψ is the mother wavelet and $*$ denotes the complex conjugate. By cross-correlating the basis function of different time shifts and scales with the signal, the wavelet coefficients indicate the frequency spectrum. For a continuous signal both the time shift and scale can be varied continuously. In practice, using sampled data, the time shift can only be reduced to the sample rate and a finite number of scales (frequency equivalent) are chosen to approximate a continuous wavelet transform (CWT). The relationship between scale, s , and frequency, F_{scaled} , is given by

$$F_{scaled} = \frac{F_{center}}{s\Delta} \quad (4.5)$$

where F_{center} is the center frequency of the wavelet chosen, and Δ is the sampling frequency of the signal.

The CWT with a scale range of 0.5 to 21.5, converted to pseudo-frequency (on the Y-axis) for high knock and low knock can be seen in Figure 4.4. The resulting CWT coefficients are displayed as blue for low correlation or red for the highest correlation to the chosen wavelet. Using the complex Morlet wavelet [Lin and Qu, 2000] it can be seen that in the heavy knock case there is a range of frequencies identified about the combustion event. These frequencies range from 4.5 kHz to 9 kHz, corresponding

to the expected knock frequency, with the peak intensity at 5.7 KHz. If the CWT wavelet coefficients for the no knock case are plotted on the same scale, they are too small to be seen. Instead, in Figure 4.4 (b), the scale magnitude is reduced by a factor of 10 compared to Figure 4.4 (a) and shows that these frequencies are negligible. The peaks that can be seen at -90 and -10 CAD are most likely artifacts of the signal processing technique. Thus the CWT method can detect knock and can quantify it by the magnitude of the wavelet coefficients. However, the CWT method is computationally intensive and thus is suitable for off-line analysis. For on-line real time knock detection the discrete wavelet transform is used as it can be efficiently implemented as a filter bank.

4.1.3 Discrete Wavelet Transform

The Discrete Wavelet Transform (DWT), with a Daubechies-8 (16 coefficients) basis function, is used to analyze the knock signal. A three level filter bank is created where the signal is decomposed into the detail (high frequency) and approximation (low frequency) coefficients. The third level decomposition is shown in Figure 4.5 with CAD on the X-axis and frequency ranges on the Y-axis with the color indicating the magnitude of the DWT coefficient.

This format is similar to the CWT plots for both high and low knock cases. The frequency range of 3.57 to 7 kHz is the knock frequency range and is thus the important range to compare for Case A and Case B. It can be seen that the knock frequency of 5 kHz is seen in the DWT plot for the high knock case but is absent in the low knock case. Thus the DWT contains the important knock information, similar to the CWT. The maximum of the signal in the 3.75 to 7.5 kHz range is taken to be the knock index and is used for real time knock detection. The knock index is recorded along with the pressure trace in order to compare the DWT detection method to the P_{RMS} method. Figure 4.6 compares the real time DWT detection method to the P_{RMS}

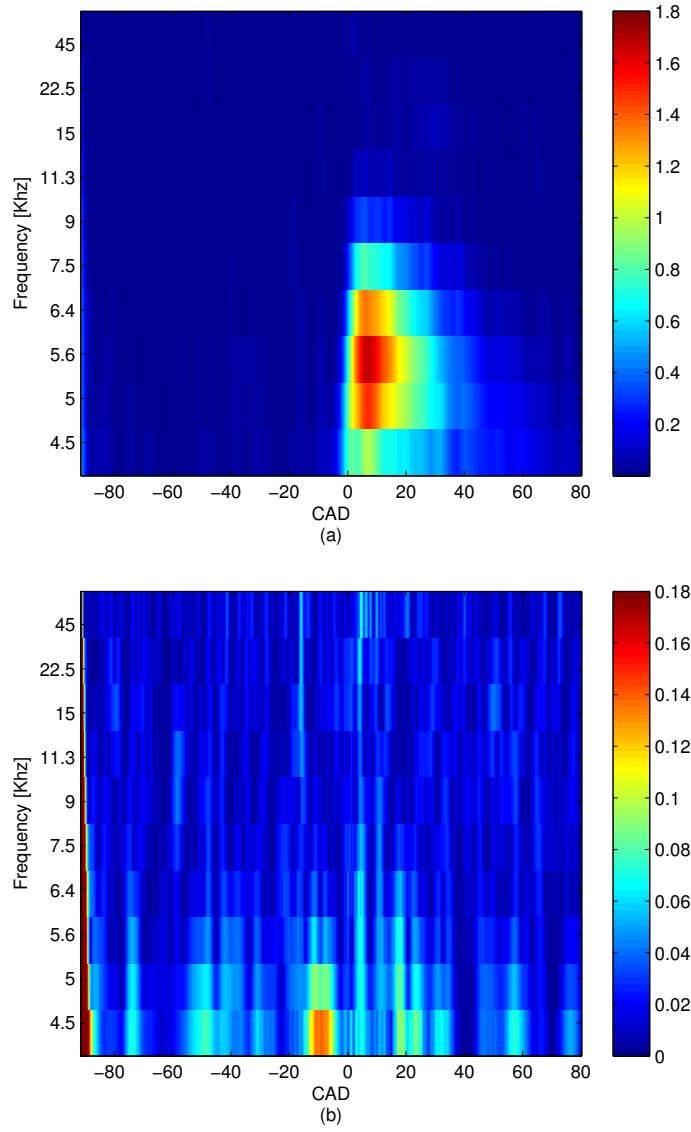


Figure 4.4: CWT Morlet coefficients for (a) high knock (case A) (b) low knock (case B)

method for each of the 300 engine cycles of both high (case A) and low knock (case B) and a linear correlation is seen. However, the correlation contains more scatter than the P_{PSD} method. This is attributed to the wavelet chosen and its correlation to the shape of the knock oscillations. Using a wavelet based on the shape of the pressure oscillation itself may offer better results [Zhang and Tomita, 2001]. Thus there is a trade off between complex wavelets with number of coefficients which give

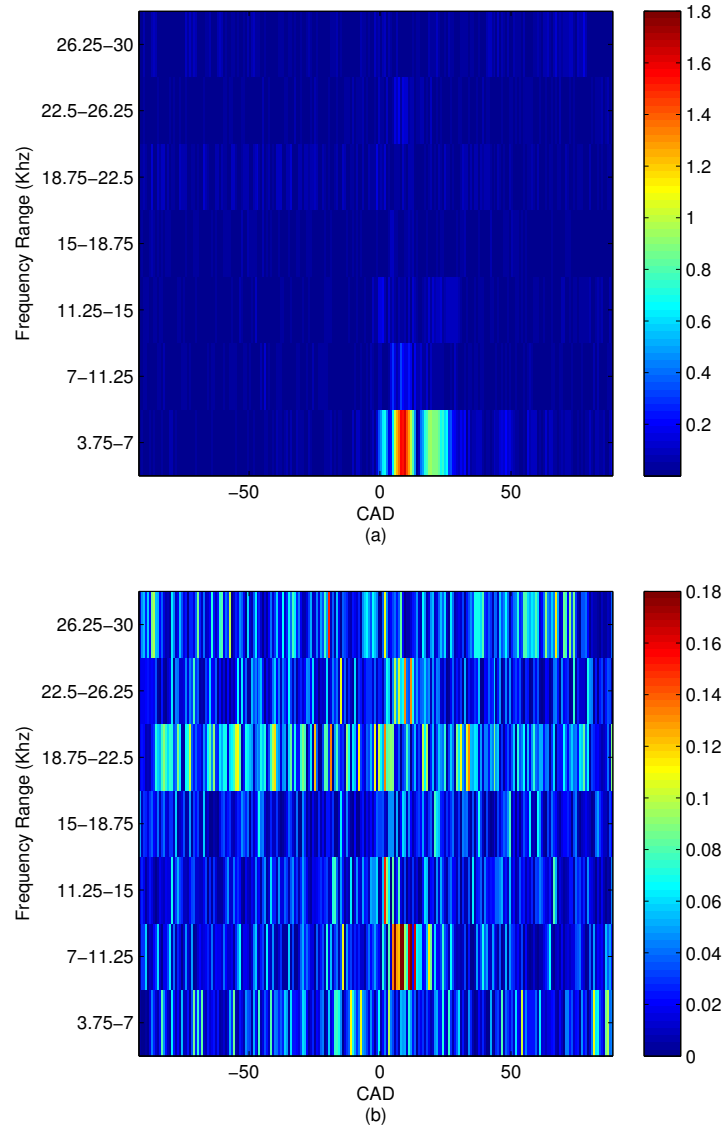


Figure 4.5: DWT colored coefficients for (a) high knock (case A) (b) low knock (case B)

high accuracy and simplicity of the mother wavelet which may be prone to noise. The DWT method is implemented as a filter bank which takes 2 ms to calculate (in LabVIEW on a 2.7 GHz processor). With the engine running at 1000 RPM the cycle time is 120 ms so the DWT method can be easily implemented in real time.

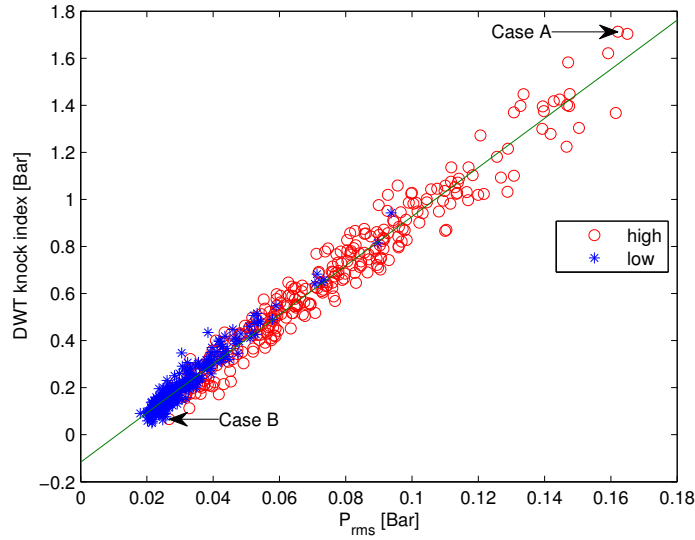


Figure 4.6: Comparison of DWT coefficients to benchmark for both high (case A) and low (case B) knock

4.2 Knock Control - Cam Phaser Head

On the single cylinder engine with the cam phasing head running in HCCI, knock is induced into the system by increasing the fuel injection pulse. The fuel injected energy is increased by 0.035 kJ, from 0.6611 kJ (case A) to 0.6961 kJ (case B), at an operating point near knock. The engine speed is 1000 RPM and other conditions are as specified in Table 3.4. The step in fuel energy is defined to occur from cycle 0 to cycle 1. To compare control methods, the normalized standard deviation, denoted σ_2/σ_1 , where σ_1 is the standard deviation of the knock level before the fuel jump and σ_2 is the standard deviation of the knock level after the fuel jump is given for each control case. As well, the normalized deviation from the desired knock value, denoted κ_2/κ_1 , where κ_1 is the deviation from the knock level set-point before the fuel jump and κ_2 is the deviation from the knock set-point after the fuel jump each normalized around the set point of 0.18 bar is given for each case as well.

In Figure 4.7 the fuel energy is stepped up while keeping the octane number constant

at 5.3. The resulting increase of knock without any control, with a five cycle moving average due to the high cyclic variation, is shown in Figure 4.7. The ratio of σ_2/σ_1 is 2.17 and κ_2/κ_1 is 1.79 for the no control case.

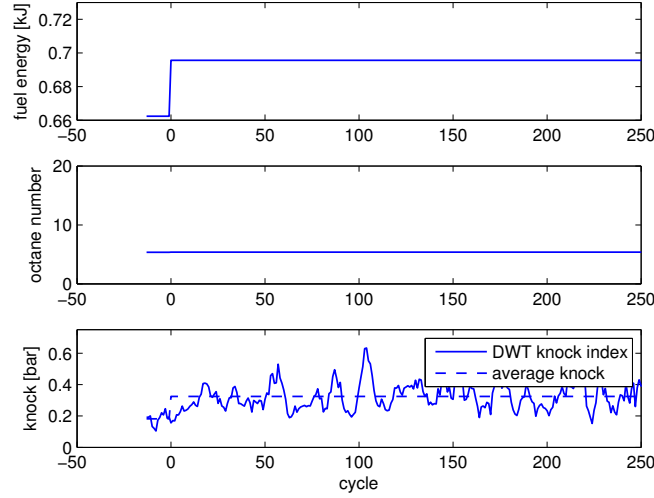


Figure 4.7: Knock level response to step in fuel energy - no control

To control the knock level despite a step in fuel energy, these three controllers are examined: Feed-Forward (FF), Proportional Integral (PI), and PI+FF. A block diagram of the overall control system is shown in Figure 4.8 with switches to be able to turn the individual PI and FF controllers on or off. The control actuation is the fuel octane number which is changed using dual injectors of n-heptane and iso-octane. The fuel octane has been shown to directly affect knock[Audet, 2008]. The fuel injection event is performed while the intake valve is closed (TDC = 0 degrees). This was done to avoid injecting with an open valve and to allow the fuel to evaporate. The desired knock value from the DWT method was set heuristically to 0.18 bar based on auditory and visual information from the real time cylinder pressure trace during testing. There are 16 cycles from the high knock case in Figure 4.6 which are less than the 0.18 bar set point and 168 of the 300 cycles of the low knock case are below the heuristically determined set-point.

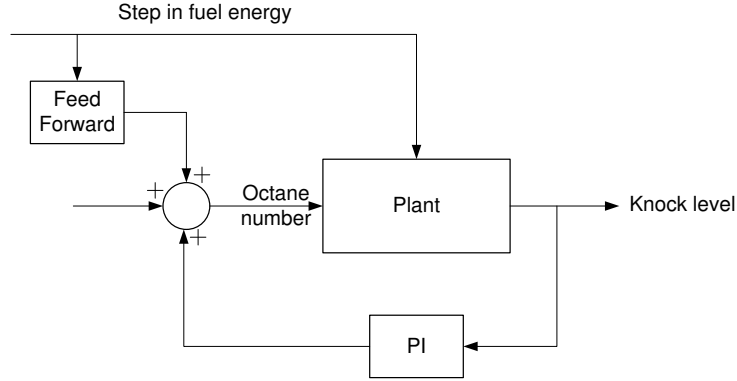


Figure 4.8: Block diagram of the FF and PI controllers

Feed-Forward control is shown in Figure 4.9. The step disturbance in fuel energy is initiated at cycle zero and it can be seen that the fuel octane is commanded to jump immediately by 8 PRF ON from 5.3 to 13.3 at the same time. The effect of adding this feed-forward is to immediately offset the step increase in fuel. The jump was chosen by manual tuning. Comparing Figure 4.7 and 4.9 shows that the fluctuations in knock are much lower than the no control case but are still higher in average and fluctuate after the fuel jump.

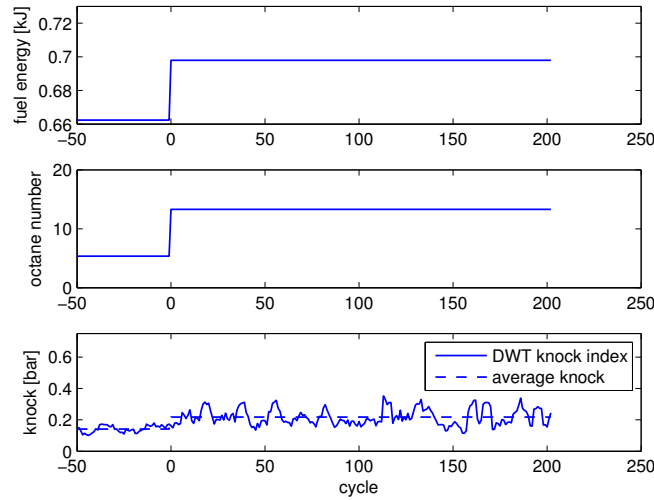


Figure 4.9: Knock level response to step in fuel energy - FF control

Figure 4.10 illustrates the resulting knock level with PI feedback control, with the dashed line indicating the desired knock level for the PI controller. The gains for the controller were tuned by first increasing the proportional gain until oscillations in the knock level could be seen. The proportional gain was then reduced and the integral gain was increased until the desired knock level response was achieved. The final gains for the proportional and integral gains are 1.1×10^{-4} and 2×10^{-5} respectively. From an average of 3.7, it takes approximately 25 cycles for the octane number to reach the new steady state value of 13.6.

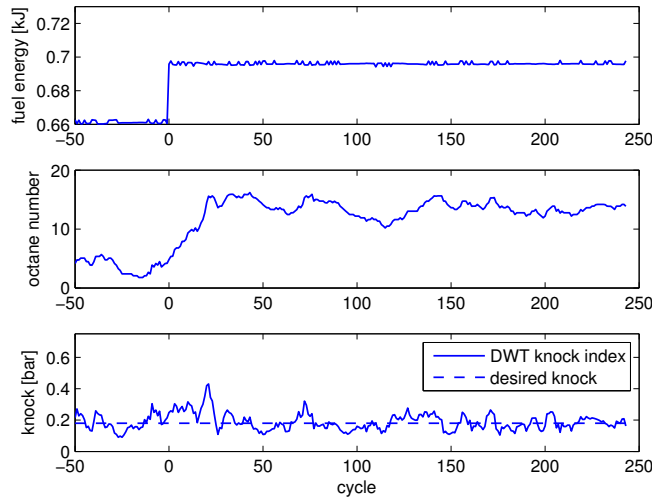


Figure 4.10: Knock level response to a step in fuel energy - PI control

In order to lower the 25 cycles that is needed to reach the new steady state ON, Feed-Forward is combined with PI control and the resulting knock response is shown in Figure 4.11. The octane command jumps immediately in Figure 4.11 due to the FF command and the resulting knock level appears to have less fluctuations when compared to Figure 4.10. From an average octane number of 4.4 the PI+FF control stabilizes to 15.0. Table 4.1 shows a comparison of knock level and standard deviation for the four cases. In the base case and in the Feed-Forward, the volatility of the knock value increase by at least 100 percent. With the PI controller, the standard deviation

increases by 11 percent, and the addition of Feed-Forward lowers that deviation to 6 percent.

The normalized deviation from the desired knock value is also tabulated in Table 4.1. The ratio of κ_2/κ_1 illustrates how the average knock value changed from the desired 0.18 bar set point. For both the baseline case as well as the Feed-Forward case, the knock level increases 80 percent and 50 percent respectively. By using PI controller (with or without Feed-Forward), the knock level is within 3 percent of the desired value. When the knock level in Figure 4.11 is compared to Figure 4.10, the addition of FF seems to reduce the knock fluctuation right after the step in fuel energy.

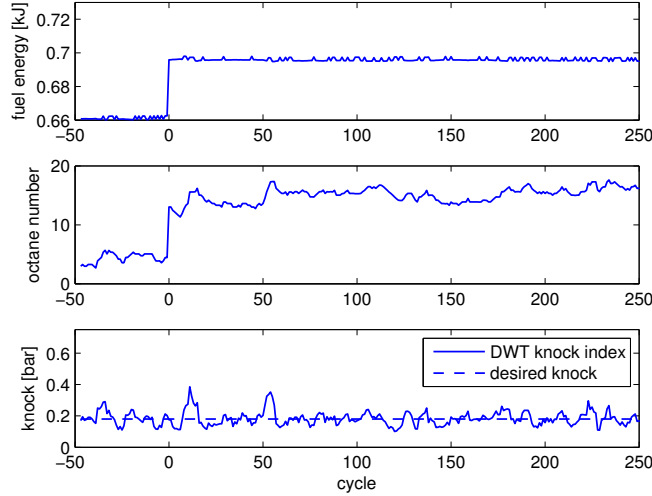


Figure 4.11: Knock level response to a step in fuel energy - PI+FF control

Table 4.1: Comparison of Control Schemes to No Control Case

	No Control	FF	PI	PI and FF
σ_2/σ_1	2.17	2.40	1.11	1.06
κ_2/κ_1	1.79	1.54	1.03	0.98

Since knock is a stochastic process [Naber et al., 2006] it is important to discuss the confidence levels of these values. The average and standard deviation before and

after the jump were determined in order to quantify how well the control worked. These tests were conducted three times for each controller. Table 4.2 shows the average and one standard deviation across three tests.

Table 4.2: Average and standard deviation of Control Schemes Across Three Tests

Control Method	Ratio	Average	standard deviation
PI	σ_2/σ_1	1.12	0.25
	κ_2/κ_1	1.12	0.09
PI and FF	σ_2/σ_1	1.02	0.06
	κ_2/κ_1	1.00	0.05
FF	σ_2/σ_1	1.70	0.64
	κ_2/κ_1	1.30	0.21

CHAPTER 5

EVVA – SI OPERATION

This chapter describes tests conducted with the EVVA system with the engine running in SI mode. Steady state valve timing of different IVC and EVO are conducted. The resulting effect on engine performance and emissions is reported. Cycle by Cycle changes in EVO are conducted to show robustness of the valve controller and are compared with the simulation developed by Chladny [2007] to validate the EVVA model. Cycle by cycle changes of IVC are conducted to demonstrate fast load changes in the engine. Lastly, thermal effects of running the EVVA system in SI are described.

5.1 Steady SI Operation for Several Valve Timing

The general SI engine operating conditions are given in Table 3.4. The valve timing for the different cases studied are tabulated in Table 5.1 and are labeled SI1 to SI4. The base case (SI1) is the valve timing used on engine start-up. Engine operating conditions are also listed in the table and the corresponding air/fuel ratio(λ) is measured. Emissions are recorded in ADAPT and the pressure trace is sampled at 50 kHz with the dSPACE 1103 controllers. The pressure trace is converted from time to crank angle and synchronized with the CAD pressure trace from National Instruments to allow timing, IMEP, and efficiency to be calculated based on CAD. The results for each operating point are given in Table 5.2. The uncertainty in the measured and

calculated values are given in the table and are described in Appendix A.

Table 5.1: Valve Timing for steady state cases in SI

Engine Conditions	Base Case SI1	EVO at 130° SI2	IVC at 160° SI3	IVC at 200° SI4
IVO [aTDC]	-300	-300	-300	-300
IVC [aTDC]	-180	-180	-160	-200
EVO [aTDC]	180	130	180	180
EVC [aTDC]	300	300	300	300
Speed [rpm]	776.4	776.7	776.7	775.3
Intake Pressure [kPa]	67.8	67.37	69.4	65.8
Intake Temperature [°C]	25.6	23.8	26.2	24.7
Octane Number [PRF]	100	100	100	100
Injected Fuel Energy [kJ]	1.032	1.032	1.032	1.032

Table 5.2: Emissions and engine conditions for steady state SI cases

	SI1	SI2	SI3	SI4	Uncertainty (\pm)
CO [%]	1.54	1.16	2.86	0.74	0.09
CO ₂ [%]	10.26	10.53	9.72	11.00	0.07
NOx [ppm]	619	870	294.9	1368	150
O ₂ [%]	3.88	3.77	3.32	3.52	0.23
uHC [ppm]	<i>Saturated</i>	<i>Saturated</i>	<i>Saturated</i>	<i>Saturated</i>	-
λ	1.00	0.99	0.94	1.03	0.01
\dot{m}_{air} [g/sec]	1.75	1.75	1.64	1.80	0.05
IMEP [bar]	3.72	3.42	3.40	3.38	0.06
η_{th} [%]	23.6	21.8	21.6	21.3	1
$T_{exhaust}$ [°C]	331	333	337	376	3
$ROPR_{max}$ [bar/CAD]	1.86	2.12	1.70	2.26	0.10

The CO formation is dependant on the air-fuel ratio [Heywood, 1988]. In the tests conducted, late IVC (case SI3) caused a near doubling in the percent CO produced, while early IVC (case SI4) lowers the CO compared to base case results. The change in air-fuel ratio for the SI3 case is due to the air charge being sent back into the intake manifold before the intake valve closes. The CO₂ level is dependant on the λ ratio as well. It can be seen the CO₂ drops with a rich air-fuel ratio in the SI3 case as expected.

The NOx emissions also show strong dependency on the air-fuel ratio [Heywood, 1988]. However, in the test cases recorded, the variation of the NOx measurements on different days of the same data show a variance of up to 150 ppm. Despite this, the general trend in the late IVC (SI3) case is such that the NOx is lower as expected with a rich mixture. As well, with a slightly lean mixture as in the case of SI4, the NOx emissions are expected to be highest. The O₂ is also dependant of the air-fuel ratio. For the SI3 case, the O₂ level average drops due to the richer mixture.

In the recorded data sets, the uHC is saturated, at 10000 ppm. This is most likely due to the fuel air mixture being compressed into the crevasses of the non-uniform piston. The flame is most likely quenched before the flame can propagate into the crevasses such as between the compression rings. This leads to unburned fuel in the exhaust and thus the high uHC measurements.

The air-fuel ratio, with fuel held constant in these tests, is strongly dependant of the air flow. Using the laminar air flow meter described in section 3.1 the measured mass flow rate of air does not change between SI1 and SI2, but does decrease in SI3 with late IVC. When the IVC is early (SI4) the airflow is measured higher, and is reflected in the air-fuel ratio. The rate of combustion as determined by the maximum rate of pressure rise (ROPOR) is given by

$$ROPOR_{max} = \left. \frac{dP_{cyl}}{d\theta} \right|_{max} \quad (5.1)$$

where $d\theta$ is a constant crank angle sample rate of 0.1 CAD and dP_{cyl} is the change in pressure per tenth of a CAD and is tabulated for the four cases in Table 5.2. It is an indication of knock in HCCI mode and will be compared to in the following chapter.

5.2 Cycle by Cycle Switch of EVO in SI

Switching the valve timing of EVO between two values on a cycle basis is conducted to test the EVVA valve motion controller to a cycle by cycle load disturbance. This test is similar to that conducted by [Chladny, 2007] on the test bench where the controller maintains soft landing of the valve using a chamber chamber that simulates exhaust pressure at it is switched between one and five bar each cycle. To create a similar test on the single cylinder engine, the EVO is moved between 100 degrees aTDC (SIC1) and 180 degrees aTDC (SIC2) in SI with the engine conditions for this test in Table 5.3 and other parameters listed in Table 3.4. No emissions were taken in the cycle by cycle switching since the emissions bench requires several cycles to stabilize.

Table 5.3: Engine Operating Conditions

Operating Condition	SIC1	SIC2
Engine speed [RPM]	777	777
Injected Fuel Energy [kJ]	0.680	0.680
IVC [bTDC]	180	180
IVO [bTDC]	300	300
EVC [aTDC]	300	300
EVO [aTDC]	100	180
IMEP [bar]	4.48 ± 0.07	4.85 ± 0.07
ROPR [bar/CAD]	1.07 ± 0.02	1.09 ± 0.05
θ_{Pmax} [CAD]	14.15 ± 0.15	15.3 ± 0.11

The exhaust back pressure at the start of valve opening is approximately 3.4 bar for SIC1 while the exhaust back pressure for SIC2 is approximately 1.5 bar as shown in the pressure trace and Pressure-Volume diagram in Figure 5.1 and 5.2, respectively. Thirty six consecutive cycles were recorded in which the EVO is switched every cycle between SIC1 and SIC2. The range of EVO back pressure tested in these experiments is less than that reported by [Chladny, 2007]. Lower exhaust valve pressure at bottom dead center could only be achieved by approaching the misfire limit. Higher exhaust back pressures at valve timing earlier than 100 degrees aTDC lead to issues with valve

reliability.

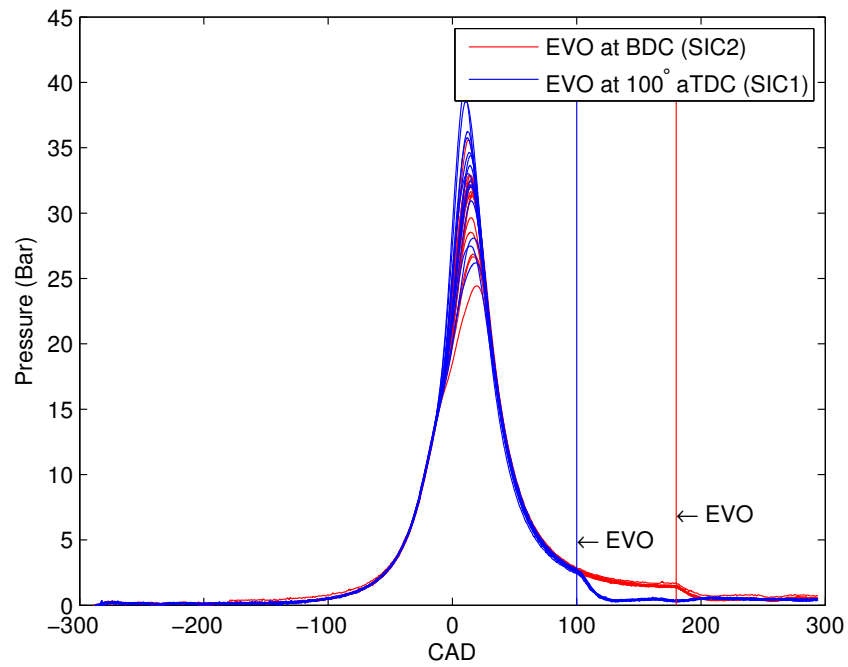


Figure 5.1: Cylinder pressure curve comparison for cyclic changes in EVO timing

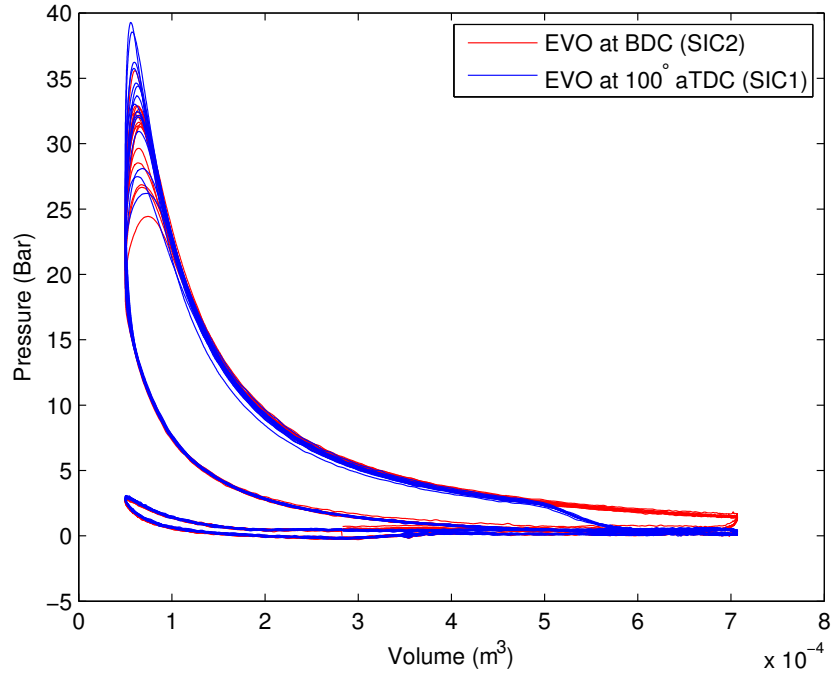


Figure 5.2: Cylinder pressure versus volume for cyclic changes in EVO timing

The EVO motion is shown in Figure 5.3 during the cycling. The plots for the position and current begin at the trigger for the exhaust valve opening event. It can be seen that against the higher back pressure, the valve motion takes longer and higher current is needed. Comparing to the results reported by [Chladny, 2007] in Figure 2.10, the position and current requirements show similar trends with current peaks that occur during the landing approach. The position-velocity plot in the bottom of Figure 5.3 shows the speed with respect to position for the full opening and closing of the exhaust valve. Comparing this figure to that of Figure 7.18 of [Chladny, 2007] shows the noise in both the position and velocity on the engine test bed. The difference due to changing EVO is apparent, however, in the velocity at -7 mm. As well, the valve bounce and the speed at which the bounce occurs can be seen at -8 mm for the EVO at 100 degrees aTDC.

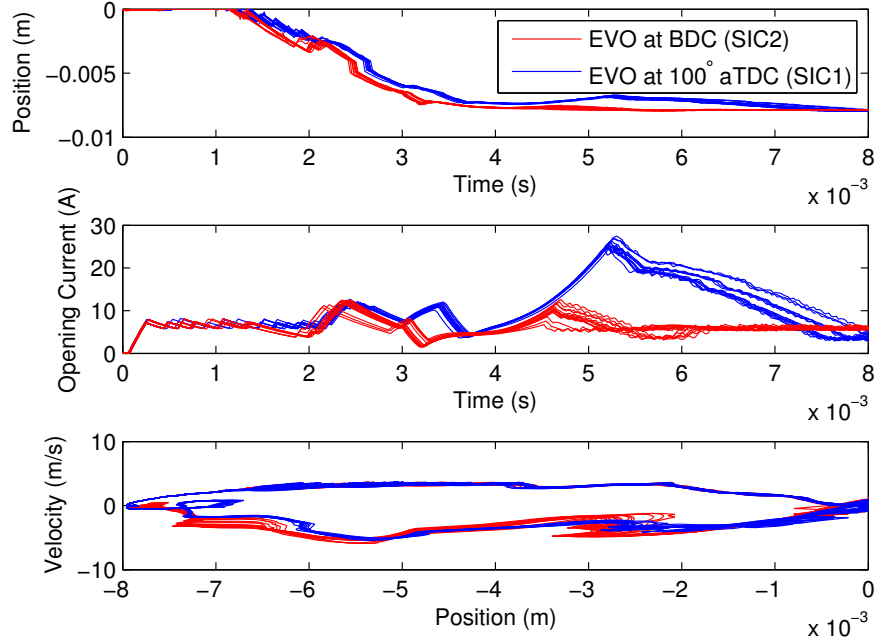


Figure 5.3: Valve performance for cycling changes in EVO timing

The power consumption per cycle is determined using the equation

$$Power = \frac{\sum_{k=1}^{k=M} PWM_k * 44.7 * i_k}{M} \quad (5.2)$$

where $PWM_k * 44.7$ is the converted voltage command from the PWM signal, i is the current, and k is the sample and M is the total number of samples. The EVO cases, the samples are taken from the start of the valve open event to the point that the valve controller switches to the holding routine. The resulting power consumption is 83.1 ± 2.0 Watts and 58.7 ± 0.8 Watts for SIC1 and SIC2 events, respectively.

5.3 Controller and Model Validation with SI Data

A physics based model and a flatness based controller of the valve actuator is detailed in [Chladny, 2007]. The valve motion control is designed using this simulation model

and using experimentally measured exhaust valve opening pressures at different loads. The control is ported to a dSPACE DS1103 controller for real time control. Then the valve motion control is tested on the valves on a test bench which simulates combustion pressures of an engine. In this work, a cylinder head is mounted on the single cylinder engine and the valve motion control is tested. The valve motion control, which was designed using a simulation model of the actuator and tested on the test bench worked without modification on the single cylinder engine. This not only means that the control algorithm works, but that the simulation model of the valve is a good representation of the non-linear dynamics of the valve and this simulation model can be used to further develop non-linear control algorithms in simulation. The simulation model, shown in Figure 2.8 has the measured engine cylinder pressure for SIC1 and SIC2 as an input and engine operating conditions the same as in section 5.2. Simulation model parameters of engine bore, compression ratio, temperature of the exhaust gases, valve lash and displacement volume are set to match the engine and are variables defined before the simulation is run. The effect of changing the valve lash changes the middle position of the valve when the coils are deactivated, thus changing the pre-load and force the springs apply to the armature. The measured actual single cylinder engine values of holding current and initial gas force estimate are used and the gas force model in simulation (a function of engine load) is removed and replaced with the measured gas force from the in cylinder pressure transducer. The simulation model for the exhaust valve opening is compared to the experimental results for SIC2 with an initial 1.5 bar exhaust pressure in Figure 5.4. Time zero is the valve opening event and the valve state is closed at 0.008 seconds.

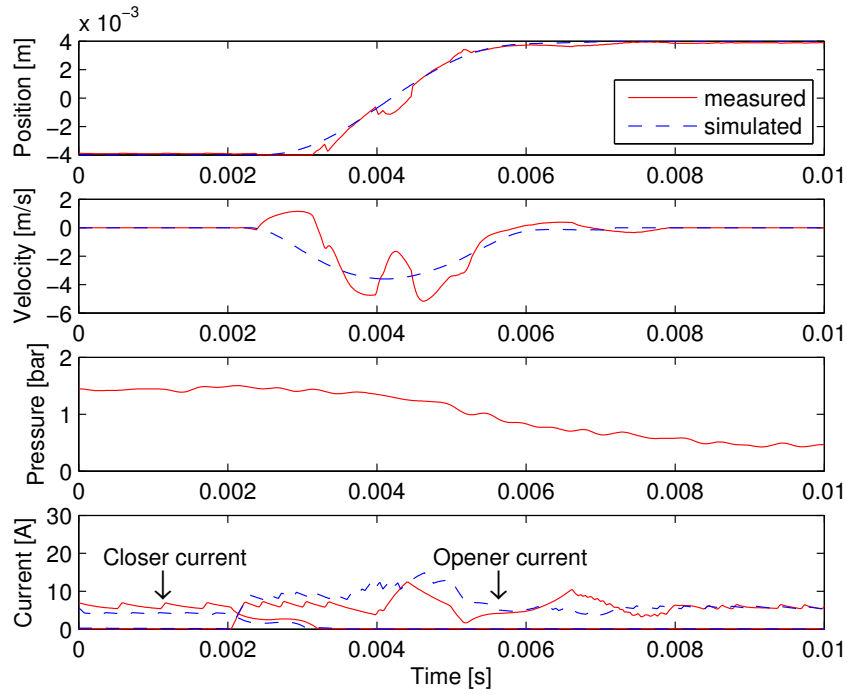


Figure 5.4: Simulation to engine experimental results for EVO at 180 degrees

In the top plot of Figure 5.4, the unfiltered measured position estimate is plotted against the simulation position as the valve opens. The measured position is estimated using the secondary measurement coils on the actuator so it contains more noise than the simulation (or the laser signal from the test bench) as shown in Figure 2.10 [Chladny, 2007]. The velocity estimate shown in the second plot of Figure 5.4 contains fluctuations that are not apparent in the simulation or test bench results due to the fluctuations in the position estimate. The position estimate from the coils has more fluctuations than the simulation but can actually be implemented on the engine. The measured cylinder pressure (third plot in Figure 5.4) is the disturbance to the simulation and is shown to illustrate the exhaust back pressure as well as the in cylinder pressure as the valve opens. The currents for both the opener and closer are also plotted in the bottom plot of Figure 5.4 and show the current response of the actuator coils to the pulse width modulated voltage input. The measured current

shows similar trends to the simulation in both figures. The simulation model captures the valve motion dynamics quite closely and deviations compared to the experimental position and current are attributed mostly to the noise in the position sensor.

Figure 5.5 compares the simulation results of SIC1 which corresponds to opening against an initial 3.4 bar exhaust pressure to experimental results. The measured position from the single cylinder engine shows similar noise which is then manifested in the velocity signal. The resulting currents, in both the opener and closer signal, show similar trends between simulation and experiment, but with more deviation, which is due to the position estimate fluctuation at 0.007 seconds.

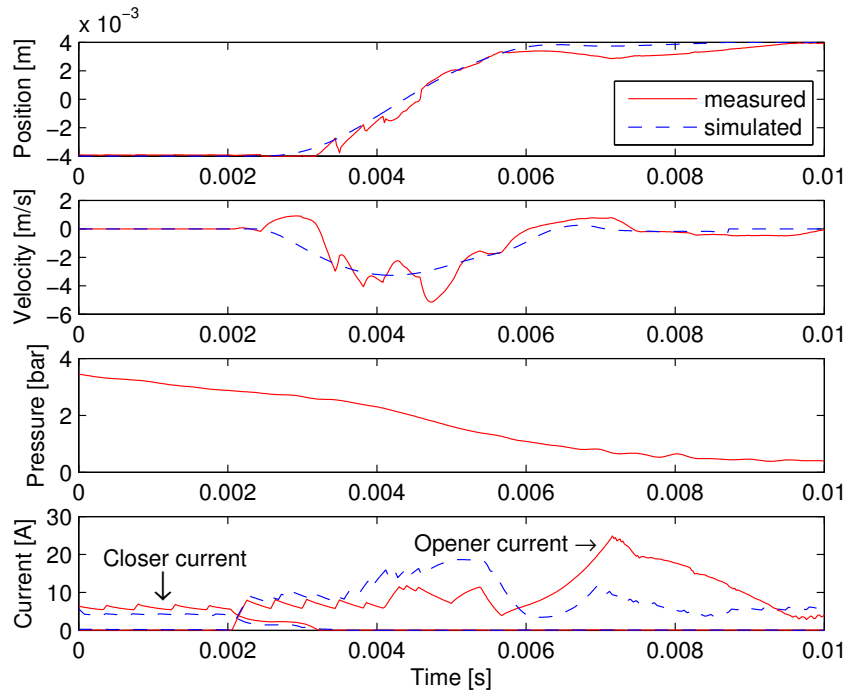


Figure 5.5: Simulation to engine experimental results for EVO at 100 degrees

The experimental curves in Figures 5.4 and 5.5 are two consecutive cycles in SI (cycles 9 and 10) from the section 5.2. The resulting simulation response to the two consecutive cycles with different loads is close to the experimental response indicating that the simulation model is a useful tool for control development. The single cylinder

engine results are compared to the simulation and test bench results as recorded by [Chladny, 2007]. Figure 2.10 shows the simulation and test bench comparison. The results of the test bench show less fluctuation in the position and velocity estimates and are closer to the simulation results than the single cylinder engine. The major differences in results can be attributed to the noise of the position estimate, likely due to the effect of the other nearby electronics and fluctuating pressures in a single cylinder engine.

5.4 Cycle by Cycle Switch of IVC in SI

Using EVVA it is possible to switch the engine load in one cycle by changing the IVC. The IVC timing effects the amount of air-fuel mixture taken into the cylinder. Late IVC causes cylinder charge to begin moving back into the cylinder as the piston moves upward. Early IVC closes the intake valve as the piston draws a fresh charge. In this section, the IVC timing is switched between 195 degrees bTDC (SIC3) and 160 degrees bTDC (SIC4) every cycle with engine operating conditions outlined in Table 5.4. The values of IVC were chosen to prevent misfire with the late IVC (SIC3) and to maximize the load on early IVC (SIC4). The pressure trace and the pressure-volume diagram is shown in Figure 5.6 clearly outlining the change in peak pressures resulting in varying the intake charge.

The use of IVC to regulate load, as indicated in the change in IMEP, shows the potential for throttle-less actuation. The change of IVC on the valve motion is shown in Figure 5.7. Time zero in the plots correspond to the close trigger event. The closing current as well as the valve position between the two cases overlap since the valve is subject to the same combustion chamber pressure in both cases. This indicates that for IVC changes where the pressure due to flow of air past valve does not increase, the change in valve timing of IVC, and thus the load, can be changed on a cycle by

Table 5.4: Engine parameters for IVC changes in SI

Parameters	Values
IVO [aTDC]	-300
EVO [aTDC]	180
EVC [aTDC]	300
IVC [aTDC]	-195 or -160
Engine speed [RPM]	827
Intake Temperature [°C]	27.4
Intake Pressure [kPa]	67.8
Injected Fuel Energy [kJ]	1.014
Octane Number [PRF]	100
Throttle [%]	0

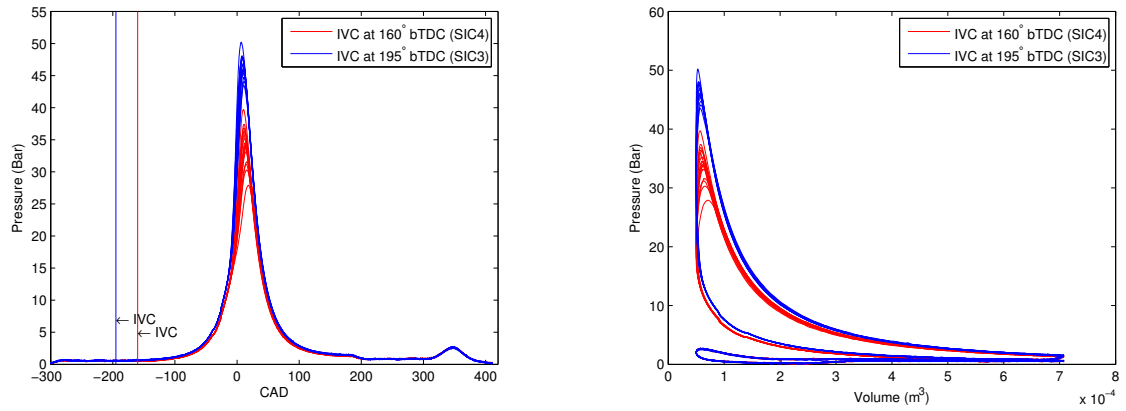


Figure 5.6: Pressure and Pressure-Volume diagram for cyclic changes in IVC

cycle basis without a change in valve actuator power requirement.

A return map plots successive values of a time series versus each other, giving an indication of the inherent deterministic structure of a data set [Green et al., 1999]. In Figure 5.8, the return map of θ_{Pmax} (for data shown in Figure 5.6) is plotted for the cycle by cycle change in IVC for 300 cycles.

Two regions can be seen in Figure 5.8 which correspond to each valve timing. This structured orientation of two regions indicate the dependance on valve timing and the absence of other deterministic components. A return map for 300 cycles of each operating point at steady state (valve timing constant) is shown in Figure 5.9.

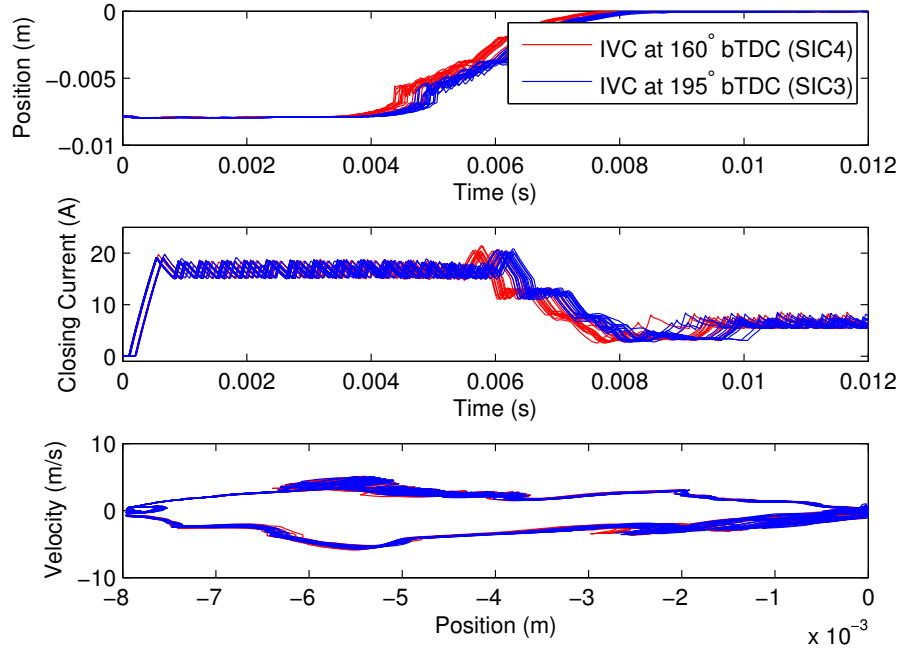


Figure 5.7: Intake valve position, current and position-velocity graph for cyclic changes in IVC

The difference for both cases of IVC valve timing results in the same SOC indicator θ_{Pmax} . The average timing, the range of θ_{Pmax} , and combustion metrics is tabulated in Table 5.5. The range of the ignition timing is taken as the maximum minus the minimum of θ_{Pmax} values.

Table 5.5: Performance indicators for IVC switching

Valve timing (bTDC)	θ_{Pmax} Range	θ_{Pmax} Average	IMEP Average	$ROPR_{max}$ Average
IVC at 195 During Cycling	5.8	8.2	4.43	2.5
IVC at 160 During Cycling	9.6	11.4	3.89	1.5
IVC at 195 Steady State	7.6	9.6	4.6	2.2
IVC at 160 Steady State	7.5	10.4	4.0	1.75

Comparing the values of Table 5.5 it can be seen that based on the the ignition timing range of SI, it can not be claimed that cycle by cycle switching of load increases the instability of θ_{Pmax} . As well, the average of θ_{Pmax} in each case indicates that

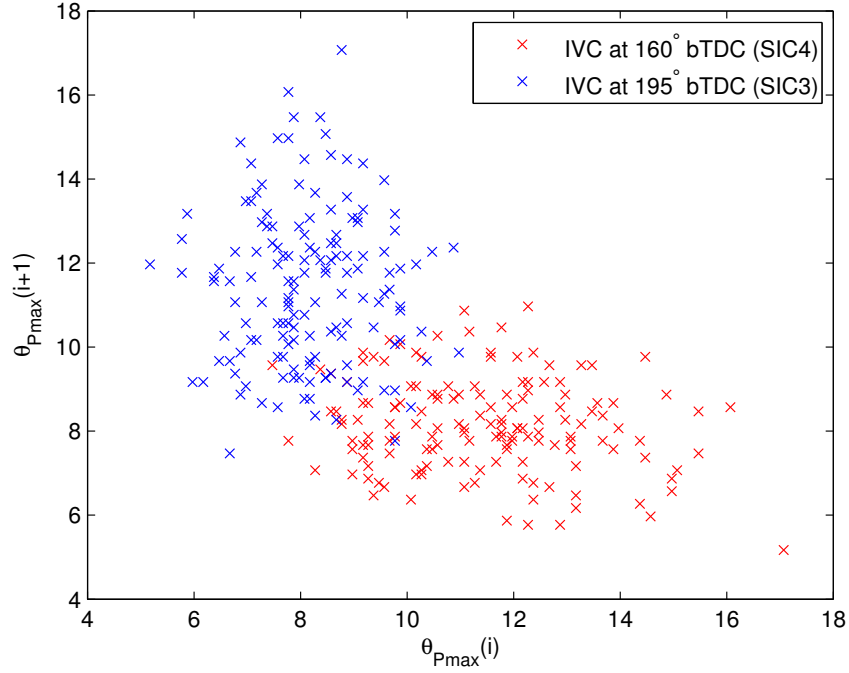


Figure 5.8: Return map for $\theta_{P_{max}}$ for 300 cycles of cyclic IVC. IVC varies from 160° bTDC to 195° bTDC every cycle

changes in the ignition timing of the current cycle is dependant on the cycle previous. The change in IMEP and $ROPR_{max}$ is evident and is different than the steady state case, showing the effect of the cycle previous on the power and pressure rise rate of the current cycle.

5.5 Heating Effects on EVVA System

The effect of temperature on the EVVA was studied by [Chladny, 2007] to assist in system identification of parameters such as effective moving mass, spring stiffness, viscous damping and spring pre-load. The valves were run in “cold” and “warm” conditions where cold conditions were where the valves were not run for 24 hours and the warm conditions were after 3000 repeated cycles. Since that test was performed on a test bench, real engine conditions of hot combustion gases, heated oil

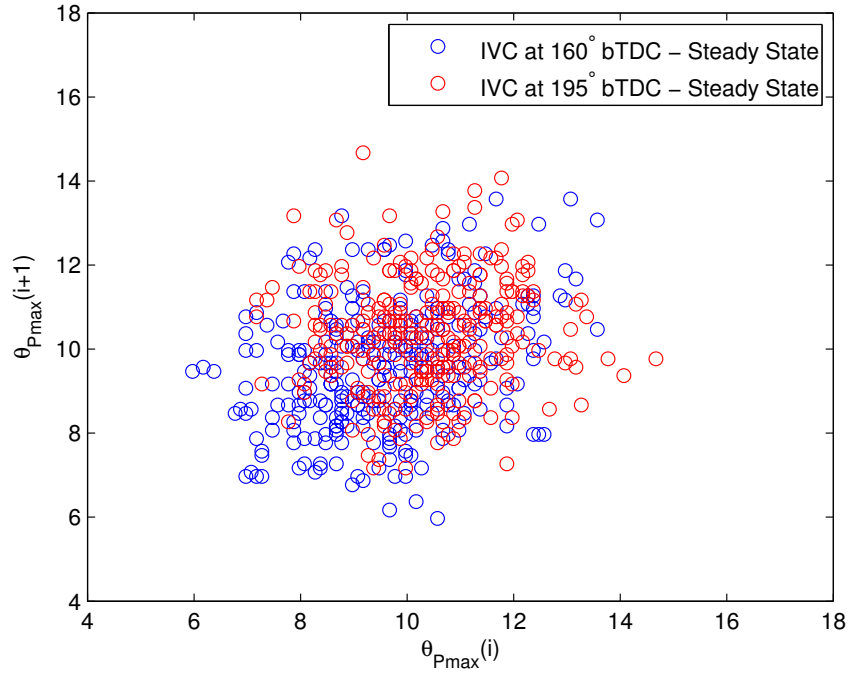


Figure 5.9: Return map for $\theta_{P_{max}}$ for 300 cycles of steady state valve timing in SI

and coolant fluids are not directly taken into account. The variation in valve response during warm up was also studied and compensated for using an adaptive controller [Tsai et al., 2011]. To examine the effects of temperature on the valves, the engine temperature is varied in SI mode.

First, the engine is started in cold conditions after a 24 hour period resulting in oil and coolant temperatures being at room temperature (20°C). The engine speed is held constant at 750 RPM and SI is started. As the exhaust valve warms up due to the hot exhaust gases, compression is lost. Since the EVVA valves do not have lash adjustment the valve experiences thermal expansion and this results in a loss of valve sealing. Once combustion becomes unstable and misfire cycles occur, spark and fuel are turned off and the pressure trace is recorded and is displayed in Figure 5.10. As the valve cools, cylinder pressure is recovered and the valve re-seals.

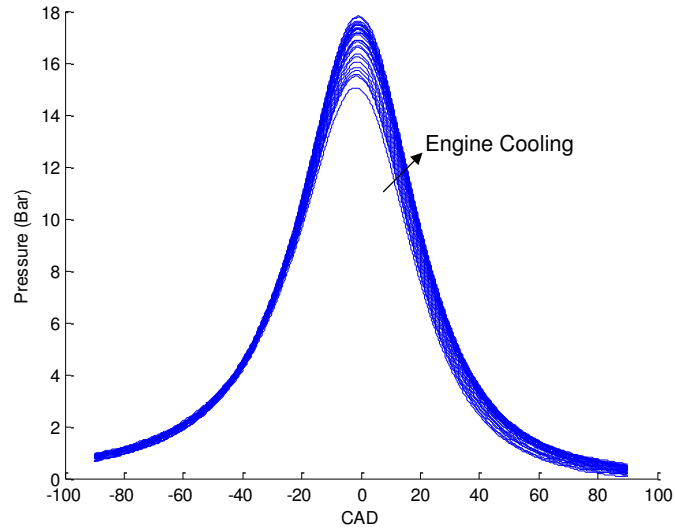


Figure 5.10: Motoring trace of every 10th cycle for 300 cycles showing the recovery of compression as the engine cools

Thus, engine operation in SI at 750 RPM is not sustainable due to misfire. As well, having hot exhaust gases run past the valve for extended time can cause engine/valve wear damage. Manual lash adjustment was performed by shimming the actuator by 0.004" to maintain a valve seal at operating temperature. This, however, means that when the engine is cold soft landing performance is degraded and wear increases. With this solution, the valve is slightly offset from the middle position which effects the valve initialization routine to swing the valve to the closed position.

A measurement of the valve response is conducted with 33 recorded cycles of warm conditions and 32 cycles of cold conditions during motoring with the shim added to the exhaust valve. The operating conditions of the two cases are listed in Table 5.6. The oil and coolant temperatures are regulated with a PID control loop. The data is recorded immediately after fuel and spark are shut off, so exhaust temperature is decreasing. In Table 5.6, the average exhaust temperature, recorded at 10Hz for 50 seconds during motoring is recorded. Figures 5.11 and 5.12 show the position, current and position-velocity plot for IVO and EVO in warm and cold conditions,

respectively.

Table 5.6: Engine Operating Conditions for Warm and Cold Motoring Conditions

Operating Condition	Cold Conditions	Warm Conditions
Engine speed [RPM]	777	777
Intake Temperature [°C]	24.1	23.5
Intake Pressure [kPa]	65.2	65.7
Oil temperature [°C]	22.8	55.3
Coolant temperature [°C]	20.2	51.8
$T_{exhaust}$ [°C]	36.9	126.3

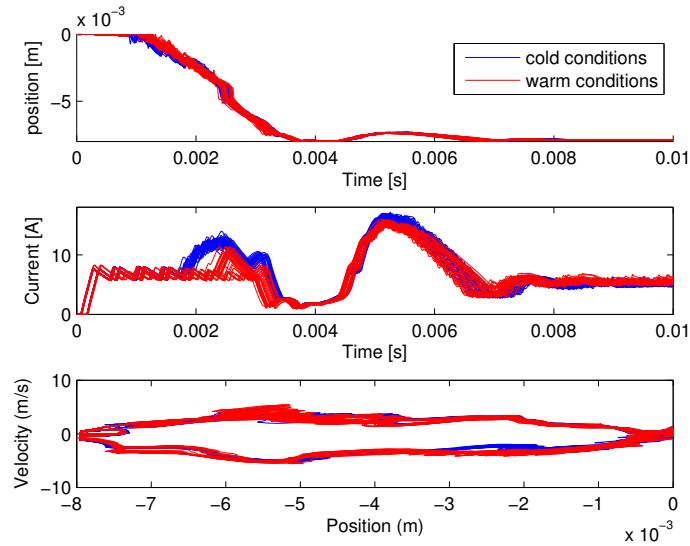


Figure 5.11: Intake valve opening (IVO) for cold and warm operating conditions

The position subplot for Figure 5.11 shows the same trajectory in both the warm and cold conditions. The coil current subplot shows a slight difference at 2 ms from the time of the open trigger where in the cold conditions a higher current is required. In contrast to the intake valve, the position subplot on the exhaust valve as shown in Figure 5.12 shows rapid spikes in the position signal at the 0.005 seconds and 0.007 seconds for warm conditions. These spikes are artifacts of the position observer which use the current and flux coil measurements. The current subplot, between the warm and cold conditions, shows differences of 15 A at the 0.005 seconds indicating

a significant change in controller response to the temperature conditions.

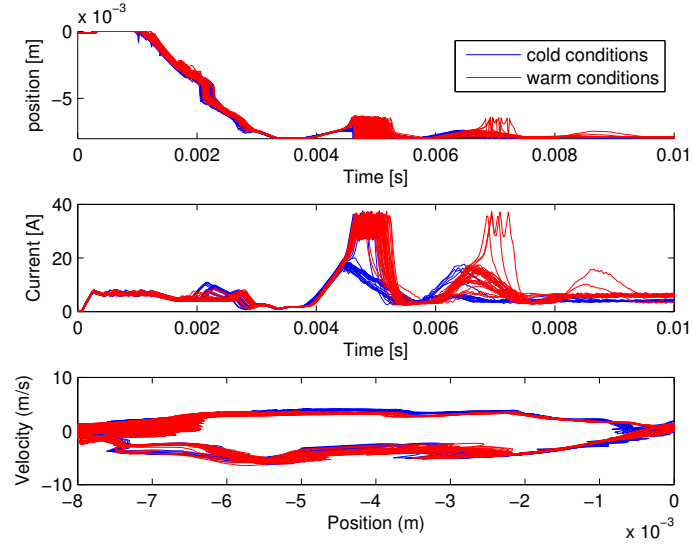


Figure 5.12: Exhaust valve opening (EVO) for cold and warm operating conditions

CHAPTER 6

EVVA – HCCI OPERATION

This chapter describes the tests conducted on the single cylinder engine with the EVVA head in HCCI combustion mode. Step changes in IVC and EVO valve timing are conducted and efficiency and emissions are compared to SI. Cyclic changes in IVC are conducted to show robustness of the EVVA system to load changes. Finally, the experimental results in HCCI are compared to simulation.

6.1 Steady HCCI Operation for Several Valve Timing

HCCI steady state engine operation and emissions with different valve timings are documented. The valve timing cases are listed in Table 6.1 and are labeled HCCI1 to HCCI4 with case HCC1 defined as the base case used in engine start-up. The timing of the valves are chosen to match section 5.1. The base engine operating conditions are also listed in Table 6.1.

The effect of valve timing cases on steady state HCCI operation is shown in Table 6.2. The emissions and exhaust temperature are recorded at 10 Hz for 50 seconds. The air-fuel ratio, is recorded for 200 cycles on a cycle basis while the rest of the parameters are calculated from the 0.1 CAD recorded pressure trace of 32 cycles.

The CO production, as mentioned in section 5.1, is dependant on air-fuel ratio. Due to the lean burning combustion of HCCI, the CO emissions recorded are low as

Table 6.1: Valve Timing for steady state cases in HCCI

Engine Conditions	Base Case HCCI1	EVO at 130° HCCI2	IVC at 160° HCCI3	IVC at 200° HCCI4
IVO [aTDC]	-300	-300	-300	-300
IVC [aTDC]	-180	-180	-160	-200
EVO [aTDC]	180	130	180	180
EVC [aTDC]	300	300	300	300
Speed [RPM]	730	775.5	776.0	776.7
Intake Pressure [kPa]	89.3	89.0	89.1	88.8
Intake Temperature [°C]	89.0	88.7	89.7	89.2
Octane Number [PRF]	10.0	10.3	10.2	10.3
Injected Fuel Energy [kJ]	0.442	0.442	0.442	0.442

Table 6.2: Emissions Summary for the Four Test Cases

	HCC1	HCC2	HCC3	HCC4	Uncertainty (\pm)
CO [%]	0.28	0.32	0.36	0.30	0.09
CO ₂ [%]	3.58	3.51	3.92	3.33	0.11
NOx [ppm]	0	0	0	0	150
O ₂ [%]	15.03	15.14	14.44	15.45	0.23
uHC [ppm]	2310	2837	3070	2386	22.5
λ [–]	2.76	2.73	2.43	2.79	0.03
\dot{m}_{air} [g/sec]	2.81	2.72	2.61	3.01	0.05
IMEP [bar]	2.17	2.03	2.08	2.14	0.06
η_{th} [%]	33.0	30.6	30.6	32.2	1
$T_{exhaust}$ [°C]	187	182	207	179	3
ROPR _{max} [bar/CAD]	2.82	2.53	2.22	2.86	0.06

expected. Comparing the four cases, the effect on CO production is less pronounced, with only a 0.08% difference in CO emissions; well within the uncertainty of the emissions recorded. Similar to SI, when IVC is set to 160 degrees bTDC (case HCCI3), λ decreases which corresponds to higher CO production. The CO₂ production is lower than SI. For low temperature combustion CO₂ emissions are dependant on equivalence ratio and the ratio of carbon to hydrogen as described in Table 4.3 of [Heywood, 1988]. For low temperature combustion of HCCI, NOx production for low engine speeds and torque is expected to be less than 10 ppm [Martinez-Frias et al., 2000]. Thus for this experiment, NOx is expected to be below the resolution of the NOx emissions bench.

The measurement uncertainty column in Table 6.2 is the 95% confidence interval of the calibration. Due to the lean burning combustion, the O_2 concentration for all four cases is much higher in HCCI than the SI cases of the previous chapter. For the HCCI cases, the oxygen content is lower in the case of the richer mixture HCCI3 than the leaner case HCCI4. The unburned hydrocarbon emission is similar to that reported by [Audet, 2008] for similar conditions. The uHC level corresponds with λ ; as the mixture becomes more rich, the level of unburned hydrocarbons increases. The airflow measurements follow that of section 5.1 where the late IVC shows less intake of air while the early IVC (HCCI4) shows more intake. Comparing $ROPR_{max}$ in Table 6.2 to Table 5.2 shows that HCCI has higher values due to the instantaneous homogeneous combustion.

6.2 Cycle by Cycle Switch of IVC in HCCI

To change the engine load cycle-by-cycle, IVC is switched back and forth from 180 degrees to 230 degrees bTDC on consecutive cycles while the valve timing for the other valve events are held constant. During this switching, 32 cycles are recorded and the results tabulated in Table 6.3. The valve timing events are chosen heuristically to be compatible with stable operation for both cycle by cycle operation as well as steady state operation at each IVC condition. The cylinder pressure as a function of crank angle is shown in Figure 6.1 and the change in valve timing is apparent from the difference in the pressure traces. The potential for cycle by cycle actuation for fast transients is thus apparent with this experimental setup.

For the cycle by cycle change in IVC, the position, current and velocity-position is shown in Figure 6.2. Due to only small changes in cylinder pressure for these two IVC timing (see Figure 6.1) the valve position, velocity and current shown in Figure 6.2 for both cases closely match. Larger changes in IVC for this operating point are

Table 6.3: Engine parameters for IVC changes in HCCI

Parameters	Values
IVO [aTDC]	-300
EVO [aTDC]	180
EVC [aTDC]	300
IVC [aTDC]	-180 or -230
Engine speed [RPM]	823
Intake Temperature [°C]	95.9
Intake Pressure [kPa]	88.0
Injected Fuel Energy [kJ]	0.4461
Octane Number [PRF]	11
Throttle [%]	50

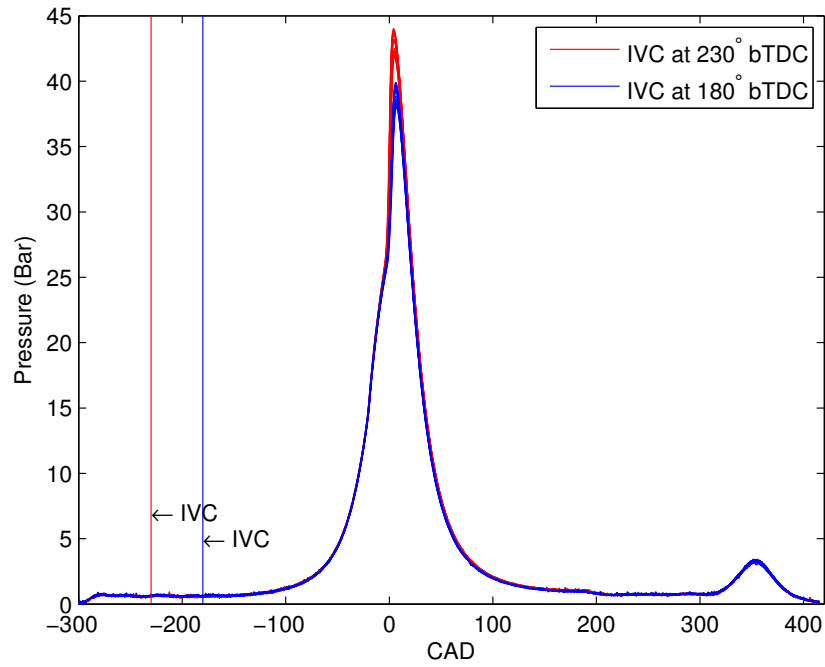


Figure 6.1: Pressure diagram for cyclic changes in IVC for HCCI operation

not possible due to unstable HCCI engine operation as the engine is near the misfire limit.

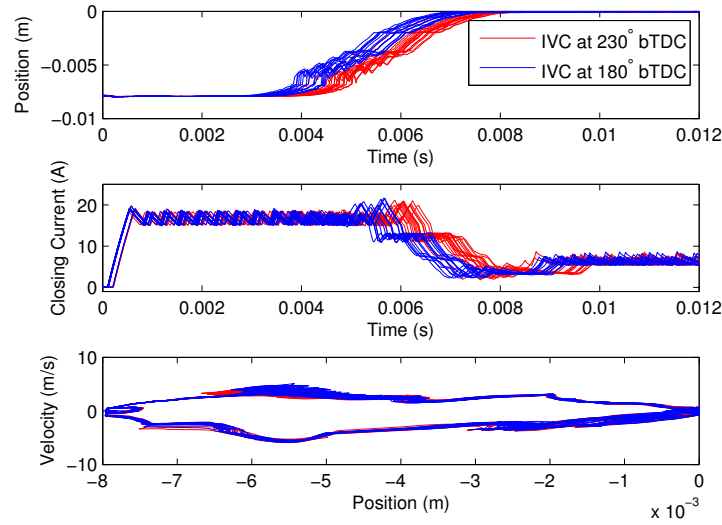


Figure 6.2: Intake valve position, current and position-velocity graph for cyclic changes in IVC

The return map for ignition timing for the previous switching case in HCCI mode (analogous to Figure 5.8 for SI) is shown in Figure 6.3. The return map shows 300 cycles where the average combustion timing, $\theta_{P_{max}}$, changes between 3.9 to 6.4 degrees aTDC. There are two distinct zones for each valve timing, and neither has a distinct pattern. We conclude from this that this case of cycle by cycle actuation does not create deterministic behavior in ignition timing that would indicate a multi-cycle combustion coupling.

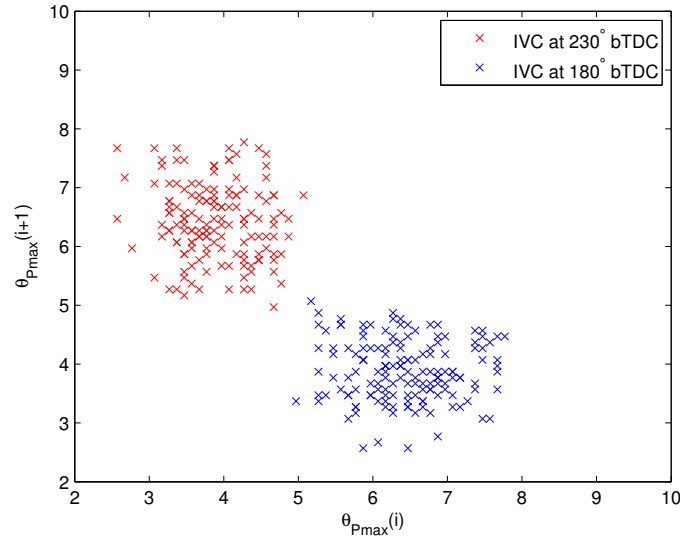


Figure 6.3: Return map for cyclic changes in IVC in HCCI

Each of the valve timings are now run individually at steady state for 300 cycles and the return map of $\theta_{P_{max}}$ for both cases is shown in Figure 6.4. The ignition timing shown in Figure 6.4 at steady state is different than that shown in Figure 6.3 of cycle by cycle actuation. During cycle by cycle actuation, $\theta_{P_{max}}$ occurs earlier for both valve timing cases compared to steady state. Since ignition timing is a complex function of the charge properties and heat transfer the ignition timing response requires a complex model. One such model details the sensitivity of ignition timing to changes in temperature, pressure, equivalence ratio, fuel octane number and exhaust gas recirculation [Shahbahkti, 2009]. In this case, changing IVC from 180° bTDC to 230° bTDC reduces the effective compression ratio and thus the charge pressure which is expected to retard the combustion timing. However, since there is less air but the fuel amount is constant, the equivalence ratio of the charge increases which is expected to advance the combustion timing. The competing effects result in the equivalence ratio influence being slightly stronger.

For the cycle by cycle and steady state HCCI cases the combustion timing average

and the average IMEP, and $ROPR_{max}$ are listed in Table 6.4. Also listed in Table 6.4 is the range of combustion timing, defined as the largest difference of $\theta_{P_{max}}$ for each valve timing case. The effect of cycle by cycle actuation compared to each individual steady state point is also apparent in the other combustion metrics such as IMEP and $ROPR_{max}$. During cycle by cycle actuation, the $ROPR_{max}$ and IMEP is higher for the case where IVC is 230° bTDC while the IMEP and $ROPR_{max}$ is lower when the IVC is 180° bTDC. The changes in combustion metrics are due to the previous cycle and the associated trapped residual which is known to affect HCCI combustion [Dec, 2002].

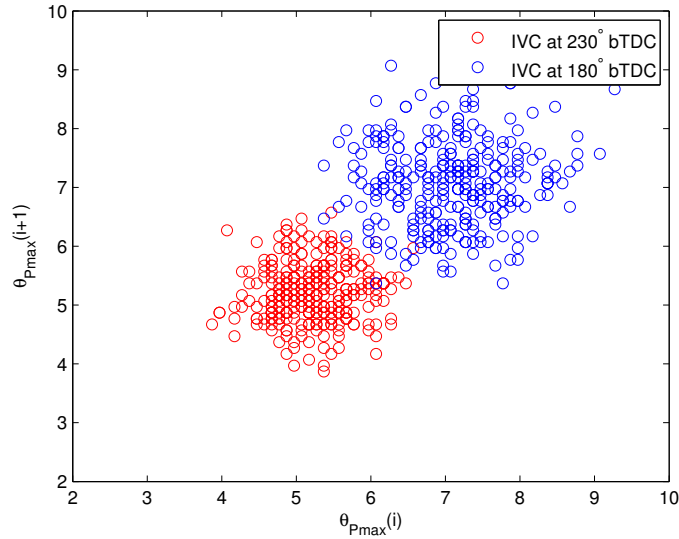


Figure 6.4: Return map for $\theta_{P_{max}}$ for 300 cycles of steady state valve timing in HCCI

Table 6.4: Performance indicators for IVC switching

Valve timing ($^\circ$ bTDC)	$\theta_{P_{max}}$ Range	$\theta_{P_{max}}$ Average	IMEP Average	$ROPR_{max}$ Average
IVC at 180 During Cycling	2.8	6.4	2.1	2.4
IVC at 230 During Cycling	2.5	3.9	2.4	4.7
IVC at 180 Steady State	3.9	7.07	2.2	2.4
IVC at 230 Steady State	2.7	5.2	2.2	3.3

Finally, comparing HCCI operation to SI in section 5.4, the operating points

show that the combustion timing of SI ($\theta_{P_{max}} = 8.2$ and 11.4) is much later than that of HCCI ($\theta_{P_{max}} = 3.9$ and 6.4) during cycle by cycle actuation. The steady state HCCI operating points have much less variation in $\theta_{P_{max}}$ than SI as expected, since HCCI is often considered stable combustion [Kalghatgi and Head., 2006] [Koopmans et al., 2002]. The range of $\theta_{P_{max}}$ was 3.9 and 2.7 for HCCI compared to 7.6 and 7.5 for SI. As well, upon cycle by cycle actuation, the ignition timing range does not increase compared to the steady state cases, indicating that fast actuation does not cause increased variation in combustion timing. The effect of cycle by cycle actuation is pronounced in the variation of the combustion metrics, both in SI and HCCI; the test confirms that HCCI ignition timing is a complex function of the charge properties.

6.3 Controller and Model Validation with HCCI Data

Experimental testing of the EVVA valve control to validate the EVVA model under HCCI combustion conditions is done using HCCI1 operating conditions. The EVVA simulation model is the same as that in SI Section 5.3 but the initial gas force estimate, the holding current and the gas force disturbance for this test are used. The resulting simulated valve position, velocity and gas force are compared to the experimental results in Figure 6.5. Good agreement between simulation and experiment provide further validation of the EVVA simulation model and the controlled valve motion also shows that the realtime valve motion control works well.

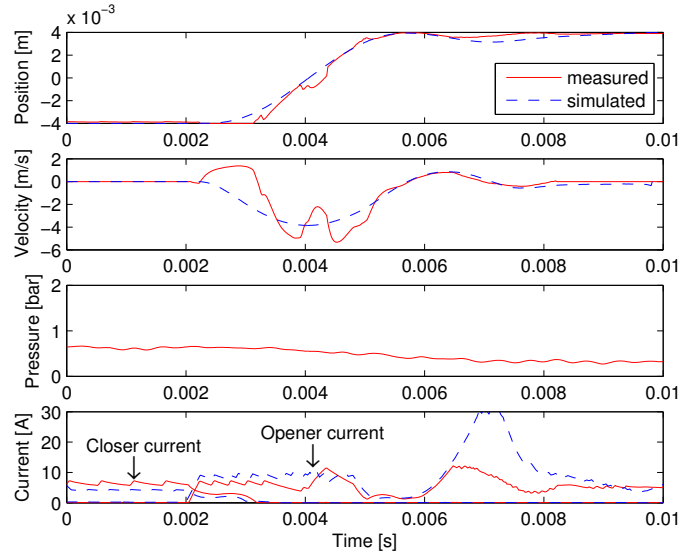


Figure 6.5: Simulation to engine experimental results for EVO at 180 degrees

In HCCI, with exhaust gas pressures less than 1 bar, the valve controller, both in simulation and experimentally, is able to control the valve opening to follow the desired trajectory. Similar noise is apparent in the position and thus the velocity signal due to the valve position measurement technique. The simulation model shows a deviation to experimental results at 0.007 seconds due to the valve drifting from the opener face. The valve model matches the position and velocity with the same exhaust gas disturbance indicating that the simulation model is a good tool for developing valve control algorithms.

6.4 Knock Mitigation Using EVVA

The EVVA system has been shown to control valve motion in HCCI combustion which opens up a wide variety of possible combustion control modes using fully flexible valve timing. For example, one use of the EVVA system is to control knock in HCCI by modifying the residual [Shi et al., 2005]. To demonstrate this, an operating condition close to engine knock is found and a step change in IVO and EVC valve timing, as

indicated in Table 6.5, changes the amount of in-cylinder residual to decrease which in turn changes the temperature for the next cycle. Table 6.5 also shows engine operating conditions for the high knock case and low knock case. The resulting change on a single unfiltered pressure trace is shown in Figure 6.6 where two cycles are the maximum knock levels recorded for low and high knock cases. The P-V diagram is shown in Figure 6.7 for the same two cycles.

Table 6.5: Valve Timing for Knock Mitigation

	High Knock Case	Low Knock Case
IVO [aTDC]	-300	-340
IVC [aTDC]	-180	-180
EVO [aTDC]	180	180
EVC [aTDC]	300	340
Speed [RPM]	775	776
Intake Pressure [kPa]	71.2	65.8
Intake Temperature [°C]	99.5	85.3
Exhaust Temperature [°C]	223.8	216.8
λ [-]	2.47	2.79
ON [PRF]	3	3
Injected Fuel Energy [kJ]	0.4042	0.4042
IMEP [bar]	2.0	2.0

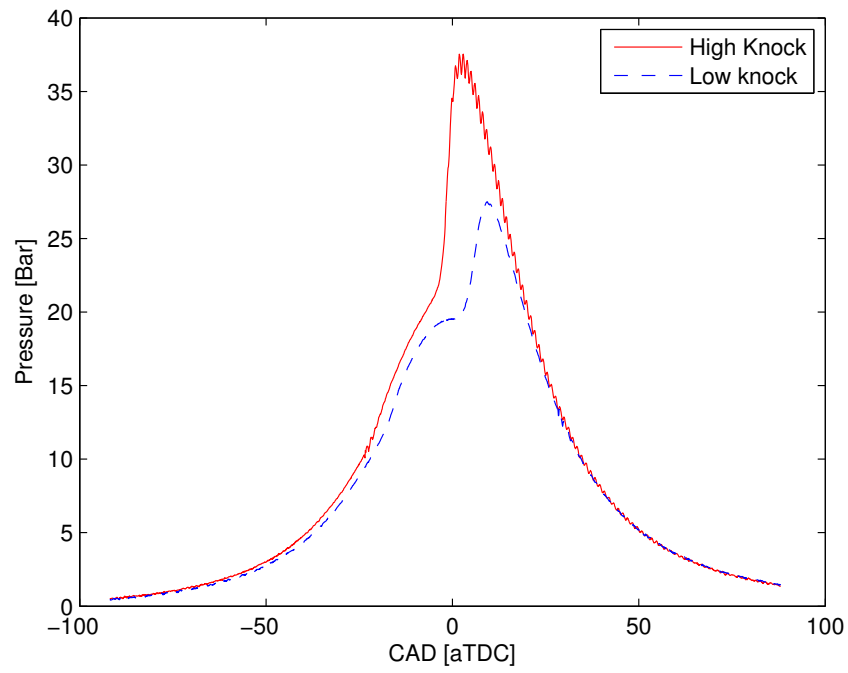


Figure 6.6: HCCI engine cycles showing effect of valve timing on knock

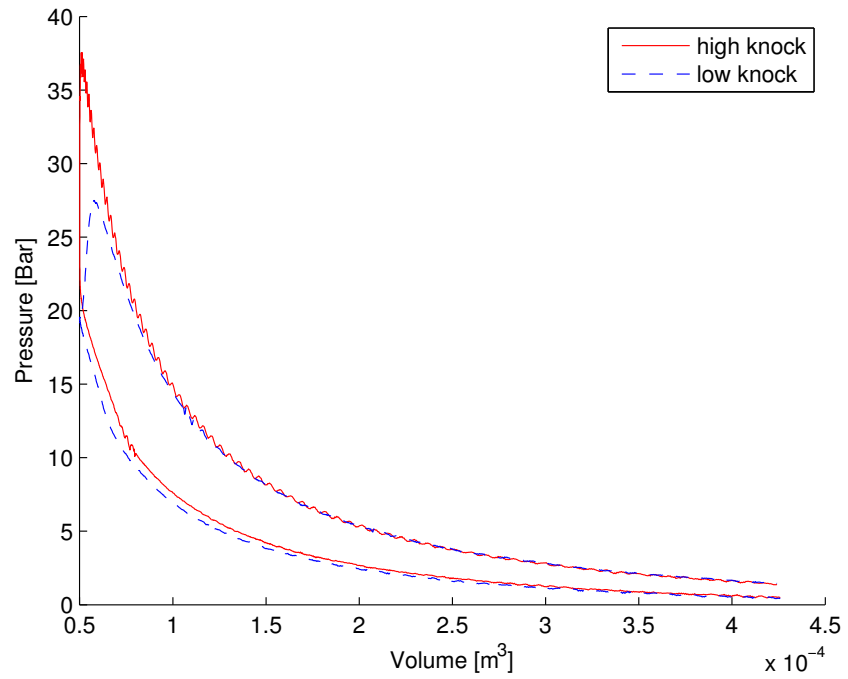


Figure 6.7: P-V diagram of HCCI engine cycles showing effect of valve timing on knock

In the high knock case for 250 cycles the average knock value based on the DWT method results in a knock index of $\kappa = 0.69 \pm 0.06$ bar. In the low knock case the average knock value is $\kappa = 0.22 \pm 0.06$ bar. This illustrates the potential of combining the VVA system with the DWT knock detection method. In the two methods, modifying the residual had little effect on the IMEP of the cycle. The IMEP of the two cases was found to be 2.0 ± 0.04 bar in both cases. The increase in peak pressure seen in the P-V diagram of Figure 6.7 for the high knock case seems to be offset by the lower pressure during the compression stroke. The two cycles plotted in Figure 6.6 have the highest coefficients from the real time DWT values. In plots that are similar to Figure 4.5 the third level decomposition is plotted in Figure 6.8. The knock frequency range is the same as in Chapter 4 since the cylinder bore has not changed between the two cylinder heads. This method is tested with a different cylinder head, piston shape (Figure 3.6), and pressure transducer location, yet is still able to detect the knock intensity with no changes to the algorithm.

The DWT method for high knock and low knock are compared to the P_{RMS} (similar to section 4.1.3) for all 250 engine cycles and the results as shown in Figure 6.9.

The DWT method shows more variance at the low knock case in Figure 6.9 due to noise in the pressure signal that is correlated with the DWT wavelet. An example of this is shown in Figure 6.10, which corresponds to cycle 118 of the low knock case (labeled in Figure 6.9). It can be seen that the oscillations in the pressure trace at 40 CAD gives rise to a spike in DWT coefficient. This noise, which was not present in chapter 4 is attributed to the EVVA electronics which is switching 42 V at 50 kHz in order to hold the valves closed.

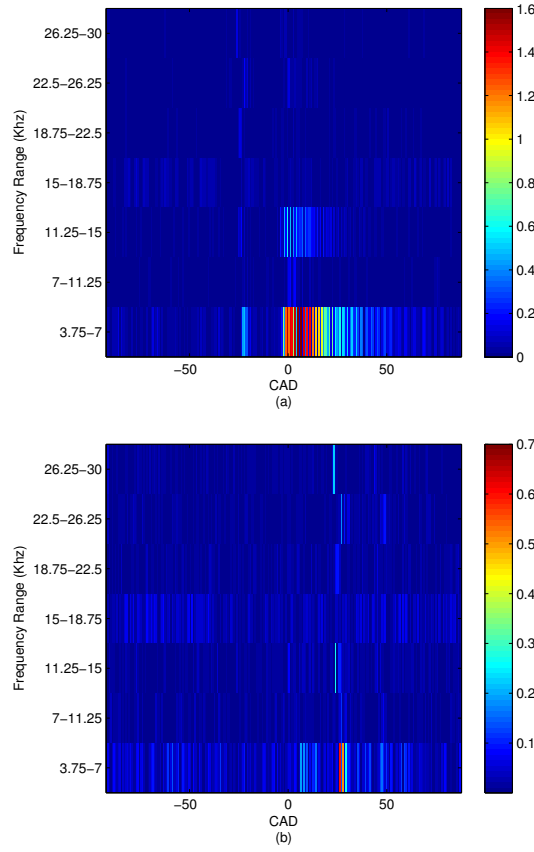


Figure 6.8: DWT colored coefficients for (a) high knock (b) low knock

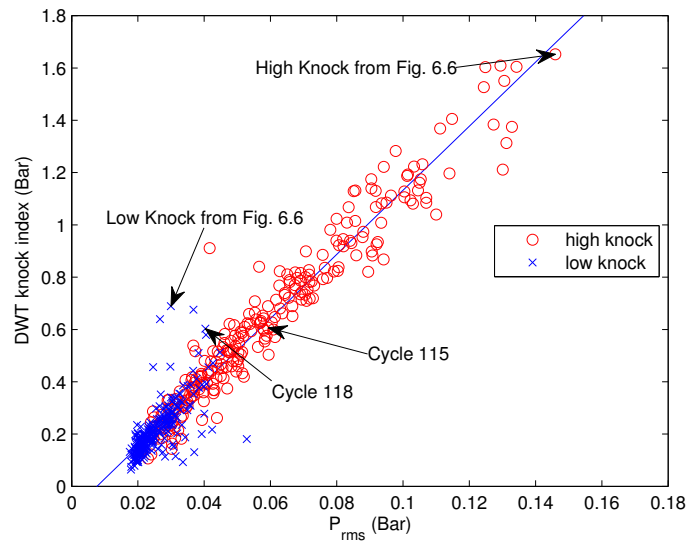


Figure 6.9: HCCI engine cycles showing effect of valve timing on knock

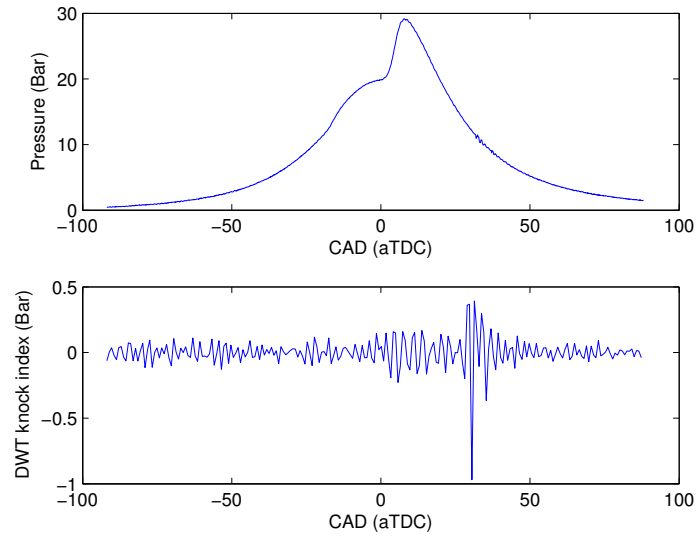


Figure 6.10: Oscillation in pressure trace and resulting spike in knock index

An example in the high knock case, where close correlation to the benchmark P_{RMS} is found is shown in Figure 6.11 and is labeled as cycle 114 in Figure 6.9. There are no oscillations in the pressure trace for this cycle and the corresponding DWT knock index over the recorded pressure trace shows no spikes, but an increase during combustion.

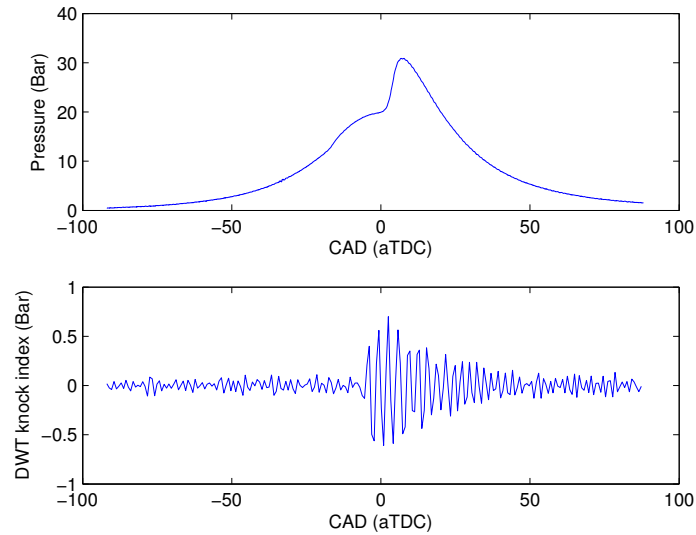


Figure 6.11: No oscillation in pressure trace and resulting knock index

CHAPTER 7

CONCLUSIONS

This chapter highlights important results of this thesis and its application to the automotive industry. Areas of future research focus are also outlined.

7.1 Conclusions

In this study a single cylinder experimental engine with two different cylinder heads is used to examine SI and HCCI combustion. Using the cam phaser head, the use of the Discrete Wavelet Transform to detect knock in HCCI is shown to be feasible in real time. Controlling the knock level with octane number in real time using classical PI control scheme is shown to be effective. The use of the EVVA to mitigate engine knock has also been demonstrated in HCCI by changing the IVO and the EVC by 40 degrees each in a single step. Fully variable electromagnetic valve timing has been implemented for study in SI and HCCI. The results of experimental trials with this setup show the robustness of the controller to changes in load, exhaust back pressure and changes in internal residual with the effects on emissions in changing valve timing. In SI, EVO jumps from 180 degrees to 100 degrees can be performed cycle by cycle. Cycle by cycle load changes in both SI and HCCI have been demonstrated with IVC changes of 35 degrees. The effects of temperature due to heat transfer to the exhaust valve from the combustion gases has been conducted and shows the increased valve

current requirements when warmed. A Simulink model of the valve train and controller developed by [Chladny, 2007] has been validated against experimental results. This validation means the model provides a realistic simulation test bed to develop future controllers which will work when ported to the engine.

7.2 Future Work

An extremely flexible single cylinder test bed has been commissioned with fully variable valve timing. This system can now be used to examine a variety of HCCI combustion challenges. These include using fully variable valve timing for

- Knock mitigation in HCCI
- Maintaining optimum combustion timing for a range of engine speeds, loads and for a variety of fuels
- Strategies for SI to HCCI mode switching

REFERENCES

- A&D Technologies (2001). *A&D Technologies BaseLine CAS Manual*.
- A&D Technologies (2003). *A&D Technologies ADAPT 4.6 User Manual*.
- Agrell, F., Angstrom, H. E., Eriksson, B., Wikande, J., and Linderyd, J. (2003). Integrated simulation and engine test of closed loop HCCI control by aid of variable valve timings. *SAE Paper No. 2003-01-0748*.
- Ashrafzadeh, A. R., Makki, A. M., and Servati, H. (1991). Quantitative analysis of knock sensor utilizing real-time discrete Fourier Transform (DTDFT). *SAE Paper No. 1991-25-0100*.
- Atkins, M. (2004). Experimental examination of the effects of fuel octane and diluent on HCCI combustion. Master’s thesis, University of Alberta.
- Atkins, M. J. and Koch, C. R. (2005). The effect of fuel octane and diluent on HCCI combustion. *Proc. IMechE, Part D*, 219:665 – 675.
- Audet, A. (2008). Closed loop control of HCCI using camshaft phasing and dual fuel. Master’s thesis, University of Alberta.
- Audet, A. and Koch, C. R. (2009). Actuator comparison for closed loop control of hcci combustion timing. In *SAE Paper 2009-01-1135*, page 8.
- Berntsson, A. W. and Denbratt, I. (2007). HCCI combustion using charge stratification for combustion control. *SAE Paper No. 2007-01-0210*.

- BMW Canada (2010). Valvetronic. <http://www.bmw.ca/ca/>. [Online; accessed April 20 2012].
- Boldea, I. and Nasar, S. (1999). Linear electric actuators and generators. *IEEE Transactions on Energy Conversion*, 14.
- Borg, J., Cheok, K., Saikalas, G., and Oho, S. (2005). Wavelet-based knock detection with fuzzy logic. *CIMSA. 2005 IEEE International Conference on Computational Intelligence for Measurement Systems and Applications, 2005*, pages 26 – 31.
- Borg, J. M., Saikalas, G., Oho, S., and Cheok, K. C. (2006). Knock signal analysis using the discrete wavelet transform. *SAE Paper No. 2006-01-0226*.
- Brustle, C. and Schwarzenthal, D. (2001). VarioCam Plus - A highlight of the Porsche 911 turbo engine. *SAE Paper No. 2001-01-0245*.
- Burda, C., Bailie, A., and Haines, G. (2010). *Driving Down Carbon: Reducing Greenhouse Gas Emissions from the Personal Transportation Sector in Ontario*. Pembina Institute for Appropriate Development.
- Canada, E. (2011). National inventory report 1990-2009: Greenhouse gas sources and sinks in Canada - executive summary. Technical report, Environment Canada.
- Carlarne, C. P. (2010). *Climate Change Law and Policy: EU and US approaches*. Oxford University Press.
- Chang, J., Kim, M., and Min, K. (2002). Detection of misfire and knock in spark ignition engines by wavelet transform of engine block vibration signals. *Measurement Science and Technology*, 13(7):1108–1114.
- Chang, W. S., Parlikar, T., Kassakian, J. G., and Keim, T. A. (2003). An electromechanical valve drive incorporating a nonlinear mechanical transformer. *SAE Paper No. 2003-01-0036*.

- Chladny, R. R. (2007). *Modeling and Control of Automotive Gas Exchange Valve Solenoid Actuators*. PhD thesis, University of Alberta.
- Chladny, R. R. and Koch, C. R. (2006). Magnetic flux-based position sensor for control of an electromechanical VVT actuator. In *2006 American Controls Conference (ACC), Minneapolis, MN, USA.*, page 3979 to 3984.
- Chladny, R. R. and Koch, C. R. (2008). Flatness-based tracking of an electromechanical VVT actuator with disturbance observer feed-forward compensation. *IEEE Transactions on Control Systems Technology*, 16:652–663.
- Chladny, R. R., Koch, C. R., and Lynch, A. F. (2005). Modeling of automotive gas-exchange solenoid valve actuators. *IEEE Transactions on Magnetics*, Volume 41, Issue 3:1155–1162.
- Chui, C. K. (1992). *An Introduction To Wavelets*. Academic Press.
- Chung, S. (2005). Flatness-based voltage end control of a gas exchange solenoid actuator for IC engines. Master’s thesis, Dept. Mechanical Engineering, University of Alberta.
- Chung, S. K., Koch, C. R., and Lynch, A. F. (2007). Flatness-based feedback control of an automotive solenoid valve control. *IEEE Transactions on Control System Technology*, 2:394 – 401.
- Dec, J. E. (2002). A computational study of the effects of low fuel loading and EGR on heat release rates and combustion limits in HCCI engines. *SAE Paper No. 2002-01-1309*.
- Dickey, D. W. (1999). Apparatus and method for reducing emissions in a dual combustion mode diesel engine.

- Draper, C. S. (1933). The physical effects of detonation in a closed cylindrical chamber. Technical Report 493, National Advisory Committee for Aeronautics.
- D.Schroll, Davis, C., Russ, S., and Barash, T. (1998). The volume acoustic modes of spark ignited internal combustion chambers. *SAE Paper No. 980893*.
- dSPACE (2005). *dSPACE MicroAutoBox Hardware Installation and Configuration*.
- dSPACE (2008). *DS1103 PPC Controller Board Release 6.3*.
- Duerr, K. and Seethaler, R. (2008). Time optimal cam synthesis for spring driven cams. In *Proceedings of the ASME 2008 International Design Engineering Technical Conferences & Computers and Information in Engineering Conference*. ASME.
- Ebrahimi, K., Shahbakhti, M., and Koch, C. R. (2011). Comparison of butanol/n-heptane as a blended fuel in an hcci engines. In *Combustion Institute/Canadian Section (CI/CS) Spring Technical Meeting*, page 6.
- Erickson, F. L. and Richeson, W. E. (1992). Spring driven hydraulic actuator.
- Frederic, A., Picron, V., Hobraiche, J., Gelez, N., and Gouiran, S. (2010). Electro-magnetic valve actuation system e-valve: Convergence point between requirements of fuel economy and cost reduction. *SAE Paper No. 2010-01-1197*.
- Geradin, R. C., Huallpa, B. N., Alves, M. F., and Arruda, J. R. F. (2009). Analysis of spark ignition engine knock signals using Fourier and discrete wavelet transform. *SAE Paper No. 2009-36-0312*.
- Ghazimirsaiied, A. (2012). *Extending HCCI Low Load Operation Using Chaos Prediction and Feedback Control*. PhD thesis, University of Alberta.

- Ghazimirsaid, A. and Koch, C. R. (2012). Controlling cyclic combustion timing variations using a symbol-statistics predictive approach in an hcci engine. *Applied Energy*, 92(0):133 – 146.
- Gillella, P. and Sun, Z. (2009). Modeling and control design of a camless valve actuation system. *American Control Conference*, pages 2696 – 2701.
- Gillella, P. and Sun, Z. (2011). Design, modeling, and control of a camless valve actuation system with internal feedback. *IEEE/ASME Transactions on Mechatronics*, 16:527–539.
- Green, J., Daw, C., Armfield, J., and Finney, C. (1999). Time irreversibility and comparison of cyclic-variability models. *SAE paper no. 1999-01-0221*.
- Handford, D. (2009). Direct injection assisted HCCI combustion of natural gas. Master’s thesis, University of Alberta.
- Heiko, G., Carsten, G., Christian, J., Heiko, N., and Leopold, M. (2000). Piezoelectric-hydraulic operating device for gas exchange valves of IC engines has to operate gas exchange valve, non-hermetised hydraulic transmission system constantly connected to oil pressure circuit of IC engine.
- Heywood, J. B. (1988). *Internal Combustion Engine Fundamentals*. McGraw-Hill Inc.
- Hosaka, T. (1991). Development of the variable valve timing and lift (VTEC) engine for the Honda NSX. *SAE Paper No. 910008*.
- Iverson, R. J., Herold, R. E., Augusta, R., Foster, D. E., Ghandhi, J. B., Eng, J. A., and Najt, P. M. (2005). The effects of intake charge preheating in a gasoline-fueled HCCI engine. *SAE Paper No. 2005-01-3742*.

- Jalili, N., Wagner, J., and Dadfarnia, M. (2003). A piezoelectric driven ratchet actuator mechanism with application to automotive engine valves. *Mechatronics*, 13:933.
- Johnson, R. W., Evans, J. L., Jacobsen, P., Thompson, J. R. R., and Christopher, M. (2004). The changing automotive environment: High-temperature electronics. *IEEE Transactions on Electronics Packaging Manufacturing*, 27 No. 3:164–176.
- Jones, J. C. P., Frey, J., Muske, K. R., and Scholl, D. J. (2010). A cumulative-summation-based stochastic knock controller. *Proceedings of the Institution of Mechanical Engineers Part D-Journal of Automobile Engineering*, 224(D7):969–983.
- Kaiser, E. W., Yang, J., Culp, T., Xu, N., and Maricq, M. M. (2002). Homogeneous charge compression ignition engine out emissions does flame propagation occur in homogeneous charge compression ignition? *International Journal of Engine Research*, 3:185–195.
- Kalghatgi, G. T. (2007). Fuel effects in CAI gasoline engines. In Zhao, H., editor, *Homogeneous Charge Compression Ignition (HCCI) and Controlled Auto Ignition (CAI) Engines for the Automotive Industry*, chapter 9. Woodhead Publishing Limited, Brunel University UK.
- Kalghatgi, G. T. and Head., R. A. (2006). Combustion limits and efficiency in a homogeneous charge compression ignition engine. *Int. Journal of Engine Research*, 7:215–236.
- Kim, C., Han, S., and Moon, S. (2000). The effect of engine misfire on catalytic converter and vehicle emissions. *SAE Paper No. 2000-05-0325*.
- Koopmans, L., Backlund, O., and Denbratt, I. (2002). Cycle to cycle variations:

- Their influence on cycle resolved gas temperature and unburned hydrocarbons from a camless gasoline compression ignition engine. *SAE Paper No. 2002-01-0110*.
- Kulzer, A., Hathout, J., and Sauer, C. (2007a). Multi-mode combustion strategies with CAI for a GDI engine. *SAE Paper No. 2007-01-0214*.
- Kulzer, A., Hathout, J. P., Sauer, C., Karrelmeyer, R., Fischer, W., and Christ, A. (2007b). Multi-mode combustion strategies with CAI for a GDI engine. *SAE Paper No. 2007-01-0214*.
- Kulzer, A., Nier, T., and Karrelmeyer, R. (2011). A thermodynamic study on boosted HCCI: Experimental results. *SAE Paper No. 2011-01-0905*.
- Lakshmanan, T. and Nagarajan, G. (2010). Experimental investigation on dual fuel operation of acetylene in a DI diesel engine. *Fuel Processing Technology*, 91:496–503.
- Lang, O., Salber, W., Hahn, J., Pischinger, S., Hortman, K., and Bucker, C. (2005). Thermodynamical and mechanical approach towards a variable valve train for the controlled auto ignition combustion process. *SAE Paper No. 2005-01-0762*.
- Lequesne, B. (1992). Permanent magnet linear motors for short strokes. *IEEE*, 1:162–170.
- Lin, J. and Qu, L. (2000). Feature extraction based on morlet wavelet and its application for mechanical fault diagnosis. *Journal of Sound and Vibration*, Volume 234 Issue 1:135–148.
- Lou, Z. (2007). Camless variable valve actuation designs with two-spring pendulum and electrohydraulic latching. *SAE Paper No. 2007-01-1295*.

- Lu, X., Han, D., and Huang, Z. (2011). Fuel design and management for the control of advanced compression-ignition combustion modes. *Progress in Energy and Combustion Science (in press)*.
- Lupul, R. A. W. (2008). Steady state and transient characterization of a HCCI engine with varying octane fuel. Master's thesis, University of Alberta.
- Mahrous, A., Potrzebowski, A., Wyszynski, M., Xu, H., Tsolakis, A., and Luszcz, P. (2009). A modeling study into the effects of variable valve timing on the gas exchange process and performance of a 4-valve DI homogeneous charge compression ignition (HCCI) engine. *Energy Conversion and Management*, 50:393–398.
- Mamalis, S., Nair, V., Andruskiewicz, P., Assanis, D., Babajimopoulos, A., Wermuth, N., and Najt, P. (2010). Comparison of different boosting strategies for homogeneous charge compression ignition engines - a modeling study. *SAE Paper No. 2010-01-0571*.
- Martinez-Frias, J., Aceves, S., Flowers, D., Smith, J., and Dibble, R. (2000). HCCI engine control by thermal management. *Society of Automotive Engineers International Fall Fuels and Lubricants Meeting and Exposition*.
- Mashkournia, M., Audet, A., and Koch, C. (2011). Knock detection and control in an HCCI engine using DWT. In *Proceedings of the ASME 2011 Internal Combustion Engine Division Fall Technical Conference*.
- Moffat, R. J. (1988). Describing the uncertainties in experimental results. *Experimental Thermal and Fluid Science*, 1:3–17.
- Naber, J. D., Blough, J. R., Frankowski, D., Goble, M., and Szpytman, J. E. (2006). Analysis of combustion knock metrics in spark-ignition engines. *SAE Paper No. 2006-01-0400*.

- Nagaya, K., Kobayashi, H., and Koike, K. (2006). Valve timing and valve lift control mechanism for engines. *Mechatronics*, 16:121–129.
- Nagaya, K., Kobayashi, K., Neno, M., Hosokawa, Y., and Murakami, I. (2008). Low driving energy engine valve mechanism using permanent-electromagnet and conical spring. *International Journal of Applied Electromagnetics and Mechanics*, 28:267–273.
- Najt, P. M. and Foster, D. E. (1983). Compression-ignited homogeneous charge combustion. *SAE Paper No. 830264*.
- National Instruments (2009). *National Instruments User Manual*.
- Nilsson, Y., Frisk, E., and Nielsen, L. (2009). Weak knock characterization and detection for knock control. *Proceedings of the Institution of Mechanical Engineers Part D-Journal of Automobile Engineering*, 223(D1):107–129.
- Olsson, J. O., Tunestål, P., Ulfvik, J., and Johansson, B. (2003). The effect of cooled EGR on emissions and performance of a turbocharged HCCI engine. *SAE Paper No. 2003-01-0743*.
- Payne, D. W. (1899). Electrically-controlled valve-gear for gas or other motors.
- Persson, H., Agrell, M., Olsson, J.-O., Johansson, B., and Ström, H. (2004). The effect of intake temperature on HCCI operation using negative valve overlap. *SAE Paper No. 2004-01-0944*.
- Peterson, K. S. (2005). *Control Methodologies for Fast & Low Impact Electromagnetic Actuators for Engine Valves*. PhD thesis, University of Michigan.
- Picron, V., Postel, Y., and Nicot, E. (2008). Electro-magnetic valve actuation system: First steps toward mass production. *SAE Paper No. 2008-01-1360*.

- Pierick, R. J. and Burkhard, J. F. (2000). Design and development of a mechanical variable valve actuation system. *SAE 200 World Congress*.
- Pischinger, F. and Kreuter, P. (1984). Electromagnetically operating actuator.
- Pischinger, M., Salber, W., van der Staay, F., Baumgarten, H., and Kemper, H. (2000). Benefits of the electromechanical valve train in vehicle operation. *SAE paper no. 2000-01-1223*.
- Sabri, A. M. (1998). *Regenerative Hydraulic Variable Valve Actuator for internal combustion engines*. PhD thesis, University of Wisconsin-Madison.
- Santoso, H., Matthews, J., and Cheng, W. K. (2005). Managing SI/HCCI dual-mode engine operation. *SAE paper no. 2005-01-0162*.
- Schechter, M. M., Hills, F., Levin, M. B., and Bloomfield (1994). Variable engine valve control system with hydraulic damper.
- Seethaler, R. and Duerr, K. (2009). Electromagnetic valve actuation system with two configurations. In *Proceedings of the ASME 2009 International Design Engineering Technical Conferences & Computers and Information in Engineering Conference*. ASME.
- Sellnau, M. and Rask, E. (2003). Two-step variable valve actuation for fuel economy, emissions, and performance. *SAE paper no. 2003-01-0029*.
- Shahbahkti, M. (2009). *Modeling and Experimental Study of an HCCI Engine for Combustion Timing Control*. PhD thesis, University of Alberta.
- Shahbakhti, M. and Koch, C. R. (2010). Physics based control oriented model for hcci combustion timing. *Journal of Dynamic Systems, Measurement, and Control*, 132(2):021010.

- Sheppard, C. G. W., Tolegano, S., and Woolley, R. (2002). On the nature of autoignition leading to knock in hcci engines. *SAE Paper No. 2002-01-2831*.
- Shi, L., Cui, Y., Deng, K., Peng, H., and Chen, Y. (2005). Study of low emission homogeneous charge compression ignition (HCCI) engine using combined internal and external exhaust gas recirculation (EGR). *Energy*, 31:2329–2340.
- Sjöberg, M. and Dec, J. E. (2007). EGR and intake boost for managing HCCI low-temperature heat release over wide ranges of engine speed. *SAE Paper No. 2007-01-0051*.
- Souder, J., Mack, J., Hendrick, J., and Dibble, R. (2004). Microphones and knock sensors for feedback control of HCCI engines. *ASME Internal Combustion Engine Division*.
- Stolk, T. and Gaisberg, A. (2001). Elektromagnetischer aktuator.
- Sun, Z. and Cleary, D. (2003). Dynamics and control of an electro-hydraulic fully flexible valve actuation system. *American Control Conference*, Vol. 4:pages 3119–3124.
- Tsai, J., Koch, C. R., and Saif, M. (2011). Cycle adaptive feedforward approach controllers for an electromagnetic valve actuator. , *IEEE Transactions on Control Systems Technology*, PP(99):1 –9.
- Tsurushima, T., Kunishima, E., Asaumi, Y., Aoyagi, Y., and Enomoto, Y. (2002). The effect of knock on heat loss in homogeneous charge compression ignition engines. *SAE Paper No. 2002-01-0108*.
- Verhelst, S., Demuyne, J., Sierens, R., and Huyskens, P. (2010). Impact of variable valve timing on power, emissions and backfire of a bi-fuel hydrogen/gasoline engine. *International Journal of Hydrogen Energy*, 35:4399–4408.

- Visakhamoorthy, S., Wen, J. Z., Sivoththaman, S., and Koch, C. R. (2012). Numerical study of a butanol/heptane fuelled homogeneous charge compression ignition (hcci) engine utilizing negative valve overlap. *Applied Energy*, 94(0):166 – 173.
- Vressner, A., Lundin, A., Christensen, M., and Johansson, P. T. B. (2003). Pressure oscillations during rapid HCCI combustion. *SAE Paper No. 2003-01-3217*.
- Vulli, S., Dunne, J. F., Potenza, R., Richardson, D., and King, P. (2008). Time-frequency analysis of single-point engine-block vibration measurements for multiple excitation-event identification. *Journal of Sound and Vibration*, 321:1129–1143.
- Wong, R. and Mok, K. (2008). Design and modeling of a novel electromechanical fully variable valve system. *SAE Paper No. 2008-01-1733*.
- Yang, J., Culp, T., and Kenney, T. (2002). Development of a gasoline engine system using HCCI technology - the concept and the test results. *SAE Paper No. 2002-01-2832*.
- Yao, M., Zhang, B., Zheng, Z., Cheng, Z., and Xing, Y. (2005). Experimental study on the effects of EGR and octane number of PRF fuel on combustion and emission characteristics of HCCI engines. *SAE Paper No. 2005-01-0174*.
- Yunlong, B., Zhi, W., and Jianxin, W. (2010). Knocking suppression using stratified stoichiometric mixture in a DISI engine. *SAE Paper No. 2010-01-0597*.
- Zhang, Z. and Tomita, E. (2000). A new diagnostic method of knocking in a spark-ignition engine using the wavelet transform. *SAE Paper No. 2000-01-1801*.
- Zhang, Z. and Tomita, E. (2001). Diagnostic of knocking by wavelet transform method utilizing real signal as mother wavelet. *SAE Paper No. 2001-01-3546*.
- Zhao, J. and Seethaler, R. J. (2011). A fully flexible valve actuation system for internal combustion engines. *IEEE/ASME Transactions on Mechatronics*, 16:361–370.

APPENDIX A

UNCERTAINTY ANALYSIS

In order to understand the effects of uncertainty in the measured, calculated, and cyclical parameters an error analysis is performed on the experimental data.

A.1 Measured Parameters

Measured parameters such as intake temperature, exhaust pressure and oil temperature contain uncertainty from two sources; the calibration accuracy and the systematic variation. The uncertainty due to calibration is found using the 95% confidence bounds. The systematic uncertainty is determined by recording no less than 20 data points at steady state, where the 95% confidence interval can then be calculated [Handford, 2009]. The combination of these errors is determined using the room sum of the squares (RSS) method [Moffat, 1988]

$$\delta R = \sqrt{\sum_{i=1}^{Num} \delta X_i^2} \quad (\text{A.1})$$

where δR is the resulting uncertainty, Num is the number of components, and δX_i is the uncertainty of each component. Some measured parameters and their uncertainties are tabulated in Table A.1.

Table A.1: Uncertainty in Measured Parameters

Parameter	Value	Uncertainty (\pm)
Bore [m]	0.097	0.001
Stroke [m]	0.089	0.001
IVO [aTDC]	-360 – -300	2
IVC [aTDC]	-240 – -140	2
EVO [aTDC]	80 – 180	2
EVC [aTDC]	300 – 360	2
T_{int} [$^{\circ}C$]	23.7 – 104	5
P_{int} [kPa]	59.7 – 100.4	2
N [RPM]	679 – 1150	15
λ [-]	0.90-2.80	1%
Octane Number [PRF]	0-100	0.1
Injected Fuel Energy [kJ]	0.4042-1.032	0.005

A.2 Calculated Parameters

Calculated parameters such as IMEP, Power and Thermal efficiency contain uncertainty from multiple measured parameters. The uncertainty is combined determined by using equation A.2

$$\varepsilon_{a_i}^2 = \sqrt{\sum_{i=1}^n \left(\frac{\delta equation}{\delta a_i} \right)^2 (\varepsilon_{a_i}^2)} \quad (A.2)$$

where ε is the error in the a_i term.

A.3 Cyclical Parameters

Cyclical measurement error are those, such as the pressure trace, where the cyclic variability is a significant source of uncertainty on the mean value presented. The error is combined using the RSS method with both the calibration error as well as the variability in the measurement.

APPENDIX B

EXPERIMENTAL DATA SUMMARY

Data for the tests recorded in this thesis are tabulated in Tables B.1 to B.3. Data logging is initiated manually, either on a CAD based system such NI and CAS or time based such as dSPACE 1103 controllers, dSPACE microautobox, and ADAPT. The data from the 5 computers are then transferred to KOCH-GRAD09 for post-processing. The data is recorded based on Date and test number. Relevant information for the tests are given as well in the Tables below.

B.1 HCCI Data for Cam Phasers

Table B.1: HCCI Cam Phasing Test Data

Date	Test	Speed [RPM]	IVC [bTDC]	Control Strategy	Notes
Oct14 10	1	1033	160	Steady State	Low knock
Oct14 10	2	1033	160	Steady State	high knock
Oct14 10	3	1033	160	PI	Step Increase and step decrease
Oct14 10	5	1033	160	PI	Step Increase
Oct14 10	6	1033	160	PI and FF	Step Increase
Oct14 10	7	1033	160	PI	Step Increase
Oct14 10	8	1033	160	PI + FF	Step Increase
Oct14 10	9	1033	160	PI + FF	Step Increase and step decrease
Oct14 10	10	1033	160	PI + FF	Step Increase and step decrease
Oct14 10	11	1033	160	FF	Step Increase
Sept1 10	1	1031	160	PI	Step Increase
Sept1 10	3	1031	160	FF + FF	Step Increase
Sept1 10	4	1031	160	FF + FF	Step Increase
Sept1 10	5	1030	160	FF + FB	Step Increase
Sept1 10	7	1031	160	FF	Step Increase
Sept1 10	8	1030	160	PI	Decreasing Energy Step
Sept1 10	9	1030	160	PI and FF	Decreasing Energy Step
Jul27 10	1	1030	160	Steady State	High knock
Jul27 10	2	1030	160	Steady State	High knock
Jul27 10	3	1030	160	Steady State	Low knock
Jul27 10	4	1030	160	Steady State	Motoring Trace

B.2 SI Data for EVVA

Table B.2: EVVA Test Data for SI chapter

Date	Test	Speed [RPM]	ON [PRF]	Energy Injected [kJ]	IVO[aTDC]	IVC[aTDC]	EVO[aTDC]	EVC [aTDC]	Notes
Feb24 12	1	800	100	1.014	-300	-160	180	300	Steady State
Feb24 12	2	800	100	1.014	-300	-195	180	300	Steady State
Feb24 12	3	800	100	1.014	-300	-195/-160	180	300	Cyclic IVC
Jan24 12	1	750	100	1.0316	-300	-160	180	300	Steady State w/ Emissions
Jan24 12	2	750	100	1.0316	-300	-180	130	300	Steady State w/ Emissions
Jan24 12	3	750	100	1.0316	-300	-170	180	300	Steady State w/ Emissions
Jan24 12	4	750	100	1.0316	-340	-190	180	340	Steady State w/ Emissions
Dec2 11	1	777	100	0.933	-300	-180	180	300	Steady State w/ Emissions
Dec2 11	2	777	100	0.933	-300	-180	130	300	Steady State w/ Emissions
Dec2 11	3	777	100	0.917	-300	-180	180	300	Steady State w/ Emissions
Dec2 11	4	776	100	0.882	-300	-160	180	300	Steady State w/ Emissions
Dec2 11	5	775	100	0.943	-300	-200	180	300	Steady State w/ Emissions
Dec1 11	1	774	N/A	N/A	-300	-180	180	300	Motoring
Dec1 11	2	768	100	0.919	-300	-180	130	300	Steady State
Dec1 11	3	771	100	0.915	-300	-180	180	300	Steady State w/ Emissions
Dec1 11	4	769	100	0.915	-300	-160	130	300	Steady State w/ Emissions
Dec1 11	5	771	100	0.903	-300	-160	180	300	Steady State w/ Emissions
Dec1 11	6	771	100	0.968	-300	-200	180	300	Steady State w/ Emissions
Oct28 11	1	777	100	0.932	-300	-180	180	300	Steady State
Oct28 11	2	777	100	0.680	-300	-180/-100	180	300	Cyclic IVC
Oct28 11	3	774	N/A	N/A	-300	-180	180	300	Motoring
Sept20 11	1	777	N/A	N/A	-300	-180	180	300	Motoring
Sept20 11	2	777	100	0.692	-300	-180	180	300	Steady State
Sept20 11	3	774	100	0.692	-300	-180	180	300	Steady State

B.3 HCCI Data for EVVA

Table B.3: EVVA Test Data for HCCI chapter

Date	Test	Speed [RPM]	ON [PRF]	Energy Injected [kJ]	IVO[aTDC]	IVC[aTDC]	EVO[aTDC]	EVC [aTDC]	Notes
Feb24 12	1	800	11	0.440	-300	-180	180	300	Steady State
Feb24 12	2	800	11	0.440	-300	-230	180	300	Steady State
Feb24 12	3	800	11	0.440	-300	-230/-180	180	300	Cyclic IVC
Dec21 11	1	777	10.3	0.439	-300	-200	180	300	Steady State w/ Emissions
Dec21 11	2	775	10.3	0.439	-300	-180	130	300	Steady State w/ Emissions
Dec21 11	3	776	10.5	0.449	-300	-160	180	300	Steady State w/ Emissions
Dec21 11	4	776	3	0.404	-340	-180	180	340	Steady State w/ Emissions
Dec21 11	5	775	3	0.404	-300	-180	180	300	Steady State w/ Emissions
Dec8 11	3	727	0	0.317	-300	-180	180	300	Steady State
Dec8 11	4	728	0	0.428	-300	-180	180	300	Steady State
Dec8 11	5	729	10	0.435	-300	-180	180	320	Steady State
Dec8 11	6	728	10	0.435	-300	-150	180	300	Steady State
Dec8 11	7	729	10	0.435	-300	-180	180	300	Steady State w/ Emissions
Dec8 11	8	728	10	0.435	-300	-150	180	300	Steady State w/ Emissions
Dec8 11	9	775	12	0.445	-300	-180/-230	180	300	Cyclic IVC
Dec8 11	10	777	20	0.433	-300	-190/-220	180	300	Cyclic IVC

APPENDIX C

EXPERIMENTAL SETUP

C.1 Program and Analysis files Used

Table C.1: Programs used

File Name	Description
knockcontrol2.mdl EVVT2.mdl Phasermodelexperiment.mdl	Simulink files used for compiling to dSPACE MicroAutoBox
knockcontrol2.cdx EVVT2.cdx Phasermodelexperiment.cdx	ControlDesk files used with dSPACE MicroAutoBox
single_cylinder5.ini phaser_sep28.tst	ADAPT configuration and screen files
vibration4.vi valvecheckv2.vi	National Instruments files
Mercedes_phaser_MS.xml. CASconfiguration.xml	CAS configuration file
fr.mk	make file for compiling c code to ds1103
ValveControl3a.cdx	ControlDesk files for ds1103

C.2 Pressure Sensor Calibration

The new 6061B pressure transducer was calibrated using a deadweight tester and CAS software. The transducer was step tested at 200, 400, 600 and 800 PSI. The average sensitivity of the transducer was 26.63 pC/Bar with a standard deviation of

Table C.2: Analysis and plot generation files used

File Name	Description
THESIS_cas2mat_converter.m	Converts CAS “.P01” files to “.mat” files
pressureplot.m	Used for DWT and CWT plot generation
knockcontrolandNI.m	Used for DWT knock control analysis
psdhighandlowknock2.m	Compares the DWT and PSD method to P_{rms}
TexhSI.m maxROPR_SI.m IMEPeffecticiency_intake_xcorr.m.m IVCsweep_xcorrdata.m	Analysis files for section 5.1
load_dspacev1b.m	Analysis file for section 5.2
OneCycleForSim.m parammod.m simulationplotter.m	Preparation and analysis files for controller validation used in section 5.3 and 6.3
cyclicIVC_SIintake.m	Plot generation file for section 5.4
ThetaPmax.m	Analysis file for θ_{Pmax} and return maps
temperatureeffects.m warm_to_cold_compare_intake.m warm_to_cold_compare_exhuast.m	Analysis files for section 5.5
HCCIemissions.m TexhHCCI.m maxROPR_HCCI.m IMEPeffectcalculation.m	Analysis files for section 6.1
cyclicIVC_HCCIintake.m	Analysis file for section 6.2

0.04 pC/bar. Figure C.1 illustrates the sensitivities at each step conducted.

The actual step test for the four cases are plotted in C.2. It can be seen there is an equal offset in the cases. This is addressed with the signal pegging that compensates for the drift of the signal amplifier. The manufacturer calibration was 26.54 pC/bar at 50°C.

Validyne pressure transducers were used in other pressure measurements. The following sample calibrations were completed with an Omega Digital Pressure Indicator.

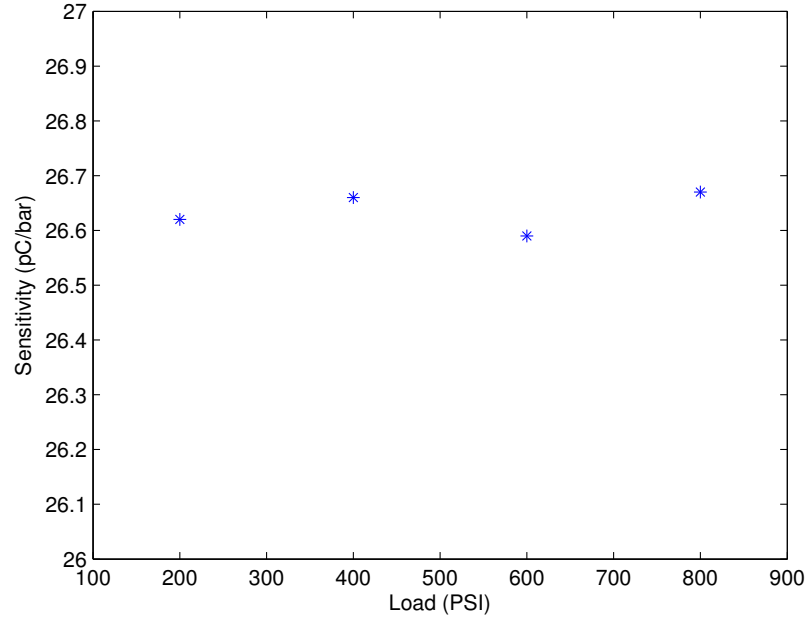


Figure C.1: Sensitivity of the pressure transducer

C.3 Dynamometer Load Cell Calibration

The dynamometer is connected to a load cell which measures a voltage from the strain gauge due to the torque applied. Calibration was performed once and the plot of the calibration can be seen in Figure C.11. The linear fit has an r^2 value of 0.9999 and a maximum full scale error of 0.1122

C.4 Emissions Testbench

The exhaust gases are measured with a five gas emissions analyzer Atkins [2004] 10cm from the exhaust port. The sample gas is directed through a heat exchanger where the water in the sample condensed into a water trap. The air is then filtered in a 0.1 micron particulate filter and the sample sent to the emissions bench. The emission analyzers and related specifications can be found in Table C.3.

The emissions bench is calibrated using a zero and span. Calibration is required

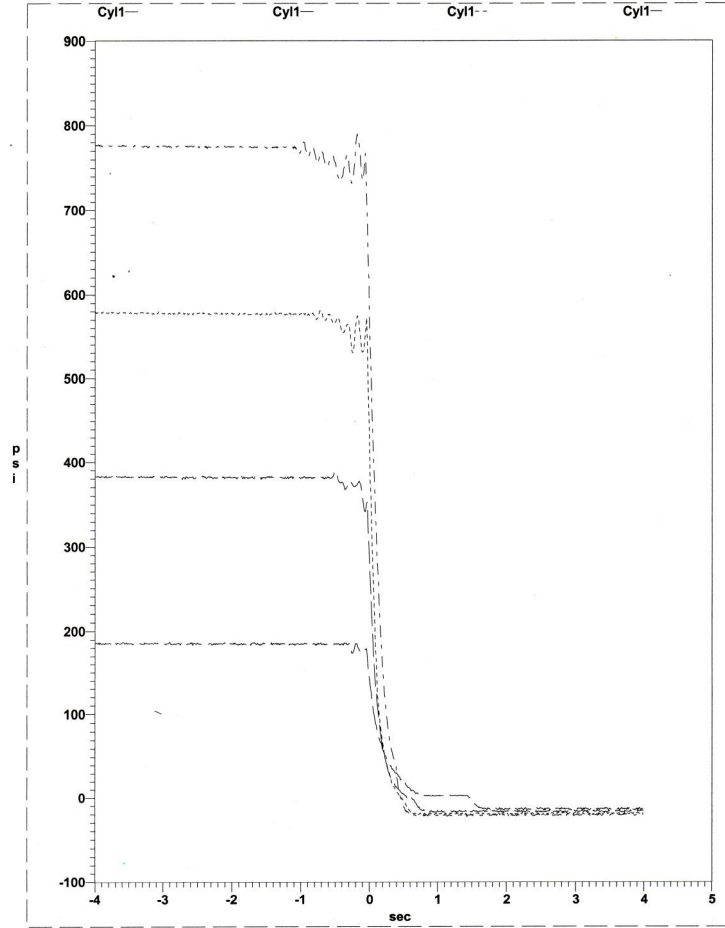


Figure C.2: Step tests using the dead weight calibrator

Table C.3: Emissions Bench

Manufacturer and Model	Gas Analyzer	Range	Resolution
Horiba FIA-510	uHC	0-10000 ppmC	10 ppm
Horiba CLA-510SS	NO_x	0-2500 ppmC	1 ppm
Siemens OXYMAT6	O_2	0-25%	0.01%
Siemens ULTAMAT6	CO	0-10%	0.01%
Siemens ULTAMAT6	CO_2	0-25%	0.01%

for both the test Bench as well as ADAPT which reading the analog inputs from the test bench. Calibration was completed on a weekly basis.

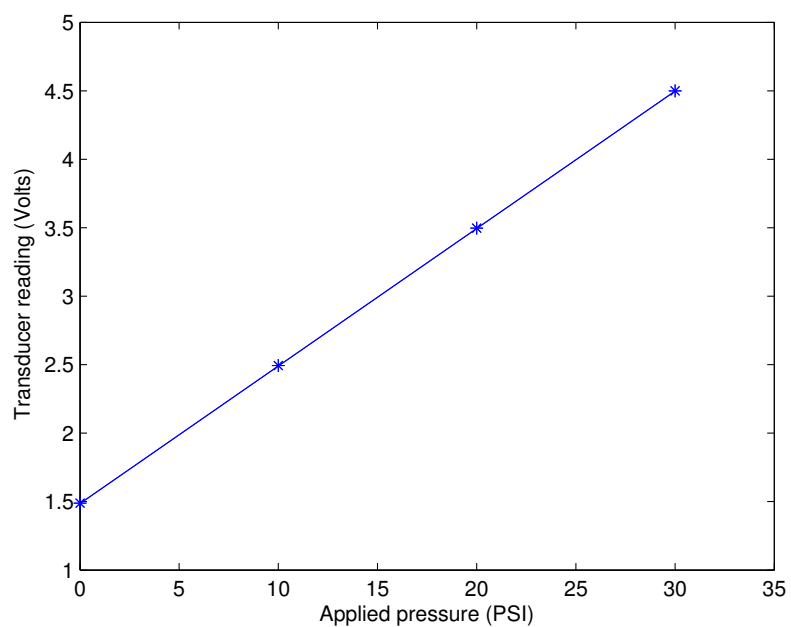


Figure C.3: Pressure transducer open to atmosphere. This calibration had a r^2 value of 1.0000 and a maximum full scale error of 0.0139%

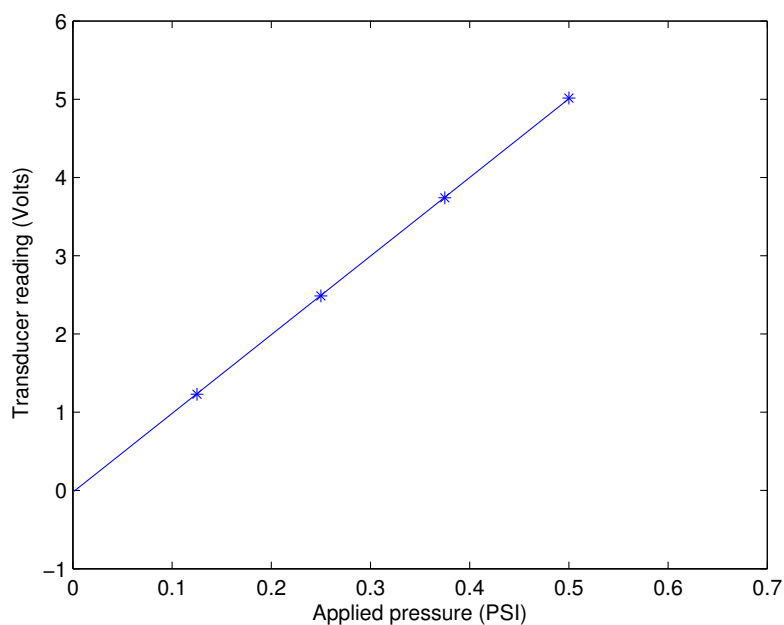


Figure C.4: Pressure transducer across the laminar air flow meter. This calibration had a r^2 value of 0.9999 and a maximum full scale error of 0.2127%

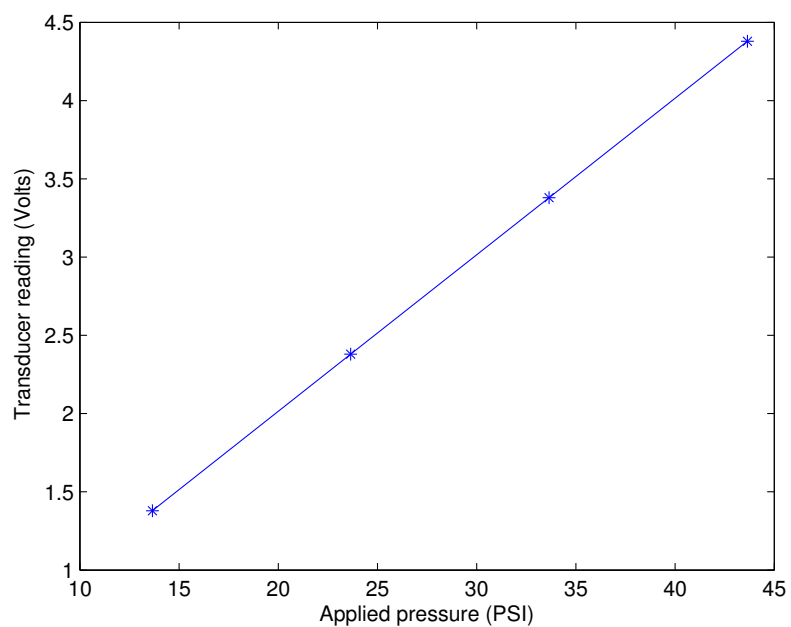


Figure C.5: Absolute pressure transducer for the intake runner. This calibration had a r^2 value of 1.0000 and a maximum full scale error of 0.0042%

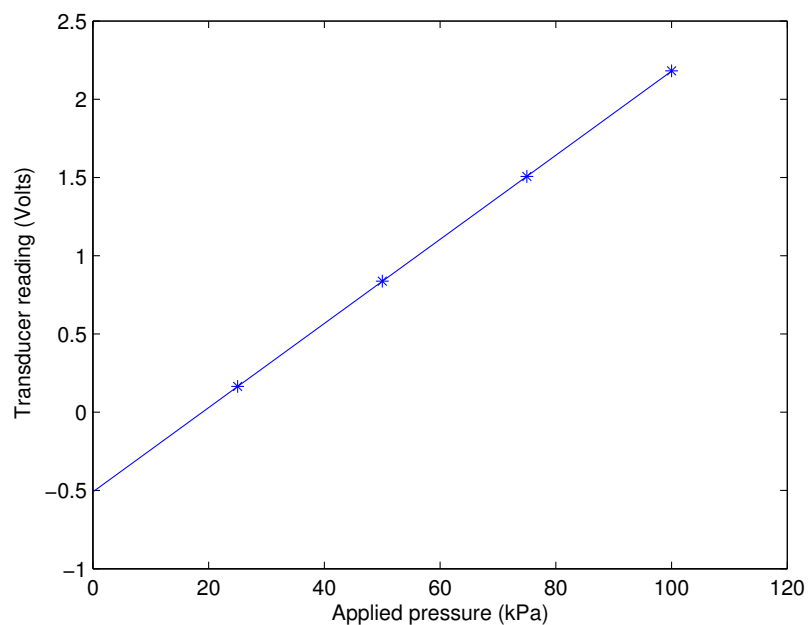


Figure C.6: Manifold Absolute Pressure (MAP) transducer. This calibration had a r^2 value of 0.9999 and a maximum full scale error of 0.0657%

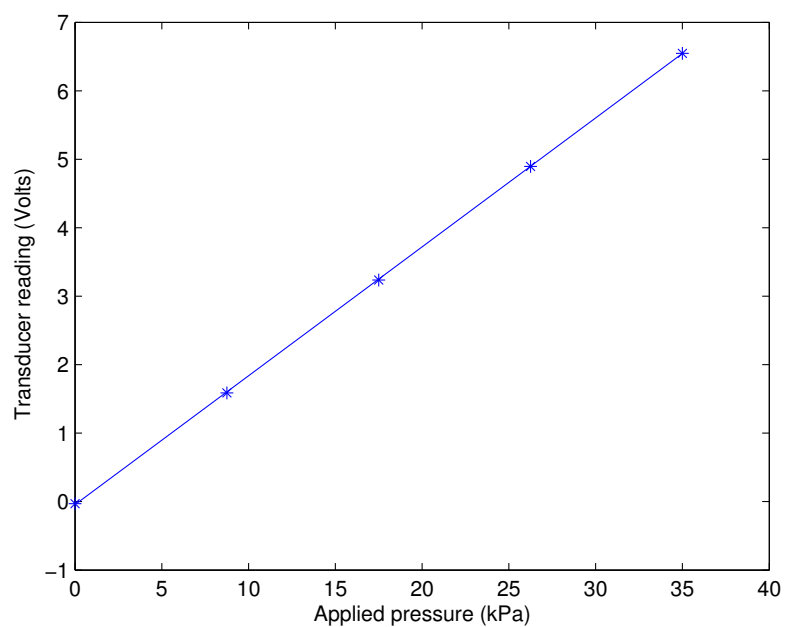


Figure C.7: Exhaust Pressure transducer. This calibration had a r^2 value of 0.9999 and a maximum full scale error of 0.2270%

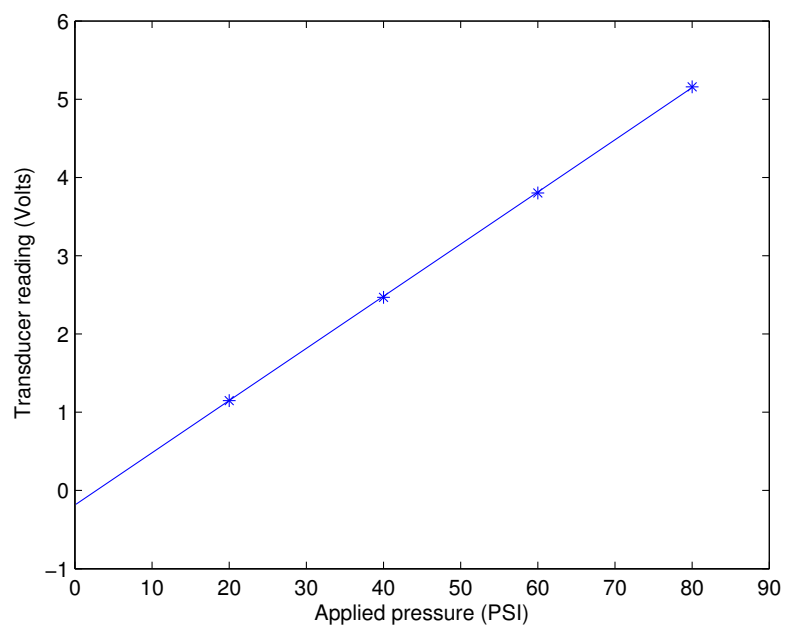


Figure C.8: N-heptane fuel pressure transducer. This calibration had a r^2 value of 0.9999 and a maximum full scale error of 0.2478%

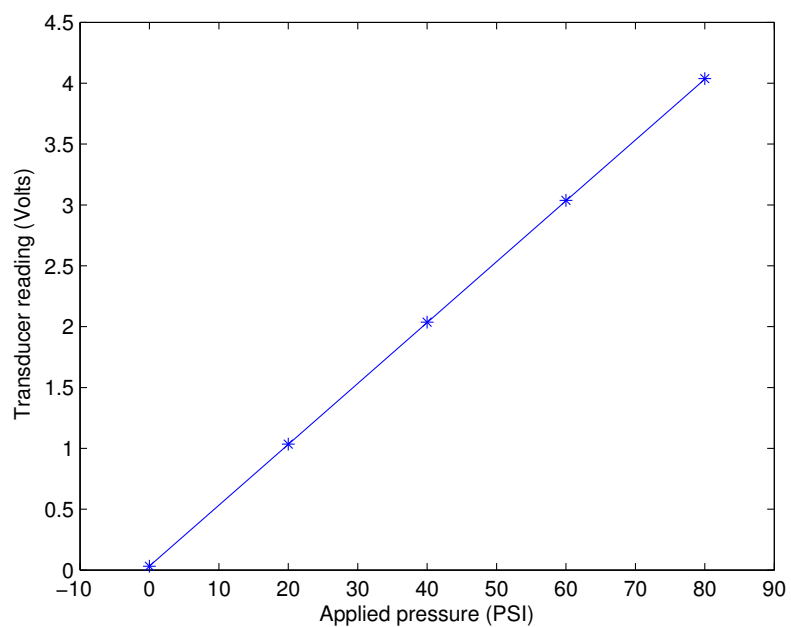


Figure C.9: Iso-octane fuel pressure transducer. This calibration had a r^2 value of 1.0000 and a maximum full scale error of 0.0392%

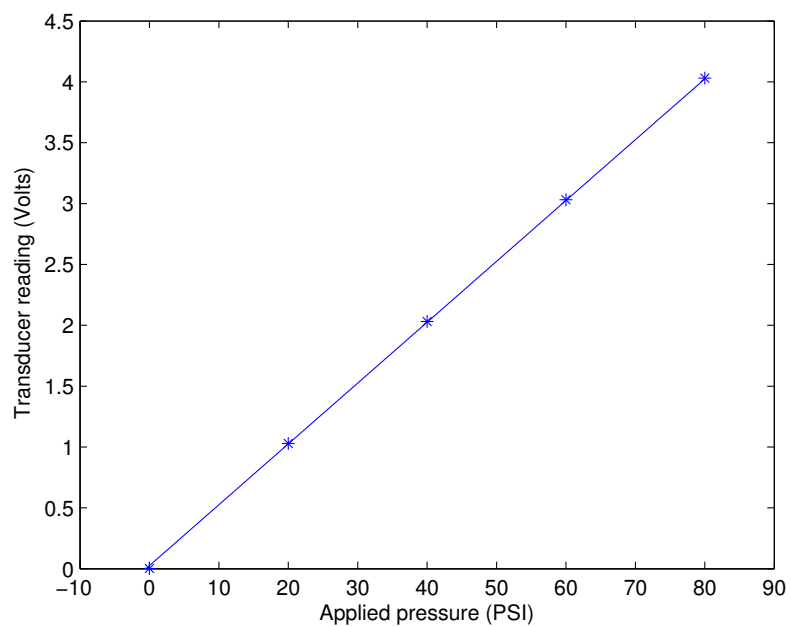


Figure C.10: Oil pressure transducer. This calibration had a r^2 value of 0.9999 and a maximum full scale error of 0.0713%

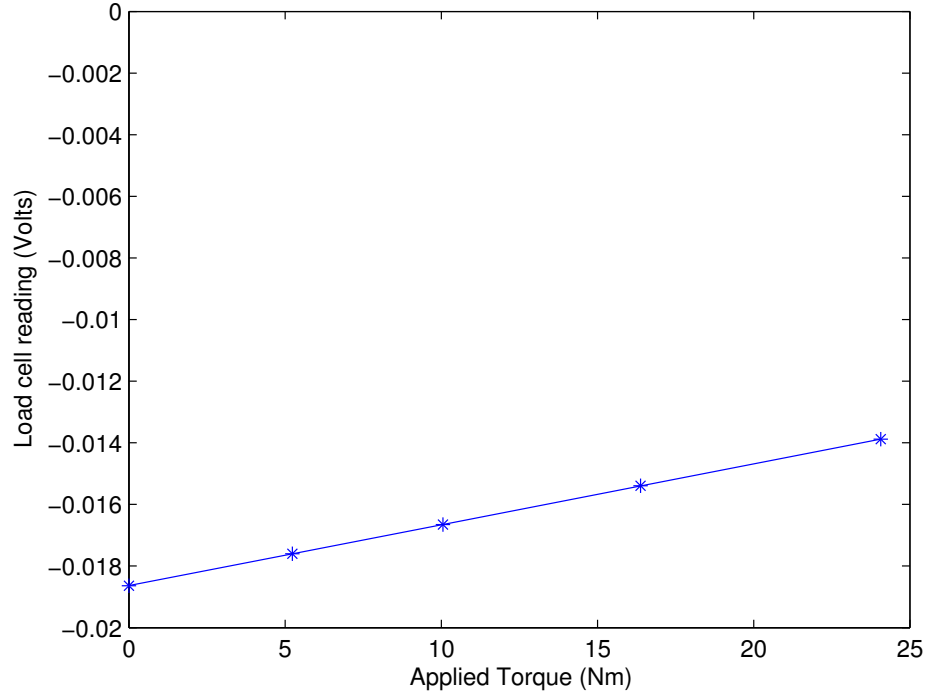


Figure C.11: Dynamometer load cell calibration

C.5 Cylinder Pressure Signal Pegging

The pressure transducer signal is pegged with Baseline CAS once every engine cycle. The pressure transducer signal is pegged to intake manifold pressure when the intake valve is open. With the cam phasing system the MAP value was averaged for 10 degrees at -180 degrees aTDC and applied at -180 degrees aTDC one full cycle after. With the EVVA system the pegging was done at -240 degrees aTDC for 40 degrees and applied at -240 degrees aTDC one full cycle later.